

ABSTRACT

HE, NANFEI. Graphene-Based Functional Fibers and Their Applications in Energy-Storage Textiles. (Under the direction of Dr. Wei Gao).

This thesis summarizes our exploration of various strategies to fabricate graphene-based fibers with different components and distinct structures from wet-spinning processes, followed by the demonstration of these fibers as effective electrodes in one-dimensional (1D) fiber/yarn shaped supercapacitors. 1D flexible fiber supercapacitors (FSCs) have recently attracted great interests as promising energy-storage units that can be seamlessly incorporated into textiles *via* weaving, knitting or braiding. The major challenge existing in this field is to develop tougher and more efficient FSCs with a relatively easy and scalable fabrication process. Graphene, due to its attractive intrinsic merits, including large surface area, good mechanical strength, and high electrical conductivity, has been extensively studied as electrode materials for electrochemical double-layer capacitors (EDLCs). Thanks to the liquid crystalline behavior of graphene oxide (GO) dispersions, graphene fibers can be fabricated *via* solution processing of GO followed by chemical reduction or thermal treatment to reduced graphene oxide (rGO) fibers. Among all the fiber-extrusion processes, wet-spinning technique is the most feasible and scalable pathway to make continuous GO fibers, during which fiber structures and subsequent properties can be easily tuned. Wet-spun GO/rGO fibers have been widely investigated in literature, but challenges still exist to combine large surface area, high electrical conductivity, and sufficient mechanical strength/toughness within an individual fiber. Trade-offs have to be made between the highly desired microscale surfaces for energy storage and the satisfactory mechanical and electrical properties for real-world applications. To address the above-mentioned dilemma, we first studied the effect of solvent and coagulation bath on the morphology, structure, mechanical and electrical properties of the resulted rGO fibers. Large surface area and high toughness were realized in rGO

fibers fabricated from the combination of NMP/ethyl acetate as the dope-solvent/coagulant pair, which is superior to the H₂O/glacial acetic acid pair for solid-state FSC applications. Later on, in order to improve the mechanical strength and electrical conductivity of fibers, we introduced ionic cross-linkers into the coagulant by utilizing the solvent-exchange process happening during coagulation. Various cations with different charge densities were investigated, including trivalent Al³⁺, Fe³⁺ and divalent Ca²⁺. A strong correlation between the charge density of the cations and the resulted fiber morphology has been observed, with the higher cation charge density leading to more wrinkled surfaces, higher toughness, and thus improved specific capacitance. In addition to EDLC, we introduced pseudocapacitive materials, MXene (Ti₃C₂T_x), into rGO fibers to further improve the capacitance and energy density of the final devices. By optimizing the weight ratio between GO and MXene, heterostructured rGO&MXene fibers with balanced mechanical and electrical properties were obtained. Furthermore, electrolyte mediated rGO&MXene (EM-rGO&MXene) fibers with H₂SO₄ incorporated, demonstrated good wettability and excellent capacitance, exceeding most of state-of-the-art fiber electrodes. EM-rGO&MXene fibers can be further twisted into yarn electrodes, followed by electrolyte incorporation to yarn-shaped supercapacitors (YSCs). Our YSCs show good capacitive performance and good bending stability, with tunable mechanical/electrochemical features to satisfy various requirements in both textile processing and energy-storage applications.

© Copyright 2019 by Nanfei He

All Rights Reserved

Graphene-Based Functional Fibers and Their Applications in Energy-Storage Textiles

by
Nanfei He

A dissertation submitted to the Graduate Faculty of
North Carolina State University
in partial fulfillment of the
requirements for the degree of
Doctor of Philosophy

Fiber and Polymer Science

Raleigh, North Carolina
2019

APPROVED BY:

Wei Gao
Committee Chair

Xiangwu Zhang

Samuel Hudson

Peter Fedkiw

DEDICATION

*To my parents and all of my friends,
without whom none of my success would be possible.*

BIOGRAPHY

Nanfei He is from Jiande, Hangzhou, Zhejiang Province in East China. She obtained bachelor's degree in Textile Engineering from Donghua University, Shanghai, China in 2011. Then, she continued to pursue her master's degree in Nonwoven Materials Science and Engineering also in the College of Textiles, Donghua University. After graduation, she joined the PhD program in Fiber and Polymer Science at North Carolina State University in 2015 Fall. She worked on the fabrication of graphene fibers and investigation of their application in wearable energy storage textiles, under the direction of Dr. Wei Gao.

ACKNOWLEDGMENTS

First of all, I would like to express my sincere gratitude and deepest appreciation to my PhD advisor, Dr. Wei Gao, for the supervising and supporting in my PhD program. Her visionary guidance, insightful advices and infinite patience lead to the successful completion of this dissertation.

I would also like to thank my committee members, Dr. Samuel Hudson, Dr. Xiangwu Zhang and Dr. Peter Fedkiw, for their contributions of time and expertise, which greatly improved the qualities of my research work and final thesis.

I also appreciate the supportive and helpful advices that I have received from my current and former group members Dr. Qin Pan, Dr. Shradha Patil, Dr. Jiangang Qu, Yanan Wang, Debjyoti Banerjee and research collaborators at NCSU Prof. Abdel-Fattah Seyam, Prof. Philip Bradford, Dr. Ozkan Yildiz, Prof. Sunkyu Park, Dr. Seunghyun Yoo, and collaborators from University of Pittsburg Prof. Guofeng Wang and Weitao Shan.

In addition, I am grateful for the resources and instrument training from Judy Elson, Birgit Andersen, Teresa White in the Wilson College of Textiles, as well as Chuck Mooney, Ching-Chang Chung, Chuanzhen Zhou from Analytical Instrumentation Facility (AIF).

Finally, I would like to express my immense gratitude towards my parents for their consistent supporting, encouragement, and enduring love throughout my education, and all those close friends that have been my support during my time at NCSU, Chunhong Lu, Siqu Zhang, just to name a few. Thank you for all their generous help and support whenever and wherever I needed.

TABLE OF CONTENTS

LIST OF TABLES	viii
LIST OF FIGURES	ix
LIST OF ABBREVIATIONS	xvi
Chapter 1: Graphene Based Functional Fibers and Their Applications in Energy-Storage	
Textiles	1
1.1. Fabrication of Graphene Based Fibers.....	2
1.1.1. Properties of GO Dispersions	3
1.1.2. Wet-Spinning Method	9
1.1.3. Other Methods	11
1.2. Properties of Graphene Based Fibers.....	14
1.2.1. Mechanical Properties	14
1.2.2. Electrical Properties.....	18
1.2.3. Thermal Properties	21
1.2.4. Surface Area	21
1.3. Application in Electronic Textiles	23
1.3.1. Wearable Energy-Storage Devices	23
1.3.2. Actuators.....	27
1.3.3. Lightweight Conductors	30
1.3.4. Other Applications.....	30

1.4. Concluding Remarks.....	32
Chapter 2: Graphene-Fiber-Based Supercapacitors Favor N-Methyl-2-Pyrrolidone/Ethyl Acetate as the Spinning Solvent/Coagulant Combination	34
2.1. Introduction.....	34
2.2. Experimental Section.....	37
2.2.1. Synthesis of GO.....	37
2.2.2. Fiber Spinning	38
2.2.3. Structural Characterizations	38
2.2.4. Electrochemical Performance Characterizations.....	39
2.3. Results and Discussion	40
2.4. Conclusion	61
Chapter 3: Mordant Inspired Wet-Spinning of Graphene Fibers for High Performance Flexible Supercapacitors	62
3.1. Introduction.....	62
3.2. Experimental Section.....	65
3.2.1. Materials	65
3.2.2. Synthesis of GO.....	65
3.2.3. Fabrication of rGO Fibers.....	66
3.2.4. Structure Characterizations.....	66
3.2.5. Electrochemical Performance Characterizations.....	67

3.2.6. Density Functional Theory Calculations	68
3.3. Results and Discussion	69
3.4. Conclusion	89
Chapter 4: Graphene/MXene Supercapacitor Yarns as Weaveable Energy-Storage	
Units	90
4.1. Introduction.....	90
4.2. Experimental Section.....	93
4.2.1. Synthesis of GO and MXene ($Ti_3C_2T_x$).....	93
4.2.2. Fabrication of Fibers.....	93
4.2.3. Fabrication of YSCs	95
4.2.4. Structural Characterizations	95
4.2.5. Electrochemical Performance Characterizations.....	96
4.3. Results and Discussion	97
4.3.1. Fabrication of Graphene & MXene Heterostructured Fibers	97
4.3.2. Electrolyte Mediated Fiber Electrodes for High Capacitive Performance	104
4.3.3. Assemble YSCs Towards Real Energy Storage Application	109
4.4. Conclusion	120
REFERENCES	121

LIST OF TABLES

Table 1.1	Mechanical and electrical conductivity of GO/rGO fibers reported in the literature	13
Table 2.1	Mechanical and electrical properties of rGO@NMP-Fs as a function of draw ratio applied in the wet-spinning processes	53
Table 2.2	Z-view fitting results for Nyquist plots in Figure 2.9c and d with the equivalent circuit shown in Figure 2.12.....	56
Table 2.3	Comparison of specific capacitance (based on a single electrode) and energy density (based on device) of solid-state FSC	60
Table 3.1	Physicochemical Properties of the Cations	75
Table 3.2	SSA, mechanical, electrical and alignment properties of rGO Fibers. Fiber alignment was calculated from the ratio of G peak intensities (parallel I_{\parallel} vs. perpendicular I_{\perp}) of rGO fibers. The ratio is the average of five measurements made over different positions of each fiber	79
Table 3.3	Z-view fitting results for Nyquist plots in Figure 3.8 d with the equivalent circuit shown in Figure 3.9	83
Table 3.4	Comparison of specific capacitance (based on a single electrode) and energy density (based on device) of solid-state FSC	87
Table 4.1	Comparison of the fabrication method, specific capacitance, energy density and power density of various YSCs.....	119

LIST OF FIGURES

- Figure 1.1 (a-b) Typical POM images of nematic (a) and lamellar mesophases of GO LC dispersion (adapted from ref. 16);^{1 1} (c) Schematic illustration of the calculation of aspect ratio (adapted from ref. 3); (d) Chiral mesophase of GO LC dispersion;^{2 2} (e) Proposed model for one pitch of GO chiral LCs (d and e adapted from ref. 11) 4
- Figure 1.2 (a) left: aqueous GO LC dispersion (0.5 wt %); right: 0.01 wt % GO aggregate upon adding 50 mM NaCl (adapted from ref. 20); (b-c) POM images of GO (b) and GO+KOH (c) dispersion, respectively (adapted from ref. 24); (d-g) representative POM images of LC GO in various organic solvents at a concentration of 2.5 mg mL⁻¹ (adapted from ref. 25)..... 6
- Figure 1.3 (a) Upon applying shear stress, nematic domains in large-sized GO LC dispersion are sheared and oriented along the direction of shear stress, resulting in continuous fibers via wet spinning; (b) in the case of small-sized GO with same concentration, no orientation is induced as applied shear force and found to be non-spinnable (adapted from ref. 19)..... 8
- Figure 1.4 The schematic of wet-spinning processes from GO LC spinning dope, drawing by (a) a rotating coagulation bath and (b) a collection unit (adapted from ref. 32); (c) confined hydrothermal approach to rGO fibers, where GO was reacted with vitamin C in a PP pipeline for 1 h at 80°C, and then drying in air (adapted from ref. 12); (d) a GO film was cut into long strips and twisted into GO fiber (adapted from ref. 13)..... 10
- Figure 1.5 (a) Structural model of multiscale defects in rGO fibers, spanning from defective rGO sheets derived from GO after mild reduction; nanoscale boundaries and voids; inhomogeneous core-sheath structure and randomly orientation at microscale and macroscale; (b) structure model of rGO fibers with defects control at all levels (adapted from ref. 59)..... 15
- Figure 1.6 (a) Schematics of the “intercalated” structure of the GO and rGO fibers: large-sized GO sheets form the well aligned backbone, whereas small-sized GO sheets fill the space and voids between LGO sheets (adapted from ref. 33);^{3 3} (b) electrical conductivity of pure rGO fibers and K, Br₂ and FeCl₃ doped rGO fibers. The insert is the photo of K-doped rGO fibers (adapted from ref. 60); (c) the electrical conductivity changes of various metal coated rGO fibers under 100 cycles bending. The insert is the copper-coated rGO fibers (adapted from ref. 61)..... 20
- Figure 1.7 (a) using an acetone coagulation bath results in the high rate of water extraction from the GO gel, leading to higher rate of solidification and porous fiber structure (adapted from ref. 40);^{4 4} (b) Inject GO dispersion into liquid nitrogen then followed by freeze-drying, resulting in porous

	fiber structure (adapted from ref. 48); (c) the basified GO dispersion with better flowability results in wet-spun fiber with fine bark-like surface morphology (adapted from ref. 55).....	22
Figure 1.8	(a) Cross-sectional SEM image of core-sheath rGO fiber showing the core rGO fiber surrounding with amorphous rGO sheets; (b) schematic of two twisted rGO fibers assembled FSC (a and b adapted from ref. 75); (c) schematic illustration of the fabrication process of N-doped rGO and CNT composite fiber and its cross-sectional SEM image (adapted from ref. 43); (d) three typical configurations of FSC: from left to right, parallel, twisted and coaxial (adapted from ref. 74); ^{5 5} (e) schematic illustration of a coaxial FSC with a core rGO fiber and coated rGO sheath as electrodes; ^{6 6} (f) the specific capacitance of FSCs with various structure at different current density, demonstrating the coaxial FSC has the highest capacitance (e and f adapted from ref. 77); ^{6 6} (g) schematic of wet-spinning process for the MXene incorporated rGO fiber; (h) cyclic voltammetry (CV) curves, demonstrating good capacitive performance of MXene and rGO composite FSC (g and h adapted from ref. 81).	25
Figure 1.9	(a) Schematic illustration of the structure for the hybrid fiber of rGO/titania, which could be used as electrodes for fiber shaped batteries; (b & c) the rGO/titania fibers assembled battery can light up 6 LED lamps under bending (a-c adapted from ref. 82); (d) schematic of fiber shaped DSSC with rGO/Pt fiber as the counter electrode and a Ti wire with TiO ₂ nanotubes as working electrode; (e) working mechanism of the rGO fiber based DSSC; (f) J-V characteristics of the DSSC with different Pt content as the counter electrode (d-f adapted from ref. 83)	27
Figure 1.10	(a) Schematic showing the positioned laser reducing of GO fiber; (b) photos of a GO/rGO fiber under different RH condition (a and b adapted from ref. 84); (c) schematic showing the twisting process of GO fiber with spiral structure; (d) SEM images of directly GO fiber and twisted spiral GO fiber; (e) schematic illustrating showing that a spiral GO fiber can be driven to rotate by varying RH; application of the spiral GO fiber as a humidity switch (f) and electric generator (g) (c-g adapted from ref. 85).....	29
Figure 1.11	(a) Schematic illustration of fabrication process of rGO staple fiber based non-woven fabric. The inserted is the SEM image of the porous fabric (adapted from ref. 86); (b-d) SEM images of GO fibers via scrolling dry GO film; (e) I-E curve for the thermally reduced film scrolled GO fiber (b-e adapted from ref. 13).....	32
Figure 2.1	Fiber four-point probe setup for electrical conductivity measurement	39
Figure 2.2	(a) A schematic of our benchtop wet-spinning setup for GO-fiber fabrication; (b) a POM image of 20 mg ml ⁻¹ dispersions of GO@NMP;	

	(c) a POM image of 20 mg ml ⁻¹ dispersions of GO@H ₂ O; (d) rheological characterization of the two GO dispersions: dependence of the dispersion viscosity on shear rate.....	41
Figure 2.3	Size distribution of Graphene Oxide (GO) sheets. (a) an SEM image of GO sheets drop-casted onto a silica wafer; (b) the corresponding size distribution of the GO sheets. The average size of GO sheets is calculated to be <i>ca.</i> 16 μm	42
Figure 2.4	An FTIR spectrum of GO powders used in our experiments. Spectrum was measured in Attenuated Total Reflectance (ATR) mode using Ge crystal-plate under nitrogen (N ₂) purging	43
Figure 2.5	Digital pictures of GO dispersions in H ₂ O, NMP and DMF after being mechanically stirred for 48 h. Left: immediately after stirring stopped; Middle: one day after stirring stopped; Right: seven days after stirring stopped. GO formed stable dispersions in both H ₂ O and NMP for seven days, but many GO flakes precipitated in DMF after one day	44
Figure 2.6	SEM images of rGO@NMP-F (a, b, c) and rGO@H ₂ O-F (d, e, f).....	46
Figure 2.7	SEM images of fiber cross-sections of (a) GO@H ₂ O-F; (b) GO@NMP-F; (c) rGO@H ₂ O-F; (d) rGO@NMP-F.....	46
Figure 2.8	A proposed mechanism for the formation of rGO@H ₂ O-F and rGO@NMP-F. Comparing to water, NMP molecules carry fewer hydrogen bonding sites and cannot form hydrogen bonding with themselves. In the coagulation process, ethyl acetate diffuses into GO sheets, the larger size of ethyl acetate and weaker hydrogen bonding between GO and ethyl acetate lead to larger distance between GO sheets. After the evaporation of ethyl acetate, the larger inter-sheet distance would shrink more, and result in rougher and more wrinkled morphology in both longitudinal and transverse directions. In addition, rGO@H ₂ O-Fs present irregular multi-armed structure with less wrinkles, while the contour of rGO@NMP-Fs is more regular but with much more microscale wrinkles on sheet surfaces	48
Figure 2.9	(a) Typical strength-strain curves of rGO-F. The inset shows a highly flexible rGO-F. (b) conductivity and toughness of rGO-F. (c) CV curves at scan rate 40 mV s ⁻¹ . Inset is a photo of a FSC assembled from two parallel single fibers (scale bar, 2mm). (d) Nyquist plots from the EIS tests of rGO@NMP-FSC and rGO@H ₂ O-FSC.....	50
Figure 2.10	Polarized Raman spectra of an rGO@NMP-F with the incident laser beam parallel and perpendicular to the fiber axis, respectively. The Raman ratio, which is determined from the ratio between the G peak intensities of the two spectra (parallel <i>vs.</i> perpendicular), provides a useful probe for the	

relative degree of alignment	52
Figure 2.11 SEM images of rGO@NMP-Fs with draw ratio of (a) 1.5, (b) 1.75 and (c) 2, respectively	52
Figure 2.12 Cyclic voltammetry (CV) curves of rGO@NMP-FSCs with rGO@NMP-Fs at different draw ratios (1.5, 1.75 and 2). Among these, rGO@NMP-F at draw ratio of 1.5 exhibited the highest specific capacitance	54
Figure 2.13 Equivalent circuit for fitting Nyquist plots in the high frequency region by Z-view	55
Figure 2.14 Electrochemical performance of rGO@NMP-FSC. (a) CV curves at different voltage scan rates. The current is normalized by the scan rates. (b) CA and CV at different scan rates; (c) GCD curves at different current density; (d) Capacitance retention as a function of bending cycles. The inset is capacitance stability during bending from 0° to 180°. The inset photo in (e) shows the 180° bending state. (e) cycling stability for 5000 cycles. (f) Ragone plot of different FSCs and some commercial devices. Commercially available 4 V/500 μ Ah Li thin-film battery, ¹³⁹ 2.75 V/44mF commercial AC-EC, ¹⁰⁹⁷⁷ 3.5 V/25 mF SC136 and some published experimental data (A) a non-LC spinning pure rGO FSC, ¹¹⁴ (B) a CNT/rGO@CMC hybrid FSC ¹³² and (C) a MnO ₂ incorporated carbon fiber SC. ¹⁴⁰	58
Figure 3.1 Atomistic structure of (a) single-layer graphene and (b) optimized structure of single layer graphene oxide (GO). In the figure, carbon, oxygen and hydrogen atoms are plotted as the black, red and white balls, respectively.....	69
Figure 3.2 Top view (top) and lateral view (bottom) of metal cations adsorption configuration on a graphene layer through cation- π interaction and optimized by DFT method	69
Figure 3.3 Schematic illustration of the formation of rGO fibers from divalent and trivalent cations in coagulation baths, respectively. After solvent evaporation and chemical reduction, rGO fibers with different cation cross-linking resulted in dramatically different morphologies.....	71
Figure 3.4 Size distribution of Graphene Oxide (GO) sheets. (a) an SEM image of GO sheets drop-casted onto a silica wafer; (b) the corresponding size distribution of the GO sheets. The average size of GO sheets is calculated to be <i>ca.</i> 16 μ m	72
Figure 3.5 Morphologies of rGO fibers. SEM images of (a) acetic-acid coagulated rGO fiber; (b) Ca ²⁺ coagulated rGO fiber; (c) Al ³⁺ coagulated rGO fiber;	

	(d) Fe ³⁺ coagulated rGO fiber.....	74
Figure 3.6	Atomic structures of hydrated cations adsorption on a single layer GO surface (a) and intercalated atoms between two GO layers (b). In the figure, the black, red, white, and blue balls represent carbon, oxygen, hydrogen, and cations (Al ³⁺ , Fe ³⁺ , or Ca ²⁺), respectively.....	74
Figure 3.7	TOF SIMS secondary ion images of (a) Ca ²⁺ , (b) Al ³⁺ and (c) Fe ³⁺ acquired from corresponding rGO fibers along fiber axis direction, confirming the existing of cations in rGO fibers. TOF-SIMS measurements were conducted with an ION-TOF TOF-SIMS V instrument with bismuth beam for analysis and cesium beam for sputtering	77
Figure 3.8	(a) Schematic illustration of the wrinkling direction of rGO sheets in each rGO fibers. (b) Cross-sectional SEM images of rGO fibers. rGOF-Al ³⁺ has the most wrinkled structure through fiber cross-section (perpendicular to fiber axis), but still maintain good alignment along fiber axis.....	77
Figure 3.9	Typical polarized Raman spectroscopy of rGOF-Al ³⁺ fiber with the incident laser beam parallel and perpendicular to the fiber axis, respectively. The Raman ratio, which is determined from the ratio between the G peak intensities of the two spectra (parallel I_{\parallel} vs. perpendicular I_{\perp}), provides a useful probe for the relative degree of alignment	78
Figure 3.10	XRD patterns of rGO fibers. Fixed Time mode, step size 0.05 degree, dwell time 4 second. Wavelength to compute d-spacing 1.54059 Å, Cu/K-alpha 1	79
Figure 3.11	Comparison on the mechanical, electrical and electrochemical properties of rGO fibers coagulated from trivalent cation baths (Al ³⁺ and Fe ³⁺), divalent cation baths (Ca ²⁺), and non-crosslinker acetic acid. (a) Representative stress-strain curves of rGO fibers prepared using various coagulation baths. (b) Typical I-V curves of rGO fibers with the length of 2 cm. The inset shows a schematic of our four-probe apparatus for the electrical conductivity measurements. (c) CV curves at 40 mV s ⁻¹ . (d) Nyquist plot from the EIS test.....	81
Figure 3.12	Equivalent circuit for fitting Nyquist plots in the high frequency region by Z-view	83
Figure 3.13	Electrochemical characterization of rGOF-Al ³⁺ FSC in PVA/H ₂ SO ₄ electrolyte. (a) CV curves at different scan rates and (b) Galvanostatic charge/discharge curves at different current density. (c) Capacitance retention as a function of bending cycles, the inset is capacitance stability upon bending from 0° to 180°. (d) Ragone plot of rGOF-Al ³⁺ FSC compared with some commercial devices and other reported FSCs,	

including commercially available 4 V/500 μ Ah Li thin-film battery, ¹⁹¹ 3.5 V/25 mF SC, ¹⁹² 2.75 V/44mF commercial AC-EC ⁷ and (A) hierarchically porous sheath-core graphene based FSC, ⁸ (B) rGO/cellulose hybrid FSC, ¹⁹³ (C) non-LC spinning pure rGO FSC, ¹⁷¹ (D) rGO@NMP-FSC. ⁹	85
Figure 3.14 The calculated specific capacitance of rGOF-Al ³⁺ FSC at different current density	86
Figure 4.1 Fabrication of rGO & MXene based fibers and corresponding YSCs. (a) Schematic illustration of wet-spun GO & MXene fibers. (b) Fabrication of electrolyte mediated rGO&MXene fibers. (c) Fabrication of rGO&MXene fibers-based yarn electrodes and supercapacitors.....	95
Figure 4.2 SEM images of graphene oxide sheets (a) and MXene sheets (b)	98
Figure 4.3 XRD pattern of MAX (Ti ₃ AlC ₂) and MXene (Ti ₃ C ₂ T _x) powder	98
Figure 4.4 Characterization of fibers. (a) The relation between the mass ratio of incorporated MXene with the electrical conductivity, tensile strength and toughness of fibers. (b) SEM images of the surface of rGO fibers (0 wt% MXene), rGO&MXene fibers (60 wt% MXene) and EM-rGO&MXene fibers (60 wt% MXene) (from left to right). (c-e) Raman spectra (c), XRD spectra (besides fibers, the spectra of MXene was collected in particles) (d), and typical stress-strain curves (e) of rGO fibers, rGO&MXene fibers and EM-rGO&MXene fibers.....	99
Figure 4.5 SEM images of fiber cross-sections of (a,d) GO fiber; (b, e) rGO&MXene fiber; (c, f) EM-rGO&MXene fiber	101
Figure 4.6 Electrochemical performance of FSCs. (a, b) CV curves at 20 mV s ⁻¹ (a) and Nyquist plots (b) of rGO FSCs, rGO&MXene FSCs and EM-rGO&MXene FSCs. (c) Linear, areal and gravimetric capacitance of rGO fibers, rGO&MXene fibers and EM-rGO&MXene fibers. (d) A plot of CA versus $v^{-1/2}$, indicating the separation of diffusion-controlled capacitance from capacitive-controlled capacitance. (e) Capacitance retention of the EM-rGO&MXene FSCs performed by galvanostatic cycling at 5 mA cm ⁻² . The inset depicts galvanostatic cycling profiles collected at different current density. (f) Comparison of the areal and gravimetric capacitance of EM-rGO&MXene fiber electrode with other reported fiber electrodes, including hollow rGO fibers, ²³⁶⁻²³⁷ non-LC wet-spun rGO fiber, ¹¹⁴ rGO&MnO ₂ fiber, ²¹⁵ fibrous CNT aerogel, ²³⁸¹⁰¹⁰ rGO&MXene (88%) fibers, ²²⁰ and rGO&MXene (90%) fibers. ²²¹	104
Figure 4.7 Schematic illustration of EM-rGO&MXene fibers preparation procedure.	105
Figure 4.8 SEM images of cross-sectional PVA coated yarn electrode. (a) Cross-sectional	

	SEM image of rGO&MXene fiber-based yarn electrode; (b) Cross-sectional SEM image of EM-rGO&MXene fiber-based yarn electrode. (c) Surface SEM image of PVA based electrolyte coated yarn electrode.....	107
Figure 4.9	Fabrication and electrochemical performance of EM-rGO&MXene YSCs. (a) Schematic illustration of YSC fabrication process. (b) Typical stress-strain curves of yarn electrodes (with various degree of twists) and YSCs. (c) Areal and linear capacitance of EM-rGO&MXene YSCs at different scan rates. (d) Correlation between the linear capacitance of YSCs and the number of EM-rGO&MXene fibers incorporated.....	110
Figure 4.10	(a) CV curves of YSC at different scan rates from 5 mV s ⁻¹ to 100 mV s ⁻¹ . (b) GAL charge-discharge curve of YSC at different current.....	113
Figure 4.11	(a) Schematic illustration of the warp distribution per-segments on the loom. (b) Schematic illustration of the loop formation in knitting process.	114
Figure 4.12	(a) Typical load-strain curve of YSCs. (b) Cycling stress-strain curves of EM-rGO&MXene YSCs with 4% (b) and 6% (c) elongation, respectively	114
Figure 4.13	Optical image of hand knitted fabrics from EM-rGO&MXene fibers-based YSCs	115
Figure 4.14	(a) Ragone plot of areal (filled red) and linear (unfilled blue) energy density versus power density of EM-rGO&MXene YSCs and some reported YSCs: (A) biscrolled MXene@CNT/RuO ₂ @CNT asymmetric YSC; ²⁵⁰ (B) MnO ₂ /PPY/rGO@SSY YSC; ²⁵¹ (C) AC@CF YSC; ²⁴⁵ (D) NiCoO ₂ @SSY YSC; ²⁵² (E) MXene/Ag@Nylon YSC; ²²⁴ (F) MnO ₂ @CNT YSC; ²⁵³¹¹¹¹ (G) PPY/CNT@PU/Cotton YSC. ²⁵⁴ (b) Capacitance retention of YSC in different bending conditions. Inset: optical images of YSCs in different bending conditions. (c) Capacitance retention at different bending cycles with bending angle of 180°. (d) Schematic illustration of three YSCs in series and CV curves of single, two and three YSCs in series. (e) Schematic illustration of three YSCs in parallel and CV curves of single, two and three YSCs in parallel. (f) Optical image of a red LED powered by two charged YSCs connected in series.....	116

LIST OF ABBREVIATIONS

GO	Graphene Oxide
1D	One-dimensional
2D	Two-dimensional
rGO	reduced Graphene Oxide
LCs	Liquid Crystals
AC	Activated Carbon
CNT	Carbon Nanotube
DMF	N, N-dimethyl formamide
NMP	N-cyclohexyl-2-pyrrolidone
POM	Polarized Optical Microscopy
PP	Polypropylene
HPG	Hyperbranched Polyglycerol
GA	Glutaraldehyde
RH	Relative Humidity
OCPs	Organochlorine Pesticides
PDMS	Polydimethylsiloxane
EDLCs	Electrochemical Double-layer Capacitors
FSCs	Fiber-shaped Supercapacitors
GFs	Graphene Fibers
THF	Tetrahydrofuran
EG	Ethylene Glycol
IR	Infrared
HI	Hydriodic acid
SEM	Scanning Electron Microscope
PVA	Polyvinyl Alcohol
FTIR	Fourier-transform Infrared Spectroscopy
SSA	Specific Surface Area
MB	Methylene blue
EIS	Electrochemical Impedance Spectroscopy

OCGs	Oxygen-containing Groups
DI water	De-ionized water
DFT	Density Functional Theory
XRD	X-ray Diffraction
CV	Cyclic Voltammogram
GCD	Galvanostatic Charge/Discharge
ESR	Equivalent Series Resistance
YSCs	Yarn-shaped Supercapacitors
<i>c</i> -LP	<i>c</i> Lattice Parameter
EM	Electrolyte Mediation
LED	Light-emitting Diode

Chapter 1 Graphene Based Functional Fibers and Their

Applications in Energy-Storage Textiles

Graphene oxide (GO) is a wrinkled two-dimensional (2D) atomic layer of oxidized graphite, with the thickness around 1 nm and lateral dimensions varying between a few nanometers and tens of microns. On its basal plane and peripheries, there are sp^2 carbon-based lattices and various oxygen-containing functional groups (epoxy, hydroxyl and carboxyl groups).¹²⁻¹³ GO can be produced in large scale from pristine graphite by various wet-chemical processes, and used to be considered as an important precursor to graphene.¹⁴

Those reactive oxygenated groups on GO can be further modified or functionalized, leading to a variety of GO derivatives, with dramatically different physical and chemical properties. In addition, with the oxygenated groups, GO can be dispersed in water or some organic solvents through sonicating or mechanical stirring,¹⁵⁻¹⁶ exhibiting higher processability as compared to graphene. Therefore, solution processing of GO used to be considered as one of the most promising pathways to achieve the mass production of graphene.

Typically, GO is electrically insulating due to the large portion of sp^3 hybridized carbon atoms bonded with the oxygen-containing groups.¹⁷ Upon chemical reduction or thermal annealing, the electrical conductivity of reduced GO (rGO) can be improved at varying degrees up to several orders of magnitude. However, there is still a big gap between the graphene materials derived from GO and their mechanically cleaved counterpart in terms of crystallinity and carrier mobility, thus the consequent conductivity.¹⁸⁻²⁰ Since during GO synthesis, the harsh chemical oxidation environment creates lots of defects and vacancies within the sp^2 carbon lattice, which are difficult to recover by subsequent reduction.²¹ Therefore, to be clear, we will use the term rGO for the GO derived graphene in the following discussions.

GO can be taken as 2D building blocks to construct macroscopic materials through the bottom-up approaches. Upon reduction, homogenous rGO based materials can be formed in a macroscopic scale in various dimensions. Since the discovery of lyotropic liquid crystals (LCs) behavior of GO dispersion in 2011, the macroscopic one-dimensional (1D) GO fibers and subsequent rGO fibers up to meters and kilometers long, have been fabricated through a scalable wet-spinning technique.² Since then, a colossal amount of research activities have been devoted to optimizing the performance of the GO and rGO fibers in terms of mechanical, electrical, thermal and other properties. Apart from wet-spinning, some other fiber preparation methods, such as dimensionally confined hydrothermal strategy and direct film conversion,²²⁻²³ have also been developed. GO and rGO fibers have shown several promising applications in energy storage, light-weight conductor, actuator, and so on, which offer great potential to be seamlessly integrated into electronic textiles.

1.1. Fabrication of Graphene Based Fibers

Traditional fiber extrusion techniques for synthetic fibers include melting spinning from polymer melts and solution spinning from polymer solutions.²⁴ The low thermal stability of GO excludes its possibility in melt spinning, leaving solution spinning the major option. According to the intrinsic properties of spinning dopes and the fiber solidifying mechanisms, solution spinning can be further classified into various types, *i.e.* dry spinning, gel spinning, phase separation wet spinning and liquid crystalline wet spinning.

As the most accessible precursor of graphene, GO possesses good dispersibility in water and polar organic solvents, and can form lyotropic nematic LCs, a typical mesophase of highly anisotropic colloids, over a critical concentration.¹⁴ Inspired by the fabrication of carbon nanotube (CNT) fibers and Kevlar fibers from their liquid crystalline spinning dopes through liquid

crystalline wet spinning, GO fibers and subsequent rGO fibers were first developed *via* LC wet-spinning technique by Gao's group in 2011.² The LC wet-spinning technique ensures a continuous process to align 2D GO sheets along a uniaxial direction. Besides LC wet-spinning, other alternative methods have also been developed to fabricate GO/rGO fibers, such as dimensionally confined hydrothermal strategy and film conversion strategy *etc.*²²⁻²³

In the preparation processes of GO/rGO fibers, initial GO dispersions play a critical role in determining the processability and properties of the final fiber products. Thus, in this section, we will first discuss the properties of GO dispersions. Afterwards, we will introduce various fiber fabrication methods in detail.

1.1.1. Properties of GO Dispersions

The rheological nature of GO dispersion plays a critical role in solution assembly toward macroscopic fibers, thus the understanding of fluid physics of GO dispersions is of high significance. It decides the processability of fibers, such as the spinnability in LC wet-spinning, and the multiscale structure of formed macroscopic fibers.

GO, although synthesized *via* oxidation of graphite, retains the intrinsic anisotropic nature of graphene. GO's lateral size largely depends on the size of graphite precursor, and the level of oxidation, typically ranging from a few nanometers up to tens of micrometers.^{15, 25} The oxygenated functional groups including hydroxyl, carboxyl and epoxy on the sheets basal plane and peripheries, enable GO to be uniformly dispersed in water and some polar organic solvents, such as N,N-dimethyl formamide (DMF) and N-cyclohexyl-2-pyrrolidone (NMP). The concentration of stable GO dispersions in water can reach as high as 80 mg mL⁻¹.^{14, 16} The high anisotropy and good dispersibility of GO in good solvents ensure the formation of LCs.¹ According to Onsager's theory, the formation of nematic LC is entropy-driven, originating from the competition between

orientational and positional entropy.²⁶ However, this theory was established on rigid rods. In contrast, GO is a functionalized superflexible 2D material.²⁷ Other than losing orientational entropy during phase transformation, GO also loses considerable configurational entropy. In addition, it has been indicated that the electrostatic interactions and steric hindrance as well as the effect of solvent molecules among GO sheets should be taken into account for understanding the GO LC formation.²⁸

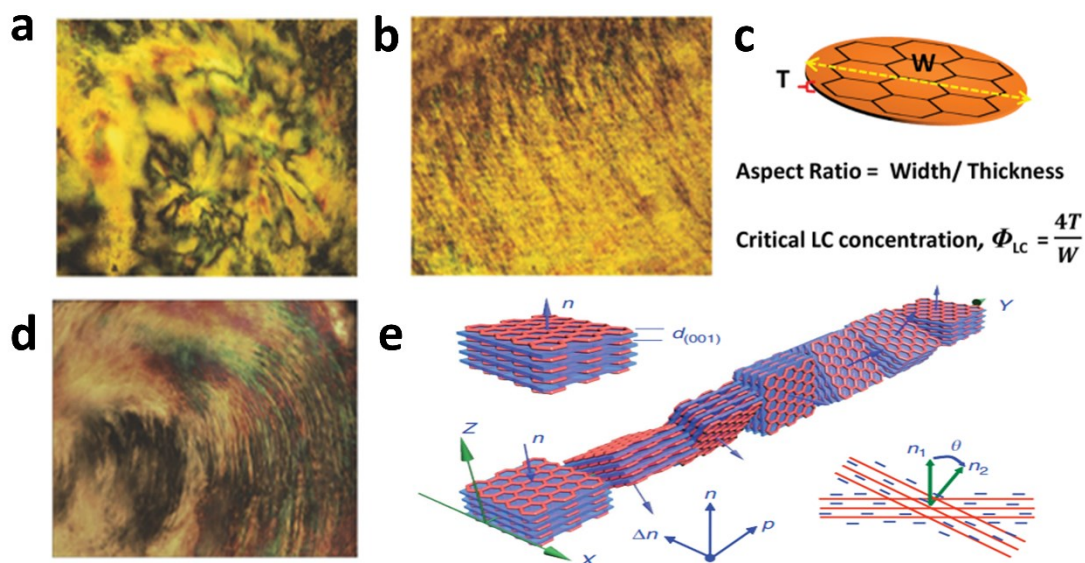


Figure 1.1 (a-b) typical POM images of nematic (a) and lamellar mesophases of GO LC dispersion (adapted from ref. 16);¹ (c) schematic illustration of the calculation of aspect ratio (adapted from ref. 3);¹⁴ (d) chiral mesophase of GO LC dispersion;² (e) proposed model for one pitch of GO chiral LCs (d and e adapted from ref. 11).²

The lyotropic liquid crystalline behavior of GO was discovered in 2011 by different research groups.^{1, 29-31} The phase transition of GO LC dispersion is largely depending on its concentration, which can be observed through polarized optical microscopy (POM). The studies by Xu *et al.*¹ showed that the isotropic-nematic transition for GO with a strong anisotropy of ~ 2600 (average lateral size of 2.1 μm and thickness of 0.8 nm) occurred at a low mass fraction

of 0.025 wt%. When the concentration was 0.5 wt %, a strong birefringent Schlieren texture with dark and bright brushes (Figure 1.1a) spread the whole dispersion, meaning the formation of nematic phase. As the concentration increased to 1 wt %, it showed regular lamellar structure (Figure 1.1b).

According to the equation $\Phi = 4T/W$ (T the thickness and W the lateral size of GO sheet) (Figure 1.1c), the larger the GO sheet, the higher the aspect ratio, thus the lower the critical phase transition concentration.²⁶ Aboutalebi *et al.* synthesized GO sheets with extremely high aspect ratio over 30 000, which led to the lowest reported critical concentration for LC transition of 0.1 wt%.³¹ In addition, the polydispersibility in the lateral size would cause the broad biphasic (isotropic & nematic) region of GO LC.¹ With a narrowly polydispersed GO (13% of the polydispersity, which is the relative standard deviation of the lateral size distribution),³² a new chiral mesophase with a long range helical twist-grain-boundary lamellar ordering was found besides normal nematic and lamellar phases, showing a typical fingerprint texture of cholesteric phase (Figure 1.1d).² The unique twisted lamellar structure is driven by the electrostatic repulsion between GO sheets boundaries. A model with a twist-lamellar block for the chiral GO LC was constructed as shown in Figure 1.1e.

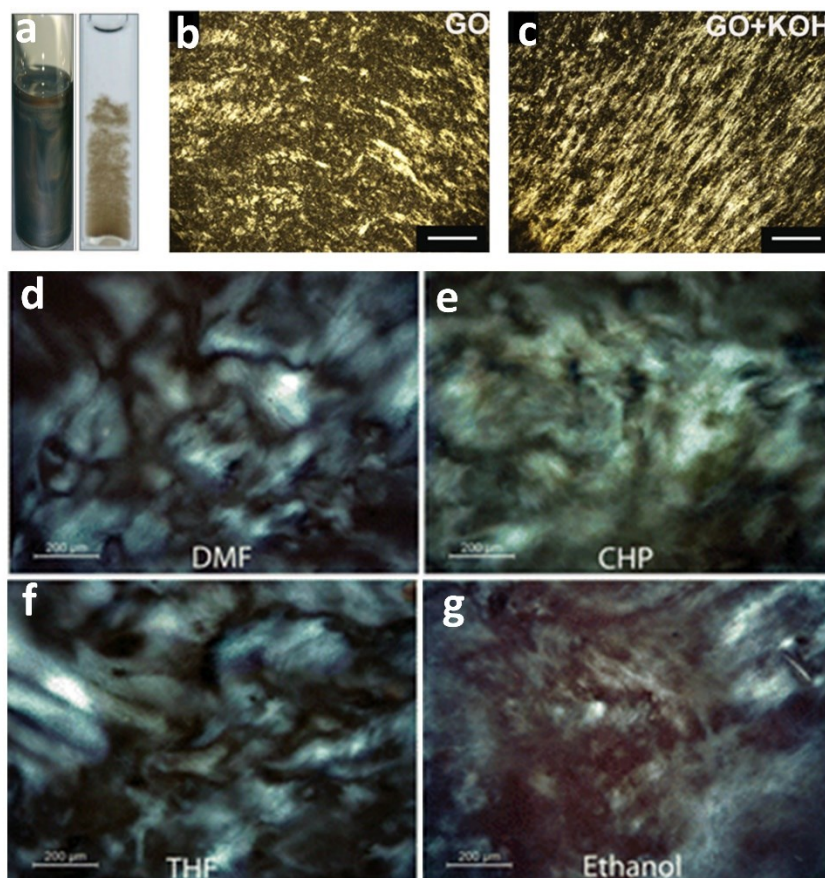


Figure 1.2 (a) left: aqueous GO LC dispersion (0.5 wt %); right: 0.01 wt % GO aggregate upon adding 50 mM NaCl (adapted from ref. 20);²⁹ (b-c) POM images of GO (b) and GO+KOH (c) dispersion, respectively (adapted from ref. 24);³³ (d-g) representative POM images of LC GO in various organic solvents at a concentration of 2.5 mg mL⁻¹ (adapted from ref. 25).³⁴

Thanks to the electrostatic repulsion between negative charges on individual GO sheet surfaces, GO can form stable dispersions in aqueous media. Meanwhile, it is crucial to remove acid and ionic impurities, which could deteriorate the repulsive electrostatic interactions, to ensure the long-term stability of GO LC formation.¹⁴ It is reported that 50 mM NaCl could induce GO sheets aggregate (Figure 1.2a).²⁹ On the contrary, strong bases such as KOH can induce the formation of highly oriented LC at a lower concentration, exhibiting an ordered laminar texture with highly aligned and continuous bands, as compared to that of pure GO dispersions (Figure

1.2b-c).³³ This is because the treatment with KOH can partially reduce GO, extending the rigid domains of GO sheets and enhancing the electrostatic repulsion between GO sheets, which lead to increased fluidity of the GO dispersion.

Apart from aqueous GO LC dispersion, researchers have also studied the GO LC behaviors in organic solvents. Wallace *et al.* demonstrated the GO LC phase in a wide range of organic solvents such as DMF, NMP, tetrahydrofuran (THF), ethanol, and acetone *etc.* (Figure 1.2d-g).³⁴ The phase transition concentration strongly depends on the intrinsic properties of solvents, such as solvent polarity, surface tension and the major interaction hydrogen bonding. However, they did not systematically study the long-term stability of these GO-LC dispersions in organic solvents.

In order to optimally fabricate GO macroscopic materials through solution assembly techniques, especially LC wet spinning, it is critical to understand the rheological behavior of GO LC dispersions. The studies from Xu *et al.* and Yang *et al.* revealed that the GO LCs exhibited shear thinning behavior, with reduced viscosity upon shearing and non-Newtonian flow curves with yield values (the threshold stress for the fluid to deform or flow),³⁵ as a result of LC alignment along flow direction.^{1, 36} Song *et al.*³⁷ studied the shear thinning behavior of GO LC dispersion through the analysis of scalar and biaxiality order parameters, which are the quantifying parameters of LC orientational order. They suggested both the ordering of individual GO sheets and inter-sheets interactions are the reasons for shear thinning behavior.

Specifically, for fiber spinning, the processability is referring to spinnability. Wallace *et al.*³⁸ studied the spinnability of GO LC dispersion as a function of concentration with the size of GO sheets fixed at ultra-large dimensions ($\sim 37 \mu\text{m}$). The full nematic phase was formed as the GO concentration increased to 0.75 mg mL^{-1} . In this region, its rheological behavior exhibited as a

plastic non-Newtonian liquid, which is suitable for wet-spinning.³⁹ The strong cohesion of the spinning dope was formed and long lengths of robust gel fibers were produced.⁴⁰

Wallace *et al.* also studied the spinnability of a range of GO dispersions with various GO sizes at fixed concentration (2.5 mg mL^{-1}).²⁸ The results showed that large-sized GO LCs ($> 1.5 \mu\text{m}$) behaved full nematic phenomenon and non-Newtonian flow curves with yield values, which was typical shear thinning fluids suitable for LC wet-spinning (Figure 1.3a). However, the small-sized GO sheets ($< 0.7 \mu\text{m}$) exhibited Newtonian flow curve with no yields and no spinnability (Figure 1.3b). GO dispersions with intermediate size carry a weak yield value that can only produce short length fiber.

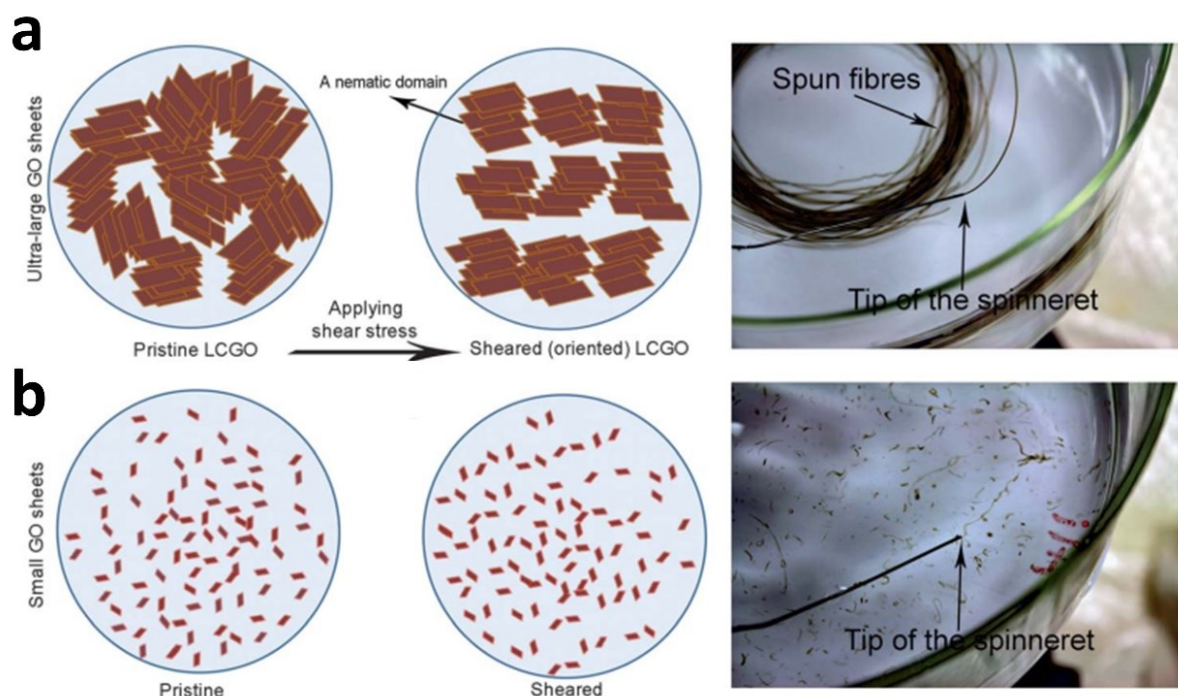


Figure 1.3 (a) Upon applying shear stress, nematic domains in large-sized GO LC dispersion are sheared and oriented along the direction of shear stress, resulting in continuous fibers *via* wet spinning; (b) in the case of small-sized GO with same concentration, no orientation is induced as applied shear force and found to be non-spinnable (adapted from ref. 19).²⁸

Other researcher also correlates the spinnability of GO LC dispersions with the GO size and concentration. Xu *et al.* reported that when the GO size was 21 μm , the critical concentration of the GO dope for spinning was 4 mg mL^{-1} ; and when the size was further reduced to 0.91 μm , the concentration increased to 81 mg mL^{-1} .^{2, 41}

The flexibility and high aspect ratio ($> 10^4$) of individual GO sheet, combined with strong sheet interactions (van der Waals, hydrogen bonds, etc.) are responsible for the assembly of continuous GO fibers. Even when infilled with metal nanowires^{3, 42} or modified with polymer molecules,⁴³⁻⁴⁶ GO dispersions still maintain their LC behavior and processability, resulting in various multifunctional GO and rGO fibers.

1.1.2. Wet-Spinning Method

Generally, wet spinning of GO fibers can be divided into three stages:

(1) An LC GO spinning dope undergoing shear force along the flow direction is extruded through a spinneret into certain coagulation bath.

(2) Solvent exchange between the spinning dope and coagulation bath, resulting in free-standing gel GO fibers. Meanwhile, the gel fibers are subjected to elongation stretch by rotating the coagulation bath or axial drawing by a collection unit, as shown in Figure 1.4a-b,⁴¹ promoting higher degree of alignment along fiber axis.

(3) Drying procedure. The evaporation of liquids in gel fiber brings the radial shrinkage, the buckling of GO sheets, and final compact stacking of solid GO fiber with typical wrinkled surfaces.

The subsequent rGO fibers can be produced by chemical or thermal treatment of GO fibers. The wet-spun GO fibers and rGO fibers can well inherit the orientational ordering of GO LCs in the flowing spinning dopes.

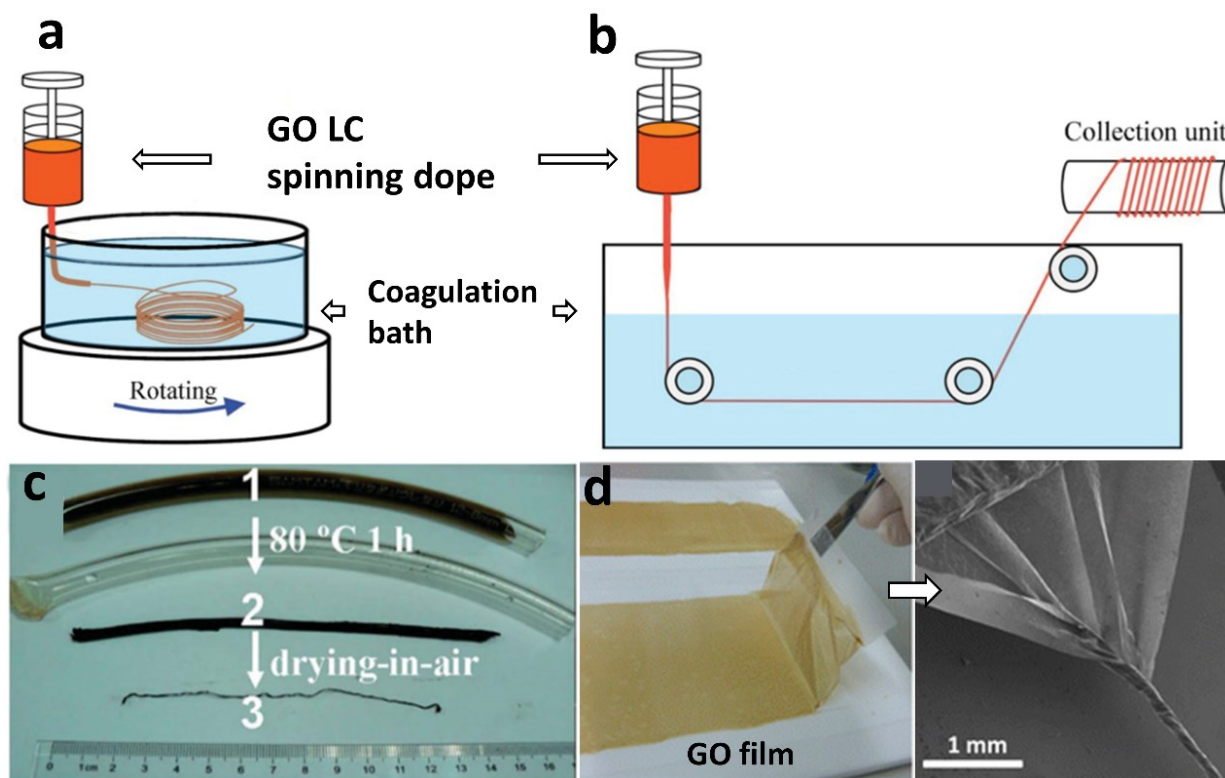


Figure 1.4 The schematic of wet-spinning processes from GO LC spinning dope, drawing by (a) a rotating coagulation bath and (b) a collection unit (adapted from ref. 32);⁴¹ (c) confined hydrothermal approach to rGO fibers, where GO was reacted with vitamin C in a PP pipeline for 1 h at 80°C, and then drying in air (adapted from ref. 12);²² (d) a GO film was cut into long strips and twisted into GO fiber (adapted from ref. 13).²³

Many parameters of wet-spinning can be utilized to control the structure and properties of GO/rGO fibers, such as solvent and concentration of GO, coagulation bath, draw ratio, the diameter of spinneret etc. Among them, the coagulation bath is one of the most important factors that determine the spinning process and fiber properties. Here are some coagulation methods: non-solvent precipitation (acetone, ethanol etc.), dispersion destabilization using acid, base or salt solutions (acetic acid, NaOH etc.), ionic cross-linking using multivalent cations (Ca^{2+} , Cu^{2+} etc.), and coagulation by amphiphilic or oppositely charged polymers (chitosan *etc.*).⁴⁰ The chosen of

coagulation bath is largely depending on the requirement of the final properties (mechanical, electrical, specific surface area etc.) of GO/rGO fibers and their applications. For example, the coagulation bath should have a balanced exchanging rate with the solvent of GO, in order to get a compact structure of GO fibers.⁴⁷ On the contrary, the rapid coagulation speed could result in porous fiber structure.⁴ In addition, the draw ratio is another important factor in determining fiber properties by controlling the orientation degree of GO sheets. By adjusting the ratio of coagulation rotation speed or fiber collection velocity to the spinning dope extrusion velocity, GO fibers with different draw ratio could be obtained.

1.1.3. Other Methods

Aside from the LC wet-spinning method, other strategies have also been developed to produce macroscopic GO/rGO fibers.

One available strategy is dimensionally confined hydrothermal approach.^{22, 48} Instead of extrusion into a coagulation bath, the GO dispersion (with or without chemical reduction agents) is injected into and sealed in a tube, then kept under suitable temperature. High temperature or chemical reduction can detach the oxygen-containing groups in GO, decreasing the electrostatic repulsion of GO sheets and inducing the precipitation to form a gel fiber. Afterwards, dry rGO fibers can be obtained by further removing the solvent. Li *et al.*²² injected GO together with reduction agent (vitamin C) dispersions into a polypropylene (PP) tube and heated to moderate temperature 80°C for 1h (Figure 1.4c). The GO was simultaneously reduced and assembled into a gel-state rGO fiber. After extraction and drying, an electrically conductive rGO fiber was obtained. By adjusting the mold structure and GO dispersion composition, this hydrothermal method was also used to fabricate hollow and composite rGO fibers.⁴⁹⁻⁵⁰ A certain degree of rGO sheet orientation could be observed, due to the capillary-induced shear forces and surface-tension-

induced sheet interactions. However, the sheet alignment is always inferior as compared to that produced *via* the wet-spinning method.⁴⁸ In addition, the hydrothermal method are inherently limited in scaling up to produce thousands of meters long fibers.

Film scrolling is another method to fabricate rGO fibers, usually with helical structures consisting of uniformly arranged loops. Large-area free-standing and flexible GO film with uniform and desired thickness could be easily prepared by coating GO solution onto a plane substrate such as PTFE plate or through film wet-spinning.^{23, 51-52} After cutting into narrow strips, GO films were suspended and twisted in a humid atmosphere by using an electrical motor to prepare helical GO fibers with tunable diameters (Figure 1.4d).²³ After reduction, GO fibers turned into helical rGO fibers.

GO LC dispersion is a useful host for various foreign guests, such as metal nanowires, nanoparticles and polymers, thus numerous GO based composite fibers with multifunctional properties can be fabricated. Confined hydrothermal approach and film converting approach are with low production efficiency and unsuitable for large-scale manufacturing. In comparison, wet-spinning is the most feasible technique for scale-up production of continuous fibers up to kilometers long. In addition, by modifying the structure of the spinneret and coagulation bath composition, core-shell, hollow, and porous fibers can be produced via wet-spinning protocols.^{4, 53-55} The characteristics and properties of GO and rGO fibers vary with the raw materials and synthesis method, which will be discussed in the following sections.

Table 1.1 Mechanical and electrical conductivity of GO/rGO fibers reported in literature.

Method	Fiber composition	Tensile strength/MPa	Young's modulus/GPa	Failure strain/%	Electrical conductivity/S cm ⁻¹
5 % NaOH/methanol bath, HI reduced ²	GO	102	5.4	10.1	---
	rGO	104	7.7	5.8	250
5% CaCl ₂ /H ₂ O bath, HI reduced ⁴¹	GO	364.4	6.3	6.8	---
	rGO	501.5	11.2	6.7	410
GO@DMF, ethyl acetate bath, HI reduced ⁹	rGO	360	---	10	280
	rGO&Ag	305	---	5.5	910-930
0.05% CTAB/H ₂ O bath, HI reduced ⁵⁹	GO	145	4.2	---	---
	rGO	182	8.7	---	35
Ethyl acetate bath, 1000°C annealed ⁶⁰	GO	214	47	0.61	---
	rGO				294
1% chitosan bath ⁴⁰	GO	442	22.6	3.6	---
1M NaOH bath, 220°C overnight ⁴⁰	rGO	115	9	---	2.8
GO&NaDC@H ₂ O, Ethanol bath, HI reduced ⁶¹	rGO	238	---	2.2	308
Liquid nitrogen bath, HI reduced ⁵⁵	GO	6.9	0.27	4.6	---
	rGO	11.1	0.35	6.2	20
GO&NaOH@H ₂ O, Acetic acid bath, HI reduced ⁶²	rGO	208	10.9	---	15.3
5% CaCl ₂ /H ₂ O bath, 1800°C annealed ⁶³	rGO	1080	77.6	1.5	1110
10% CaCl ₂ /H ₂ O bath (dry-jet) ⁶⁴	GO	135.8	7.9	5.9	---
GO@chlorosulfonic acid, ether bath, 1500°C (dry-jet) ⁶⁵	GO	33.2	3.2	1.64	---
	rGO	383	39.9	0.97	285
GO@DMF, ethyl acetate bath, 3000°C annealed ⁶⁶	rGO	1450	282	0.5	8000
GO@DMF, ethyl acetate bath, 3000°C annealed ⁶⁷	K-doped rGO	---	---	---	2.25*10 ⁵
GO@DMF, ethyl acetate&DCM bath, 2500°C annealed ⁶⁸	rGO with Ag electrodeposited	---	---	---	2.2*10 ⁵
GO&phenolic resin@H ₂ Oðanol, 2% CaCl ₂ /ethyl acetate&methanol bath, 1000°C annealed ⁶⁹	rGO&phenolic carbon (9/1)	1450	120	1.8	840
Ionic liquid bath, HI reduced ⁷⁰	GO	387.3	32.8	1.18	---
	rGO	412.2	10.7	3.48	181.9
5% CaCl ₂ /H ₂ O bath, HI reduced ⁴⁴	GO&HPG	452	8.31	5.4	---
	rGO&HPG	555	15.9	5.6	32.09
5% CaCl ₂ /H ₂ O bath, HI reduced ⁴⁵	GO&GMA	500	18.8	---	---
Hydrothermal, 230°C 2h ⁴⁸	rGO	180	---	4.2	ca. 10
Hydrothermal, 220°C 6h ⁵⁰	rGO	197	---	4.2	12
	rGO&CNT (1/1)	84	---	3.3	102
Hydrothermal, 80°C 6h ²²	rGO	150	1.9	20	8
GO film twisted, 2800°C annealed ²³	rGO	39.2	3.17	1.5	416

Note: in wet spinning method, unless other mentioned, the spinning dopes are aqueous pure GO dispersions.

1.2. Properties of Graphene Based Fibers

GO fibers consist of stacked and aligned 2D GO sheets, which can be easily turned into rGO fibers via chemical or thermal treatments. It is well known that graphene has extraordinary properties, such as the highest mechanical performance (tensile strength up to 130 GPa, modulus of 1100 GPa)⁵⁶, incredible electrical conductivity (10^8 S m^{-1}),⁵⁷ and the best thermal conductivity ($5300 \text{ W m}^{-1} \text{ K}^{-1}$).⁵⁸ However, as we mentioned before, rGOs derived from GO sheets have more defects, in comparison to their mechanically exfoliated counterparts. Apart from the properties of individual rGO sheets, the interaction between rGO sheets and how they are stacked together will also greatly influence the properties of final fibers. Therefore, numerous research efforts have been devoted to realization of those marvelous properties of pristine graphene with rGO fibers by optimizing fiber compositions and structures. Major endeavors include making rGO fibers with high mechanical properties, high electrical conductivity, high thermal conductivity and/or high surface area. In this section, we will describe these research activities in detail. Table 1 summarizes the mechanical and electrical conductivity of GO/rGO fibers reported in literature.

1.2.1. Mechanical Properties

GO/rGO fibers are expected to be strong and tough to withstand the processing and ultimate daily use. According to different applications, rGO fibers may also need to possess high modulus or high elasticity. For conventional polymeric fibers, molecular weight, chain-by-chain interaction and entanglement dominate the mechanical performance. In comparison, GO/rGO fibers composed of 2D flexible sheets display different interactions between basic constituent units. Specifically, the hierarchical and multiscale interactions encompass:^{44, 71-72}

- 1) chemical bonding between the GO/rGO sheets and/or the foreign components.

2) hydrogen bonding. The oxygen-containing groups on GO sheets can readily form hydrogen bonds. Even though the GO was reduced to rGO, there are still some residue oxygenated groups.

3) The van der Waals force.

4) Physical entanglement that originate from the wrinkles and folds of GO/rGO sheets.

In addition, according to the Griffith's criterion,⁷³ the randomly distributed defects in fibers and defect sizes influence fiber strength greatly. Thus, defect management is of great significance for achieving high strength fibers. Xu *et al.*⁶⁶ analyzed the defects in rGO fibers through its hierarchical structure, spanning from atomic to macroscopic scales (Figure 1.5), mainly including: 1) the atomic defects of individual rGO sheets; 2) nanoscale boundaries and voids; 3) inhomogeneous core-sheath structure and randomly orientated surface at the microscopic and macroscopic scales.

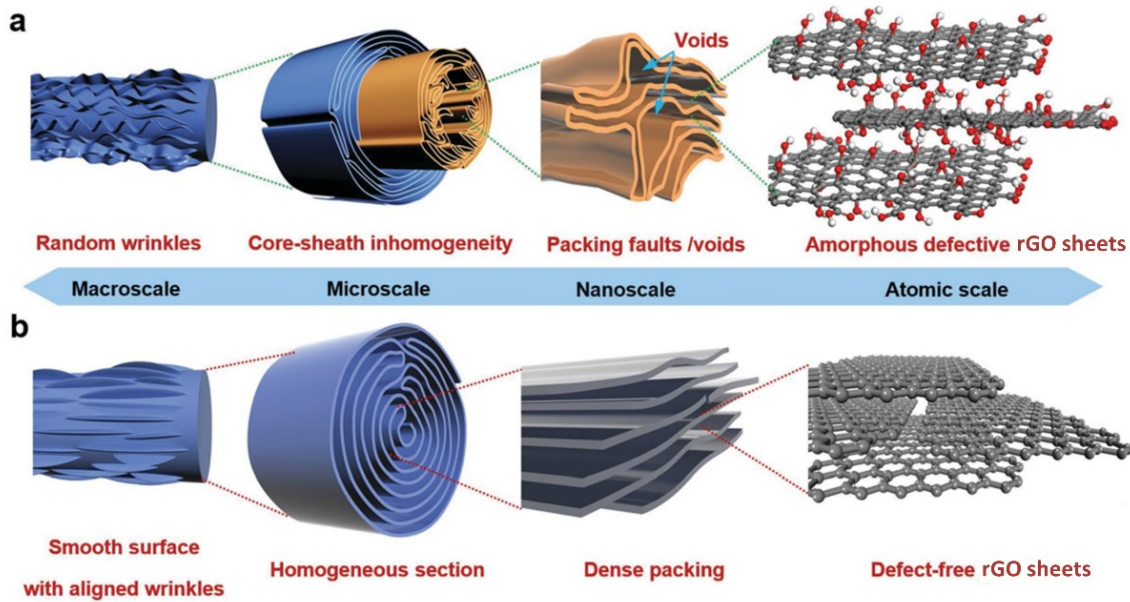


Figure 1.5 (a) Structural model of multiscale defects in rGO fibers, spanning from defective rGO sheets derived from GO after mild reduction; nanoscale boundaries and voids; inhomogeneous core-sheath structure and randomly orientation at microscale and macroscale; (b) structure model of rGO fibers with defects control at all levels (adapted from ref. 59).⁶⁶

By analyzing the interaction among basic constituent units and possible defects in GO/rGO fibers, several strategies could be applied to strengthen GO/rGO fibers: 1) decrease the boundaries and voids among 2D sheets by increasing the size of GO sheets, choosing suitable coagulants in wet spinning *etc.*; 2) enhancing GO/rGO sheets alignment by applying stretching; 3) perfect the atomic structure of rGO sheets by high-temperature graphitization; 4) increase interlayer interaction by introducing high energy covalent bonds.

Guided by these ideas, many efforts have been devoted to improving mechanical performances of GO/rGO fibers. Xiang *et al.*⁶⁰ studied the influence of lateral size of GO sheets and draw ratio during wet spinning to the mechanical performance of resulting GO fibers, respectively. They reported that the tensile strength of GO fibers spun from large-sized GO (22

μm) was 78 % higher than that of GO fiber spun from small-sized GO (9 μm). In this study, they also demonstrated that the alignment of GO sheets along fiber axis was optimized as the draw ratio increased from 1.09 to 1.45. As a result, GO fiber from draw ratio of 1.45 possessed the highest strength, as compared with those from lower draw ratios of 1.27 and 1.09. So far, most of the reported wet-spun GO/rGO fibers are fabricated with average GO size in the range of 15 μm - 40 μm .

Similarly, in order to achieve high strength fibers, Xu *et al.* chose GO sheets with average lateral size of 18.5 μm as building blocks to reduce defect boundaries and regulated the alignment of GO sheets along fiber axis by wet-drawing of GO gel fiber.⁴¹ In addition, divalent ions Ca^{2+} was introduced to form ionic bonding with GO sheets. After chemical reduction, as comparing to GO fibers, the tensile strength of rGO fibers increased by *ca.* 14% to 501.5 MPa and the modulus increased by *ca.* 77% to 11.2 GPa. Generally, after reduction, the tensile strength of rGO fibers will increase as comparing to GO fibers. Reduction enables most of the oxygen-containing groups to be removed, resulting in decreased layer distance and enhanced van der Waals force between layers. Thus, both the fiber linear density, tensile strength and modulus increase.^{65, 74}

Another common pathway to improve the fiber mechanical performance is to incorporate foreign molecules or polymer that can form covalent bonding with GO/rGO sheets. Hu *et al.*⁴⁴ grafted hyperbranched polyglycerol (HPG) onto GO sheets, and further used glutaraldehyde (GA) to form covalent acetal bridges between -OH groups of HPG and GO sheets, resulting in a high tensile strength of 652 MPa. Zhang *et al.*⁷⁵ introduced both ionic bonding with Ca^{2+} and covalent bonding with 10,12-pentacosadiyn-1-ol. The resulted rGO fibers exhibited both high tensile strength (842.6 MPa) and extraordinary toughness (15.8 MJ m^{-3}). Li *et al.*⁶⁹ improved the tensile strength of rGO fibers to 1.45 GPa and the modulus to 120 GPa by introducing phenolic carbon as

an effective cross-linkers, which could not only densify rGO fibers but also increase interfacial interaction among rGO sheets by forming new C-C bonds between rGO backbone and phenolic cross-linkers. Other polymers, such as chitosan,⁷⁶ polyacrylonitrile,⁷⁷ and poly(vinyl alcohol),⁷⁸ *etc.* have also been used to reinforce GO/rGO fibers. However, some polymers will dissolve or melting during the chemical or thermal reduction of GO fibers.

Recently, Gao's group demonstrated a full scale synergetic defect engineering protocol to minimize the possible defects at all levels from nano-scope to macro-scope.⁶⁶ 1) apply wet-drawing during wet-spinning process to realize regular orientation of GO sheets along fiber axis; 2) fabricate ultrafine GO/rGO fibers to submicrometer scale to decrease the probability of forming defects and voids; 3) high temperature graphitization at 3000°C to perfect the atomic structure of rGO. Under such synergetic defect engineering strategy, the strength of rGO fibers reached 2.2 GPa, the highest reported value so far.

1.2.2. Electrical Properties

The electrical property plays an important role in rGO fibers' application as flexible electrodes. Electrical conductivity of rGO fibers is depending on the following aspects: 1) the properties of individual rGO sheet in terms of structural defects and residue oxygenated groups which would deteriorate the carrier mobility; 2) the structure of rGO fibers, including the size and the alignment of rGO sheets. 3) the foreign components in rGO fibers.

Generally, rGO fibers are fabricated from GO fibers *via* a reduction process. Therefore, the reductive treatment is of critical importance in restoring the electrical conductivity of rGO sheets. There are two primary strategies for GO fiber conversion, *i.e.* chemical reduction and thermal annealing. The electrical conductivity of rGO fibers from chemical reduction was limited to the range of 20 to 400 S cm⁻¹, due to structural defects and residue oxygenated groups. Comparing to

chemical reduction, thermal annealing can lead to graphitization and remove oxygen-containing groups completely, thus giving birth to a significant increase in electrical conductivity up to $2\sim 8 \times 10^3 \text{ S cm}^{-1}$.^{63, 66} In addition, the higher the annealing temperature increases, the greater the electrical conductivity.²³

With respect to fiber structure, Chen *et al.* compared the conductivities of rGO fibers fabricated from large-size GO (30 μm) and small-size GO (5 μm), respectively. rGO fibers assembled from large-size GO had a conductivity 52% higher than that from the small-size GO. With respect to alignment, Chen *et al.* demonstrated that the conductivity of stretched rGO fibers was 87% higher than that of non-stretched fibers.⁶² Xin *et al.* fabricated a compact “intercalated” GO fiber structure by filling the space and voids among large-sized GO with small-sized GO (Figure 1.6a). After high temperature annealing, the electrical conductivity reached $2.2 \times 10^3 \text{ S cm}^{-1}$.⁶³

Foreign components will also largely influence the fiber electrical performance. rGO fibers with insulated polymer molecules incorporated, generally, exhibit low electrical conductivities ($< 10 \text{ S m}^{-1}$). On the contrary, the introducing of intrinsic conductive components could largely improve the electrical conductivity of final rGO fibers. For instance, silver nanowires greatly improve the rGO fiber conductivity to 930 S cm^{-1} .³ Gao’s group adopted post doping strategy to enhance the carrier density of rGO fibers by intercalating dopant (K, Br_2 and FeCl_3) into interlayer gallery of rGO sheets (Figure 1.6b).⁶⁷ The rGO fiber doped with K exhibited the highest conductivity up to $2.24 \times 10^5 \text{ S cm}^{-1}$, which was even comparable to that of metals like nickel. They also doped Ca to prepare a superconducting rGO fiber.⁷⁹ However, the K- and Ca-doped rGO fiber is unstable in air, largely limiting its practical applications. Recently, they applied electrodeposition to grow air stable metal (copper, silver, gold, nickel *etc.*) on thermal reduced

rGO fibers with electrical conductivity improved to metallic level (up to $2.2 \times 10^5 \text{ S cm}^{-1}$) (Figure 1.6c).⁶⁸

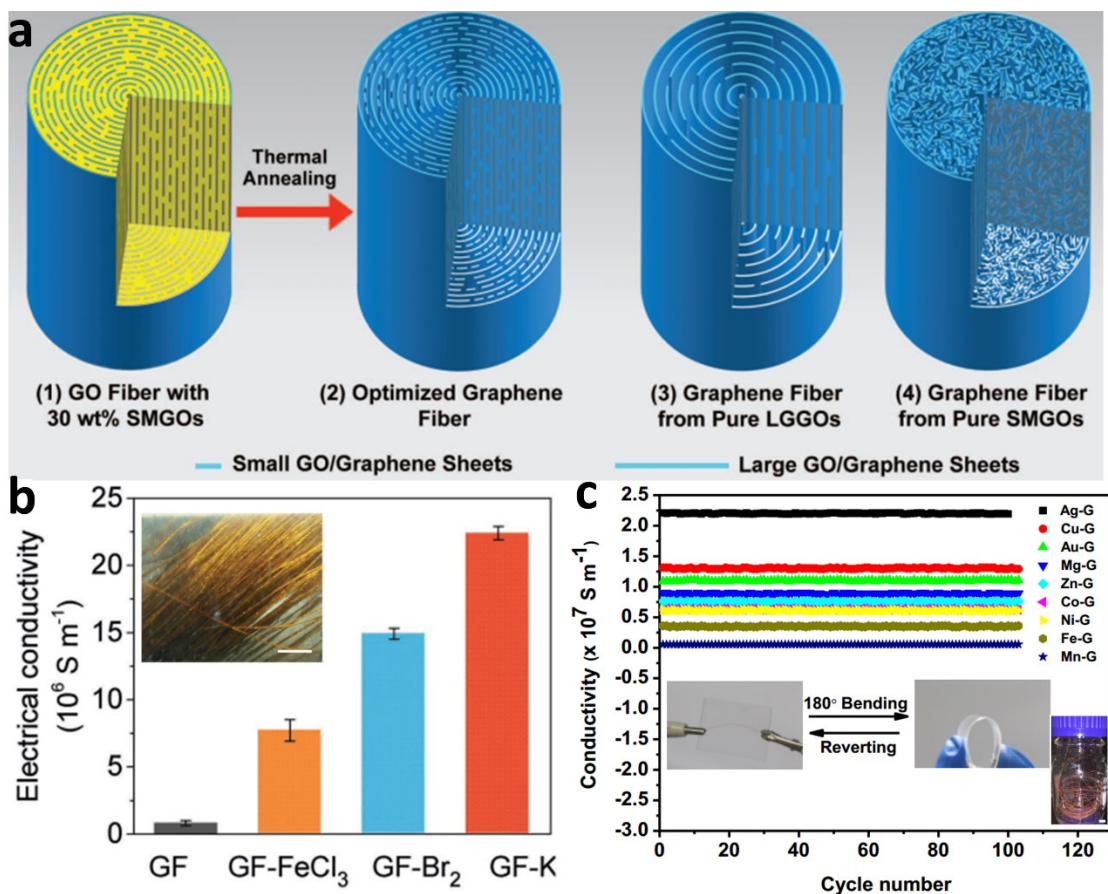


Figure 1.6 (a) Schematics of the “intercalated” structure of the GO and rGO fibers: large-sized GO sheets form the well aligned backbone, whereas small-sized GO sheets fill the space and voids between LGO sheets (adapted from ref. 33);³ (b) Electrical conductivity of pure rGO fibers and K, Br₂ and FeCl₃ doped rGO fibers. The insert is the photo of K-doped rGO fibers (adapted from ref. 60);⁶⁷ (c) the electrical conductivity changes of various metal coated rGO fibers under 100 cycles bending. The insert is the copper-coated rGO fibers (adapted from ref. 61).⁶⁸

1.2.3. Thermal Properties

For macroscopic rGO fibers with rGO sheets stacked, scattering of phonons by external boundaries or by large grain boundaries seriously limits the phonon mean free path, meaning the phonon-transport resistance increase.⁸⁰ Thus, in order to improve thermal conductivity of rGO fibers, larger GO sheets should be employed to decrease the defect boundaries for better phonon transportation. In addition, high-temperature thermal annealing is needed to completely remove oxygenated groups and recover the graphitic domain as much as possible, which is beneficial for increasing phonon mean free path.

Xin *et al.* reported highly thermal conductive rGO fibers with intercalated and compact structure by combining small-size and large-size GO.⁶³ After thermal annealing at 2850°C, the optimized rGO fibers expressed amazing thermal conductivity up to 1290 W m⁻¹ K⁻¹, about 3 times as high as that of copper. This result demonstrates potential applications of rGO fibers in the field of thermal management.

1.2.4. Surface Area

Due to the superflexibility of GO sheets, they are easily wrinkled during the fiber-assembly processes. In addition, by controlling fiber fabrication parameters, various fiber morphologies and porous structures can be obtained. Hitherto, hollow, porous, and core-sheath structure have been produced successfully.^{49, 53, 55} Therefore, the surface area of rGO fibers could be tuned by the assembly protocols. Usually the attribute of high surface area conflicts with good mechanical and electrical properties of rGO fibers due to the lower level of alignment and loosened structure.

Aboutalebi *et al.* fabricated porous rGO fibers with extremely high surface area of 2210 m² g⁻¹ (measured by methylene blue absorption) by modulating the diffusion rate of the solvent and coagulation bath during wet-spinning process (Figure 1.7a).⁴ By injecting GO dispersion into

liquid nitrogen following by freeze dry, Xu *et al.* fabricated highly porous GO/rGO fibers (Figure 1.7b).⁵⁵ Chen *et al.* used basified GO dispersion as spinning dope to fabricate rGO fibers with a willow-bark-like fine microstructure, resulting in ~30 % larger surface area as compared to fiber from normal GO dispersion (Figure 1.7c).⁶² They also demonstrated that fibers with lower draw ratio in wet-spinning process possessed more wrinkled morphology and larger surface area. However, all the porous and more wrinkled fibers showed inferior strength and electrical conductivities.

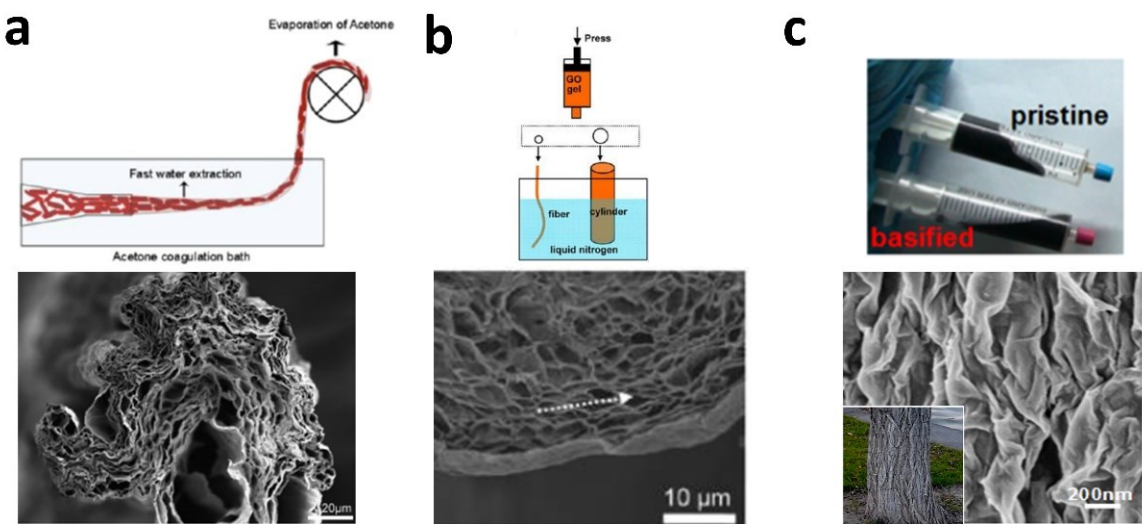


Figure 1.7 (a) Using an acetone coagulation bath results in the high rate of water extraction from the GO gel, leading to higher rate of solidification and porous fiber structure (adapted from ref. 40);⁴ (b) Inject GO dispersion into liquid nitrogen then followed by freeze-drying, resulting in porous fiber structure (adapted from ref. 48);⁵⁵ (c) The basified GO dispersion with better flowability results in wet-spun fiber with fine bark-like surface morphology (adapted from ref. 55).⁶²

Above all, GO/rGO fibers have demonstrated great potential in mechanical, electrical, thermal properties and can be tuned in surface area, enabling them in a broad range of practical

applications. It is still highly desired to fabricate fibers with large surface area and still maintain high mechanical and electrical conductivity.

1.3. Application in Electronic Textiles

As multifunctional fibers, GO/rGO fibers exhibit potential applications as electrodes in electronic textiles. Enormous research efforts have been focusing on wearable energy-storage devices, smart actuators, lightweight conducting wires, among others. In addition, the GO/rGO fibers are flexible and can be produced in large-scale, showing great potential to be easily integrated into multifunctional fabrics through knitting or weaving. Here, we mainly focus on the fibers with GO/rGO as main backbones, leaving alone other fiber substrates (natural fibers, synthetic fibers, or metal wires *etc.*) with GO/rGO coatings on surfaces.

1.3.1. Wearable Energy-Storage Devices

Due to flexible mechanical properties, good electrical conductivity, tunable surface area, as well as potential scalability, rGO fibers have been extensively explored as electrodes for flexible fiber-shaped supercapacitors (FSCs). These 1D FSCs are highly flexible and can be woven or knitted into fabrics with great design versatility in terms of shapes and locations.⁵

rGO fibers were first employed in supercapacitors by Qu's group in 2013.⁸¹ They fabricated a core-sheath rGO fiber (Figure 1.8a-b) consisting of a hydrothermal assembled rGO fiber as the core with a sheath of 3D porous rGO network. The twisted FSC with PVA/H₂SO₄ gel electrolyte showed a capacitance of 1.7 mF cm⁻² (27.1 μF cm⁻¹, 40 F g⁻¹), which was on the lower end. It was mainly due to the inferior electrical conductivity (12 S cm⁻¹) and a relatively small surface area (< 100 m² g⁻¹) of the rGO fibers in their system.

Since then, many efforts have been devoted to improving the electrochemical performance *via* structure optimization of rGO fibers or pseudocapacitive materials incorporation. Chen *et al.*

fabricated a pure rGO fiber with bark-like fine micromorphology (Figure 1.7c) and tunable porous structure by modulating wet-spinning process.⁶² The assembled solid-state FSC has specific capacitance of 226 F cm^{-3} , larger than that from most of the neat rGO fibers. High-crystalline graphene flakes tend to stack together densely, offering limited electrolyte accessible surfaces. CNTs have shown promises for reducing the stacking of graphene layers. Yu *et al.*⁵⁰ fabricated nitrogen doped-rGO and CNTs composite fibers (Figure 1.8c), resulting in a capacitance of *ca.* 300 F cm^{-3} for the solid state FSC, among the highest volumetric capacitances for carbonaceous materials.

Three FSC configurations have been demonstrated so far (Figure 1.8d), *i.e.* parallel, twisted, and coaxial.⁵ Compared with the other two configurations, the coaxial one provides the largest and most efficient interfaces between two electrodes, leading to the lowest solution resistance in the separation layer of a supercapacitor.⁸² Zhao *et al.*⁶ developed a coaxial FSC consisting of a continuously wet-spun rGO fiber, a dip-coated polymer electrolyte layer, and an rGO sheath coated subsequently (Figure 1.8e-f). This coaxial FSC had an areal capacitance of 205 mF cm^{-2} , much higher than the parallel aligned FSC.

In addition, pseudocapacitive materials have also been incorporated into rGO fibers to further improve the capacitance of FSCs, such as metal oxide (MnO_2 , *etc.*),⁸³⁻⁸⁴ and conductive polymer (ppy, *etc.*).⁸⁵ Recently, Yang *et al.* fabricated rGO and MXene composite fiber through wet-spinning (Figure 1.8g-h).⁸⁶ Thanks to the pseudocapacitive performance and high electrical conductivity of MXene, superior volumetric capacitance (586.4 F cm^{-3}) of the assembled FSC was achieved, exceeding most of those from pure rGO fibers.

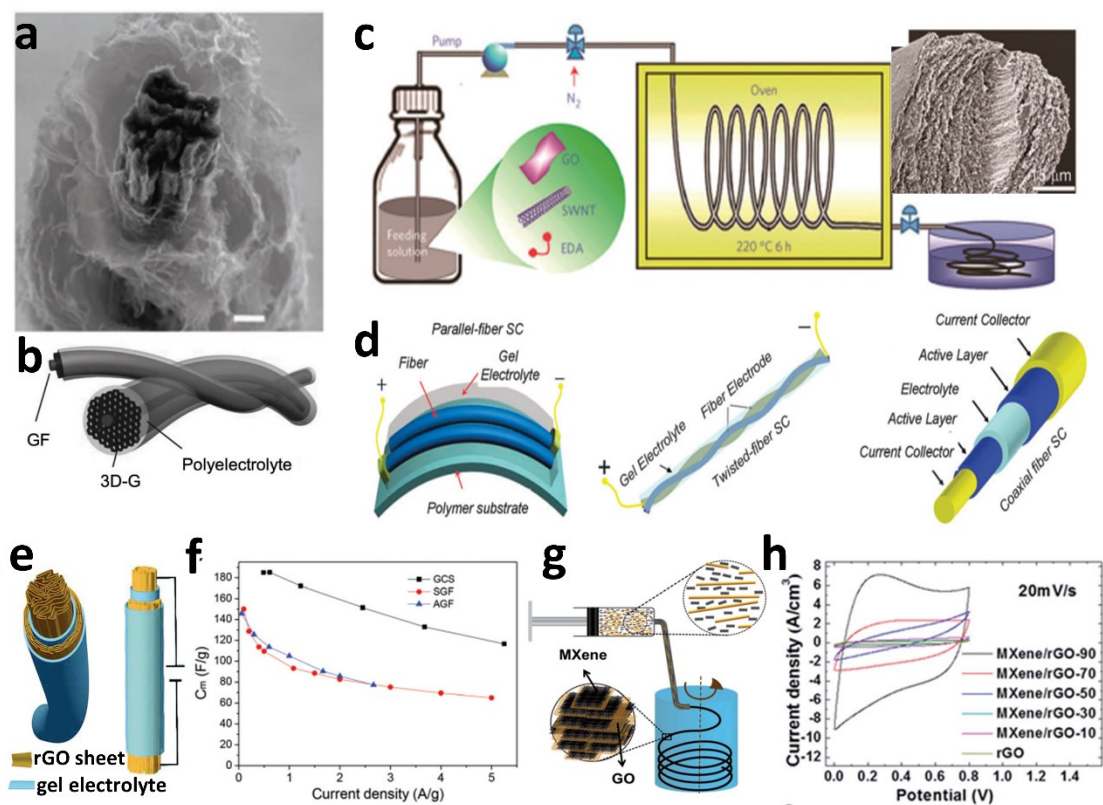


Figure 1.8 (a) Cross-sectional SEM image of core-sheath rGO fiber showing the core rGO fiber surrounding with amorphous rGO sheets;⁸¹ (b) schematic of two twisted rGO fibers assembled FSC (a and b adapted from ref. 75);⁸¹ (c) schematic illustration of the fabrication process of N-doped rGO and CNT composite fiber and its cross-sectional SEM image (adapted from ref. 43);⁵⁰ (d) three typical configurations of FSC: from left to right, parallel, twisted and coaxial (adapted from ref. 74);⁵ (e) schematic illustration of a coaxial FSC with a core rGO fiber and coated rGO sheath as electrodes;⁶ (f) the specific capacitance of FSCs with various structure at different current density, demonstrating the coaxial FSC has the highest capacitance (e and f adapted from ref. 77);⁶ (g) schematic of wet-spinning process for the MXene incorporated rGO fiber;⁸⁶ (h) cyclic voltammetry (CV) curves, demonstrating good capacitive performance of MXene and rGO composite FSC (g and h adapted from ref. 81).⁸⁶

Apart from the use as electrodes in FSCs, rGO fibers can also be used as fiber-shaped rechargeable battery. Recently, Hoshida *et al.* reported a novel fiber-shaped lithium-ion battery (LIB) electrode (Figure 1.9a-c),⁸⁷ which was fabricated by processing the titania into 2D rGO sheets through the wet-spinning strategy. The fiber-shaped LIB exhibited superior battery performance in terms of linear densities, rate capabilities and cyclic behaviors as well as excellent mechanical properties.

In addition, rGO fibers are also an alternative material for solar cells. Peng's group developed a novel archetype of wire-shaped dye-sensitized solar cell (DSSC).⁸⁸ The wet-spun rGO fiber with electrodeposited Pt nanoparticles was acting as counter electrode and Ti wire with TiO₂ nanotubes as working electrode (Figure 1.9d-f). The energy conversion efficiency of this DSSC achieved an amazing level of 8.41% when the Pt content was 7.1%, the highest among the wire-shaped photovoltaic devices.

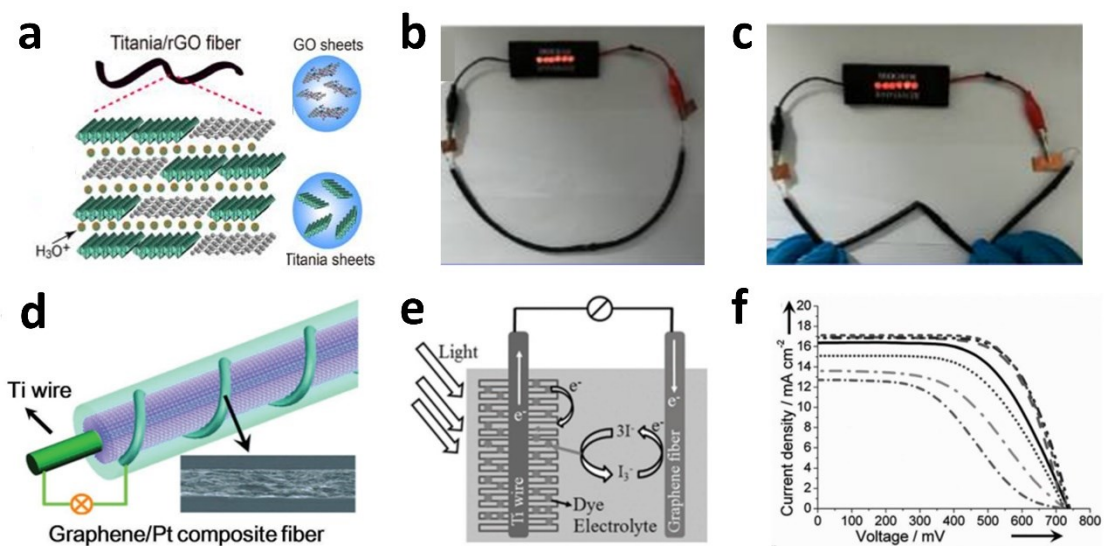


Figure 1.9 (a) Schematic illustration of the structure for the hybrid fiber of rGO/titania, which could be used as electrodes for fiber shaped batteries;⁸⁷ (b & c) the rGO/titania fibers assembled battery can light up 6 LED lamps under bending (a-c adapted from ref. 82);⁸⁷ (d) schematic of fiber shaped DSSC with rGO/Pt fiber as the counter electrode and a Ti wire with TiO₂ nanotubes as working electrode;⁸⁸ (e) working mechanism of the rGO fiber based DSSC;⁸⁸ (f) J-V characteristics of the DSSC with different Pt content as the counter electrode (d-f adapted from ref. 83).⁸⁸

1.3.2. Actuators

GO/rGO fibers have a variety of actuating properties and can undergo deformation or mechanical property changes in response to the external stimulus, such as electricity and humidity *etc.* Qu's group developed a series of GO-based moisture triggered actuators with versatile functionalities. They developed a mini-moisture-sensitive actuator, which is a region-asymmetric rGO/GO fiber.⁸⁹ The GO fiber was partially laser reduced, resulting in different wetting behavior between the two parts on one fiber, *i.e.* rGO part and GO part (Figure 1.10a-b). The oxygen containing groups on GO sheets and relative larger interlayer distance facilitate the fast incorporation or evaporation of water molecules into or out the GO part. When the fiber was

exposed in high relative humidity (RH) up to 80 %, it bends rapidly to the rGO side. The fiber will recover to its initial state as the RH regressed to 25 %.

Another study from the same group was about a humidity-triggered GO fiber-based electronic switches and electric generators.⁹⁰ A GO fiber with spiral structure was prepared by twisting the freshly wet-spun GO hydrogel fiber (Figure 1.10c-d). When exposed to alternating RH conditions, the fiber can be reversibly untwisted or further twisted by water molecules diffusing out or in (Figure 1.10e). This special moisture-driven torsional actuation was harnessed to be a humidity switch and alternating current generator (Figure 1.10f-g).

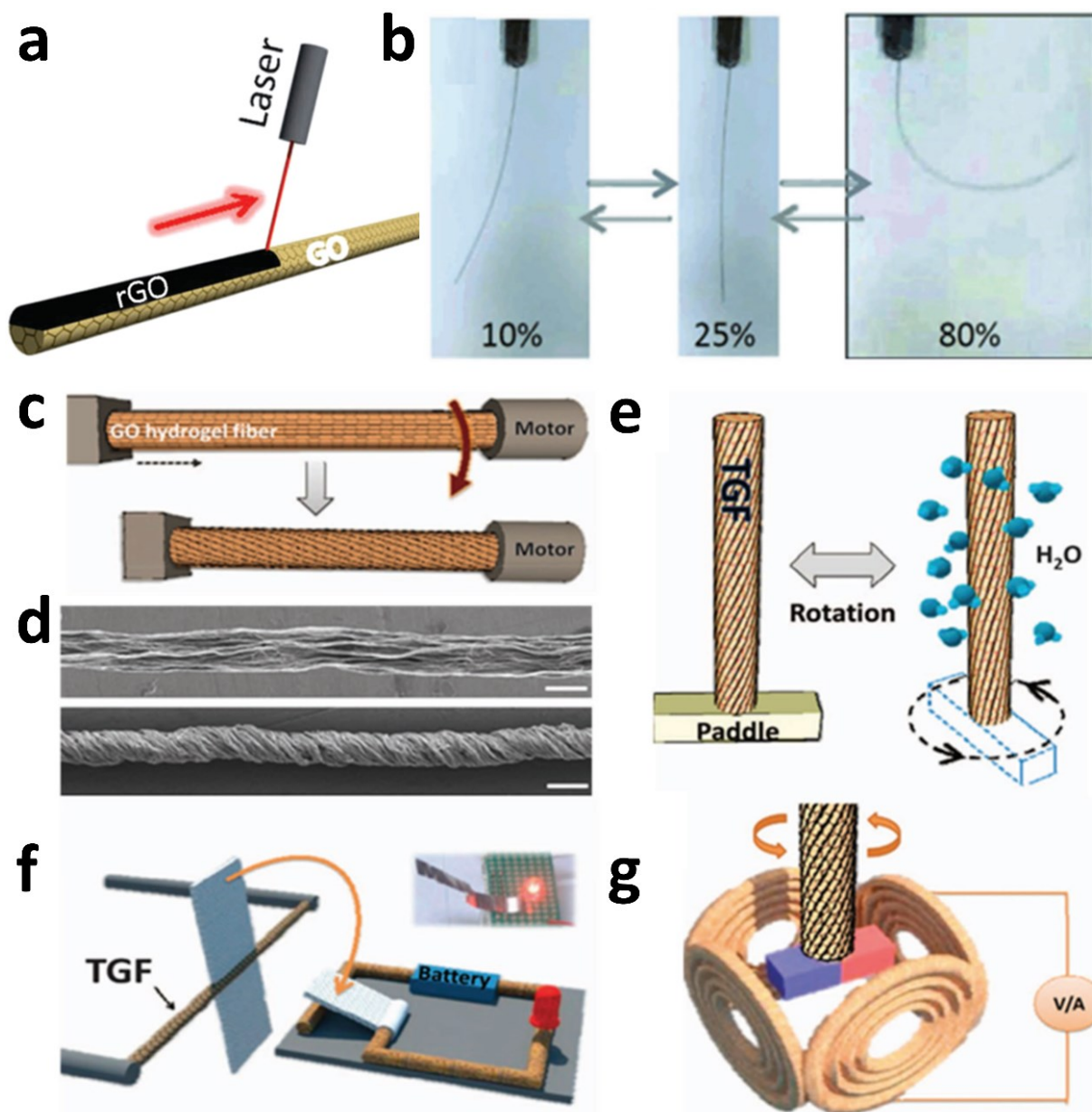


Figure 1.10 (a) Schematic showing the positioned laser reducing of GO fiber;⁸⁹ (b) photos of a GO/rGO fiber under different RH condition (a and b adapted from ref. 84);⁸⁹ (c) schematic showing the twisting process of GO fiber with spiral structure;⁹⁰ (d) SEM images of directly GO fiber and twisted spiral GO fiber;⁹⁰ (e) schematic illustrating showing that a spiral GO fiber can be driven to rotate by varying RH;⁹⁰ application of the spiral GO fiber as a humidity switch (f) and electric generator (g) (c-g adapted from ref. 85).⁹⁰

1.3.3. Lightweight Conductors

The electrically conductive rGO fibers due to the much lower density and higher flexibility than that of metal wires, hold great promises in lightweight and wearable electronic textiles.

The electrical conductivity of rGO fibers varies in a large range, strongly depending on the reduction method and post-treatment. The chemically reduced rGO fibers with limited electrical conductivity of 20-400 S cm⁻¹, which is far less than that of metal wires, can only be connected into circuits with limited length, usually at centimeter-scale,⁷² since its large electrical resistance will share a big portion of the applied voltage. As a comparison, the electrical conductivity of rGO fibers from thermal annealing can increase by one order of magnitude. In addition, the study from Gao's group showed that the ampacity (2.3×10^{10} A m⁻²) of such rGO fibers was higher than that of pure copper, suggesting its potential usage as electrical cables to carry heavy current.⁶⁶ In terms of density, the linear density of rGO fibers is only 12.5 % of that of copper wire. Recently, Gao's group have raised the electrical conductivity of rGO fibers to 10⁴-10⁵ S cm⁻¹ by means of chemical doping or electrodeposition,⁶⁷⁻⁶⁸ making rGO fibers a promising substitute for metal wires for lightweight electrical conduction.

1.3.4. Other Applications

Besides the above-mentioned applications that are mostly studied, some other interesting functions were also explored.

Recently, Gao's group modified wet-spinning process to prepare staple GO fibers instead of continuous filament, and assembled them into non-woven rGO fabric (Figure 1.11a).⁹¹ The rGO non-woven fabrics demonstrated porous structure and decent mechanical flexibility, as well as good electrical and thermal conductivity, carrying great potential for applications in oil adsorbents, porous supercapacitor electrodes and electrochemical heaters.

Cruz-Silva *et al.* demonstrated the application of rGO fibers as field emitters.²³ Their rGO fiber was made by scrolling dry GO film followed by annealing at 2000°C, which offered superior field-emission properties with low turn-on voltage at 0.48 V μm^{-1} (Figure 1.11b-e), lower than those of CVD-grown graphene sheets in few layers (4.7 V μm^{-1}) and electrophoretic-deposited single-layer graphene film (2.3 V μm^{-1}). The good field emission properties are due to the well-oriented rGO sheets along fiber axis and the topological defects at the sheets' edges, which were believed to act as effective emission sites.

Apart from the application in smart textile as electronics, rGO fiber can also work as a good solid-phase microextraction sorbent. Luo *et al.*⁹² demonstrated that a hydrothermally fabricated rGO fiber had better absorption performance for organochlorine pesticides (OCPs) than a commercially used polydimethylsiloxane (PDMS) fiber.

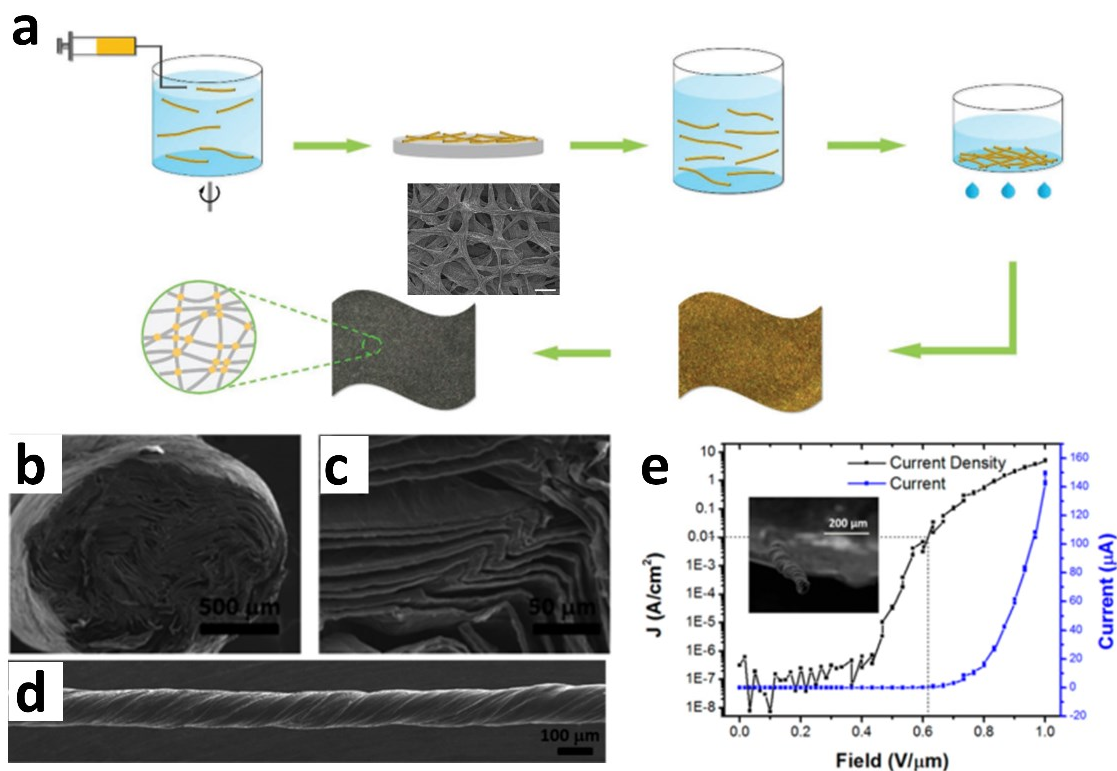


Figure 1.11 (a) Schematic illustration of fabrication process of rGO staple fiber based non-woven fabric. The inserted is the SEM image of the porous fabric (adapted from ref. 86);⁹¹ (b-d) SEM images of GO fibers via scrolling dry GO film;²³ (e) I - E curve for the thermally reduced film scrolled GO fiber (b-e adapted from ref. 13).²³

1.4. Concluding Remarks

GO as a 2D flexible sheet with rich oxygen containing groups, can be well dispersed in water and other organic solvents, which can exhibit liquid crystalline behavior at certain concentrations. These intrinsic properties enable GO sheets to be easily assembled into 1D macroscopic fibers *via* solution assembly. Upon chemical reduction or thermal annealing, GO fibers can be converted to rGO fibers, imposed with electrical and thermal conductivities.

In this chapter, we have summarized and discussed the properties of GO LC dispersions and fiber fabrication methods. Among all the methods, wet-spinning is the most commonly used

strategy to fabricate large-scale continuous GO fibers. By modulating fabrication parameters and/or introducing foreign components, such as nanoparticles, polymers *etc.*, the neat or composite GO fibers with various structure can be obtained for targeted applications. Many efforts have been devoted to make fibers with desired mechanical performance, high electrical conductivity, outstanding thermal conductivity, or large specific surface area. The basic understanding of structure and properties of GO/rGO fibers are established, and the critical control parameters have also been clarified, including the lateral size and alignment of GO sheets, and the interactions between them. The applications of GO/rGO fibers have also been categorized and discussed. Due to the versatility in structural engineering, GO/rGO fibers can be applied in energy storage devices, lightweight conductors, actuators, field emitters, and so on.

Meanwhile, it is still highly desirable to fabricate GO/rGO fibers with combined properties for specific applications. For example, an rGO fiber with high strength, high electrical conductivity and large surface area is highly favored as an electrode in FSC, but so far hasn't been full achieved. In addition, fundamental understanding is still missing on the fiber structure evolution during the extrusion and coagulation processes, as well as on the deformation of GO sheets in the gel to solid transition and the formation of multiscale wrinkles. The structure-property relationship is yet to be clarified. Although people have made impressive progresses on GO/rGO fiber applications, marketable products and large-scale manufacturing are still far away from occurring.

Chapter 2 Graphene-Fiber-Based Supercapacitors Favor N-Methyl-2-Pyrrolidone/Ethyl Acetate as the Spinning Solvent/Coagulant Combination

2.1. Introduction

The term “smart-clothes” has been applied over the past few years to refer to the attachment of commercial (rigid) electronic devices to an article of clothing with applications mostly in performance sports or futuristic fashion shows. An actual smart fabric comprising the seamless integration of soft (flexible) electronics within the textile itself is still mainly in the R&D and prototyping stages at prohibitively high manufacturing costs. Recently, fiber-based energy-storage systems have attracted enormous attention due to their remarkable promises in smart textiles, implantable medical devices, portable military equipment, high-tech sportswear *etc.*, mainly as more pliable energy-storage units being truly “wearable”.⁹³⁻⁹⁵ 1D fiber-shaped devices with small volumes can be easily assembled into various textile structures through weaving or knitting to maximize mechanical flexibility and compliance, comparing to 2D thin-film devices.⁹⁶⁻⁹⁸ As for energy-storage devices, supercapacitors (also known as Electrochemical Double-layer Capacitors (EDLCs)) are favored over batteries due to their fast charge-discharge rate, long cycling life and good stability,⁹⁹⁻¹⁰⁰ but still need improvements in their energy densities and current leakage.¹⁰¹⁻

102

In most fiber-shaped EDLCs (FSCs), metal wires have been adopted as current collectors due to their high conductivity.¹⁰³ However, metal wires are heavy, uncomfortable, and abrasive, resulting in low gravimetric/volumetric energy/power density of FSCs.⁵ Alternatively, conductive, lightweight, and flexible carbonaceous fibers can be used as both current collectors and active

materials.¹⁰⁴⁻¹⁰⁵ Carbon nanotube (CNT) fibers have been demonstrated as fiber electrodes.¹⁰⁶ Nevertheless, CNT is costly and toxic to human body,¹⁰⁷ thus will hamper the scale-up of this device and its application in direct contact with human bodies. In contrast, cost-effective and biosafe graphene fibers (GFs) are more promising for FSCs applications.¹⁰⁸ GFs have been prepared by scrolling of chemical vapor deposition graphene films,¹⁰⁹ hydrothermal assembly of graphene oxide (GO) dispersion in a pipelines,⁴⁸ and wet spinning of GO dispersion followed by chemical reduction.^{2, 47, 66, 91, 110} Among all these protocols, the industrially viable wet-spinning process is the most promising pathway to produce continuous and long GFs.^{72, 79} Reduced GO (rGO) has been reported as an excellent electrode material for EDLCs because of its high surface area, good electrical conductivity and easy processability.^{7, 111-113}

GO dispersions have been discovered to form liquid crystals (LCs) at certain concentrations.² Wet spinning from LC dope is a feasible way to make robust fibers, in light of strong Kevlar fibers and CNT fibers.¹¹⁴⁻¹¹⁵ Wet spinning is a process of spinning polymer solutions or other LCs (such as GO dispersions) into a liquid bath called the “coagulation bath”.¹¹⁶⁻¹¹⁷ A diffusional interchange, *i.e.* coagulation, between the freshly formed fluid filament and the bath causes the solute to solidify. This spinning dope composition as well as the coagulation bath will largely influence the surface morphology and inner structure of the as-spun polymeric fibers, and later impact the mechanical, electrical and electrochemical behaviors of these fibers. Therefore, it is critical to choose an appropriate solvent for GO dispersions and a good coagulation bath. Chen *et al.* has basified the aqueous GO dispersion into non-LC, and spun it for the production of rGO fibers (rGO-Fs), in order to create fine microstructures with enhanced specific capacitance, but it also resulted in 80% lower conductivity than that of LC-spun fibers.¹¹⁸ Abouralebi *et al.*¹¹⁹ found that rGO-Fs spun *via* acetone coagulation bath could give higher capacitance over CaCl₂ bath.

However, the mechanical properties of acetone-based rGO-Fs were only 49 MPa, almost 10 times lower than CaCl₂ coagulated rGO-Fs. Ca²⁺ ions are known to crosslink GO,¹²⁰ so that it improves the mechanical strength of rGO-Fs but also leads to more compact structure with less surface for ion adsorption. Till now, challenge remains on scalable fabrication of highly conductive and mechanically strong GFs with fine-tuned microstructures as FSC electrodes.

As we known, GO can be well dispersed in H₂O and polar organic solvents, such as *N*-methyl-2-pyrrolidone (NMP), *N,N*-dimethylformamide (DMF), ethylene glycol and tetrahydrofuran (THF) and ethylene glycol (EG).¹⁵⁻¹⁶ Among these available solvents, water, DMF and NMP dispersions possess comparatively larger dispersing capability and long-term stability.¹⁶ In addition, Konios *etc.* also suggested that NMP with high dipole moments and close surface tension to GO surface energy, exhibits the highest solubility and significant long-term stability, being the most efficient solvents for the dispersion of GO among organic systems.¹²¹ NMP is widely used as solvent for polymer wet spinning.¹²²⁻¹²³ Until now, the most reported wet-spun GO fibers are H₂O based^{40, 118, 124-126} and few are DMF based^{67, 127} and chlorosulfonic acid based¹²⁸. No comparison on the structure, properties and electrochemical performance of rGO-Fs derived from various spinning-dope solvents has been explored so far.

In the present work, we have fabricated continuous rGO-Fs from GO dispersions in NMP, with ethyl acetate as the corresponding coagulant. The resulted fibers showed wrinkled morphology and porous structure which facilitate the adsorption and diffusion of electrolyte ions. Owing to this unique structure, these NMP-based rGO fibers (rGO@NMP-Fs) exhibited twice higher toughness at comparable tensile strength (~93 MPa) and electrical conductivity (~60 S cm⁻¹), as compared to H₂O-based rGO fibers (rGO@H₂O-Fs). They also demonstrated fivefold higher capacitance as compared with H₂O-based rGO FSCs (rGO@H₂O-FSCs). In addition, the NMP-

based rGO FSCs (rGO@NMP-FSCs) exhibited good cycling and bending fatigue retention with volumetric energy density and power density up to 6.8 mWh cm^{-3} and 1183 mW cm^{-3} respectively, among the highest values of recently reported FSCs.

2.2. Experimental Section

2.2.1. Synthesis of GO

GO was prepared from the oxidation of graphite powders following a modified Hummers method.^{124, 129} The graphite (500 μm , Asbury Graphite Mills, US) were expanded by microwave (750 W) irradiation for 90 seconds. Then the expanded graphite powder was pretreated to facilitate further oxidation. For the pretreatment, concentrated H_2SO_4 (50 mL) was heated to 90°C in a 300 mL flask, and $\text{K}_2\text{S}_2\text{O}_8$ (10 g) and P_2O_5 (10 g) were added successively with magnetic stirring of the solution. After all reactants were completely dissolved, the mixture was cooled down to 80°C and the expanded graphite (12 g) was added into the solution. The mixture was kept at 80°C for 24 h, after which the heating was stopped, and the mixture was diluted with 2 L of de-ionized (DI) water. Then the mixture was vacuum filtered and washed with DI water until the pH was neutral. The solid was dried in air at room temperature for two days. For the oxidation step, the pretreated graphite powder was added to the flask containing concentrated H_2SO_4 (460 mL) in an ice bath (0°C). KMnO_4 (60 g) was added slowly and allowed to dissolve with the aid of stirring. The mixture was then allowed to react at 35°C for 12 hours, after which DI water (920 mL) was added slowly in an ice bath. Shortly after that another 2.8 L DI water and 50 mL of 30% H_2O_2 was added to the mixture resulting in a brilliant yellow color along with bubbling. The mixture was settled and washed with DI water and 10 % HCl repeatedly until neutral to get the final concentrated GO dispersion. The GO dispersion was dried and the solid was collected to prepare the desired spinning dope.

2.2.2. Fiber Spinning

For GO@H₂O-F, the water-based GO dispersion was injected into glacial acetic acid in a rotating plate through a 22 G hollow needle at a rate of 1.5 m min⁻¹. The end of the needle was placed tangentially 35 mm away from the center of rotation, and the rotation speed was adjusted to form draw ratio at 1.5. The wet fibers were drawn out vertically along the infrared (IR) lamp and wound onto a bobbin. For GO@NMP-F, the NMP-based GO dispersion was spun at the same condition, except for the use of ethyl acetate as the coagulation bath. In addition, we obtained GO@NMP-F at different draw ratios (1.5, 1.75 and 2) for study of fiber orientation.

The GO fibers were reduced by hydriodic acid (HI) solution (45 wt %) at 80°C for 8 h, washed with water and ethanol alternatively 3 times, and dried at 80°C under vacuum for 12 h to obtain rGO-Fs.

2.2.3. Structural Characterizations

POM images of the GO dispersion were taken with a Nikon polarized light microscope. The rheological behavior of GO dispersions was evaluated by an ATS RheoSystems STRESSTECH rheometer (TA Instruments, USA) using cone-plate geometry. The morphology of GO and rGO fibers were observed on scanning electron microscope (SEM). Mechanical property test was conducted with an Instron material testing system at a strain rate of 1 mm/min at a gauge of 10 mm. The conductivity was measured by the four-point probe method (Figure 2.1). The fiber cross-section area used for calculating mechanical and electrical conductivity properties were based on the circle with a diameter equal to the largest diameter of the irregular fiber cross sections. The orientation of rGO sheets was measured by polarized Raman spectroscopy (BaySpec Nomadic Raman Spectrometer) with 532 nm laser excitation.

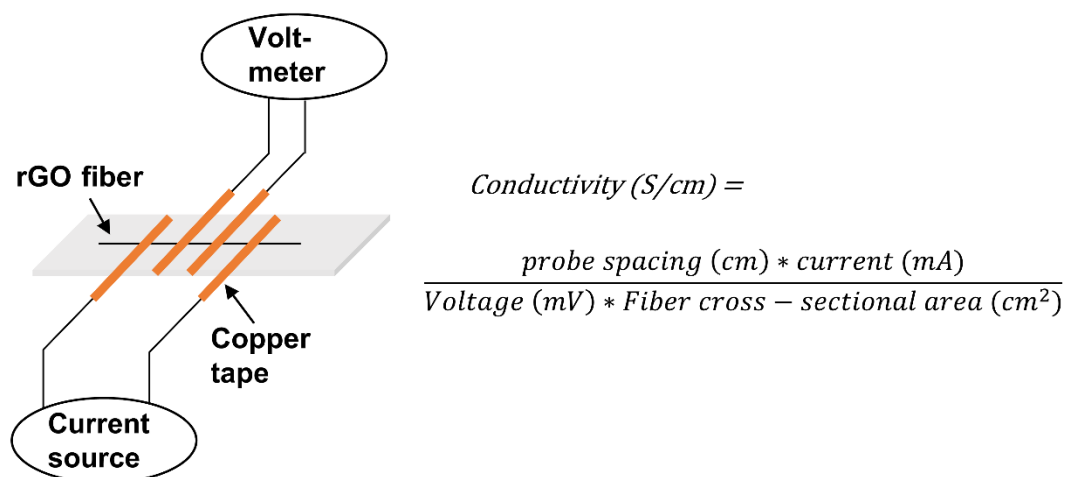


Figure 2.1 Fiber four-point probe setup for electrical conductivity measurement.

The specific surface area (SSA) of rGO-Fs was measured by MB adsorption method.⁷ A known mass of rGO-Fs (~10 mg) was added to the aqueous MB solution with concentration of 1 mg ml⁻¹. Then the solution was stirred for 24 hours to reach maximum adsorption. The concentration of MB in supernatant was measured by UV-vis spectrometer at 665 nm. The SSA was calculated by the equation: $SSA = \left(\frac{m_{MB}}{M_{MB}}\right)A_V A_{MB} \left(\frac{1}{m_{fiber}}\right)$, where m_{MB} is the mass of the adsorbed MB, M_{MB} is the molar molecular weight (319.87 g mol⁻¹) of MB, A_V is Avogadro's number (6.02×10^{23} /mol), A_{MB} is the area covered by one MB molecule (assumed to be 1.35 nm²) and m_{fiber} is the mass of rGO-F.

2.2.4. Electrochemical Performance Characterizations

To assemble a solid-state flexible FSC, two rGO-Fs (1.5 cm in length) were aligned in parallel, soaked with a gel electrolyte of H₂SO₄/Polyvinyl alcohol (PVA)/H₂O (1/1/10 in weight), and dried at room temperature. CV, GCD, and EIS measurements were performed using an electrochemical workstation (Autolab, Metrohm, USA).

The specific volumetric capacitance (C_V), mass capacitance (C_M), area capacitance (C_A) and length capacitance (C_L) of the electrode in a two-electrode cell was calculated according to $C_V = 2C/V_{fiber}$, $C_M = 2C/M_{fiber}$, $C_A = 2C/S_{fiber}$, and $C_L = 2C/L$ respectively, where C is the measured two-electrode configuration FSC capacitance, V_{fiber} , M_{fiber} and S_{fiber} are the volume, mass and surface area of the single fiber respectively, L is the overlapped portion of fiber electrodes. C could be obtained from CV test: $C = (1/2v) \times \oint IdU/\Delta U$, where v is the scan rate, I is the instantaneous current, ΔU is the voltage range. C could also be from GCD test: $C = t \times I/(\Delta U - U_{drop})$, where t is the discharge time, I is the discharge current, ΔU is the potential window, U_{drop} is the voltage drop in the discharge curve.

For the solid-state FSC, the volumetric capacitance ($C_{V-device}$) of the device was derived from the equation: $C_{V-device} = C/V_{device}$, where V_{device} is the volume of two fiber electrodes. The volumetric energy density (E_V) and power density (P_V) of the FSC can be obtained from $E_V = C_{V-device} \times U^2/7200$, $P_V = E_V \times 3600/t$.

2.3. Results and Discussion

Surprisingly, the rGO-Fs developed from the two-distinct wet-spinning recipes are dramatically different in their microscopic structure, morphology, electrical and mechanical properties. Consequently, they offer great discrepancy in capacitive performance when being assembled into a solid-state FSC. The continuous fibers were fabricated from a home-made apparatus as illustrated in Figure 2.2a. The details of the characterizations and analysis are presented in the following sections.

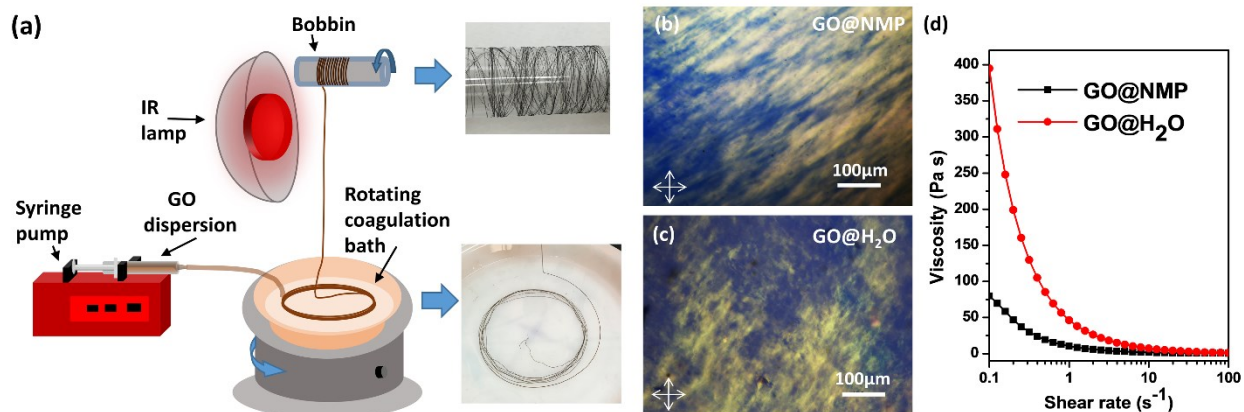


Figure 2.2 (a) A schematic of our benchtop wet-spinning setup for GO-fiber fabrication; (b) a POM image of 20 mg ml^{-1} dispersions of GO@NMP; (c) a POM image of 20 mg ml^{-1} dispersions of GO@H₂O; (d) rheological characterization of the two GO dispersions: dependence of the dispersion viscosity on shear rate.

NMP and DMF have both been reported as polar organic solvents capable of dispersing GO.^{16,121} However, GO-sheet size and the level of oxidation will also influence its dispersibility.¹³⁰ The average lateral size of GO sheets used for our wet spinning was estimated to be *ca.* $16 \mu\text{m}$ (Figure 2.3). To characterize the level of oxidation in our GO samples, a Fourier Transform Infrared (FTIR) spectrum of GO (Figure 2.4) shows prominent peaks around 1035 cm^{-1} ($\nu_{\text{C-O}}$), 1225 cm^{-1} (ν_{phenolic}), 1362 cm^{-1} ($\nu_{\text{O-H bending in tertiary alcohol}}$), 1622 cm^{-1} ($\nu_{\text{HOH bending in water}}$), 1730 cm^{-1} ($\nu_{\text{C=O}}$) and a broad peak at $2430\text{-}3722 \text{ cm}^{-1}$ ($\nu_{\text{O-H stretching}}$),¹³¹⁻¹³² confirming the chemical structure and the level of oxidation in our GO samples. Thus, good dispersibility of GO was observed in our experiments. As shown in Figure 2.5, at concentration of 20 mg ml^{-1} (the concentration used in our wet-spinning experiments), GO formed stable dispersions in both H₂O and NMP for seven days, but many GO flakes precipitated in DMF after one day. Therefore, in this study, we adopted water and NMP as the dope solvents for wet spinning. The solvents with different chemical structures will have different interactions with GO sheets, influencing the rheological properties

of GO dispersions. According to “Hansen solubility parameters”,¹³³ the ability of these solvents to form hydrogen bonds (hydrogen bonding cohesion parameter, δ_H) is different. Water shows higher hydrogen bonding capability ($\delta_H = 42.3$), while δ_H of NMP is merely 7.2. In addition, NMP as an aprotic solvent cannot form hydrogen bonds with itself since it’s not a hydrogen-bonding donor. As a result, the hydrogen-bonding effect in the GO-NMP (GO@NMP) system is less dominating, leading to distinct rheological behaviors of the dispersion and the unique properties of the resulted wet-spun fibers.

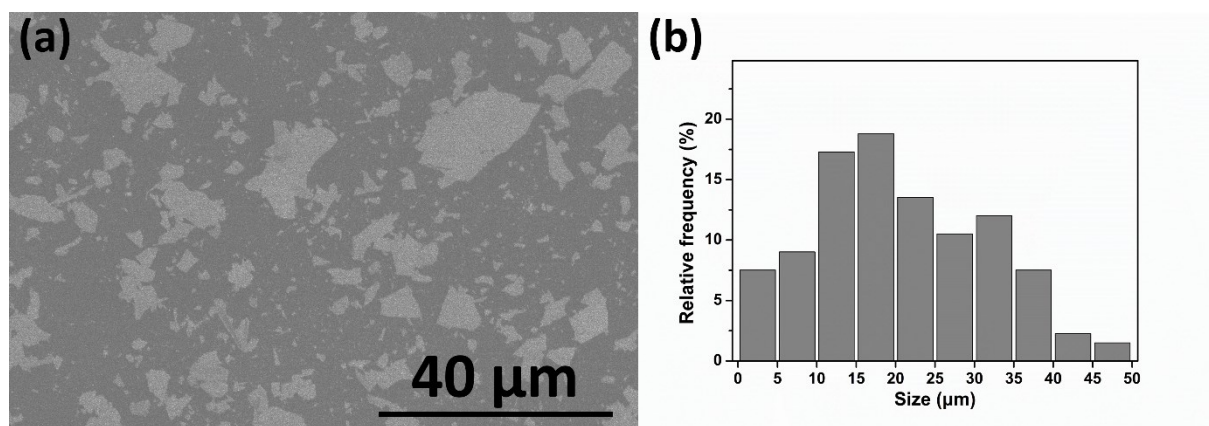


Figure 2.3 Size distribution of Graphene Oxide (GO) sheets. (a) an SEM image of GO sheets drop-casted onto a silica wafer; (b) the corresponding size distribution of the GO sheets. The average size of GO sheets is calculated to be ca.16 μm.

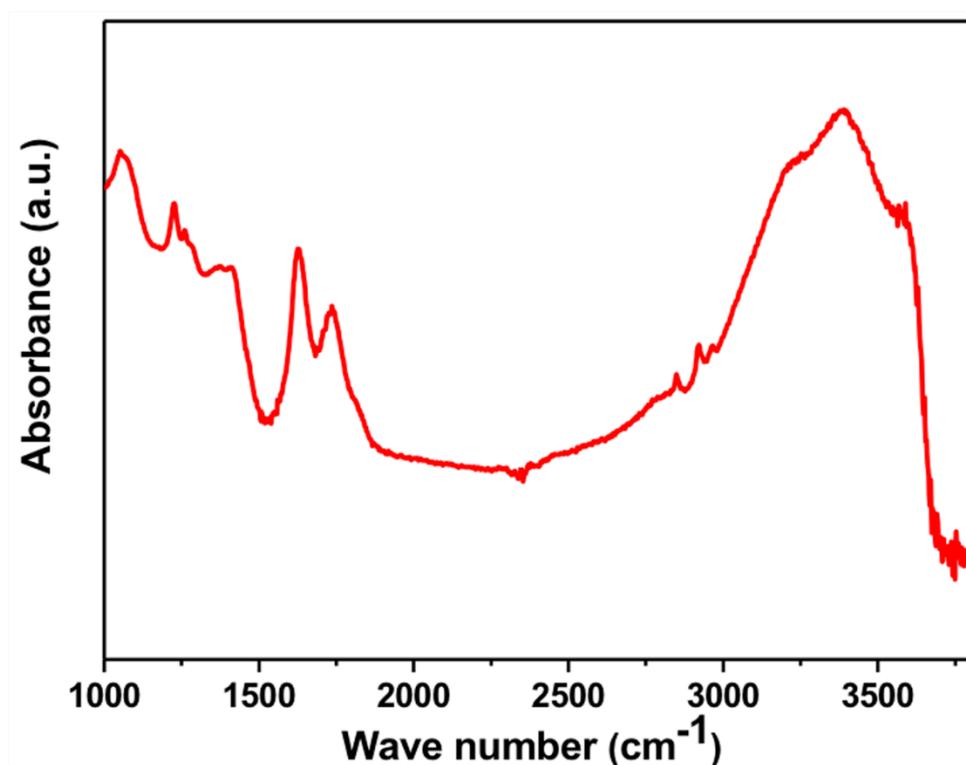


Figure 2.4 An FTIR spectrum of GO powders used in our experiments. Spectrum was measured in Attenuated Total Reflectance (ATR) mode using Ge crystal-plate under nitrogen (N₂) purging.

Figure 2.2b&c show the polarized optical microscope (POM) images of 20 mg ml⁻¹ GO dispersion in NMP and water, respectively. Both of them showed vivid colors, indicating the formation of LC phase.² Rheological behaviors of the spinning dope strongly affect its spinnability, which depends on the size of GO sheets, the concentration of the GO dispersion, and the GO-solvent interactions. Figure 2.2d shows the rheological behavior of GO dispersions in NMP and water at the same concentration (20 mg ml⁻¹). The flow curve of LC GO dispersion is similar to that of plastic fluids.¹³⁴ The relationship between viscosity (η) and shear rate ($\dot{\gamma}$) of GO@NMP and GO@H₂O were $\eta \sim (\dot{\gamma})^{-0.873}$ and $\eta \sim (\dot{\gamma})^{-0.941}$ respectively. The theoretical exponent for plastic materials is -1 and viscous character shows a value between 0 and -1. Therefore, in both NMP and H₂O systems, the slight deviation from -1 represents the existence of viscous component and confirmation of dominant plastic behavior.⁴⁰ This feature enables the shear-induced alignment of

the LC GO dispersion during spinning. Thus, the large size of GO sheets and high concentration used in both NMP and H₂O systems ensure their good spinnability.

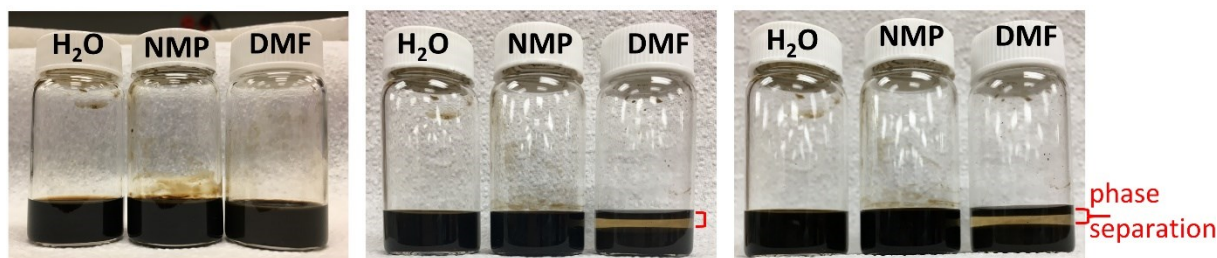


Figure 2.5 Digital pictures of GO dispersions in H₂O, NMP and DMF after being mechanically stirred for 48 h. Left: immediately after stirring stopped; Middle: one day after stirring stopped; Right: seven days after stirring stopped. GO formed stable dispersions in both H₂O and NMP for seven days, but many GO flakes precipitated in DMF after one day.

rGO-Fs were made by wet spinning of a LC GO dispersion into a coagulation bath followed by chemical reduction with HI. Apart from solvent, coagulation bath is another vital parameter in wet spinning and will influence fiber morphology and structure greatly, since the molecular structure and the diffusion rate of the coagulant matter significantly.¹³⁵ Until now, the coagulants used for GO dispersions can be divided into three categories, non-solvent precipitation, dispersion destabilization (*via* base or salt solutions, such as NaOH *etc.*), and cross-linking via divalent cations (such as CaCl₂) or amphiphilic or oppositely charged polymers (such as chitosan).⁴⁰ Among these, cross-linking agents and dispersion destabilization will introduce impurities and have negative side effects on the electrochemical performance of rGO-Fs.¹¹⁹ Thus, non-solvents of GO (*e.g.* acetone, acetic acid, and ethyl acetate *etc.*)^{118-119, 127} are expected to be the proper coagulants for supercapacitor applications. In addition, solvent and coagulation bath should match each other to ensure successful coagulation. For example, ethyl acetate is a good coagulant for GO@NMP but cannot be used for GO@H₂O dispersions, because water and ethyl

acetate are immiscible, which hinders the dual diffusion process. When acetic acid was used as the coagulation bath for GO@NMP, GO fibers were floating in the bath requiring longer coagulation time and resulting in lower fiber strength. This made the fiber collection difficult and inhibited further processing. However, acetic acid works well when using GO@H₂O as the spinning dope, and stronger fibers are usually obtained. Acetone-coagulated fibers with inner porous structures are much weaker mechanically than those coagulated from other non-solvents in both water and NMP systems. Therefore, we chose non-solvent ethyl acetate and acetic acid as the proper coagulation baths for GO@NMP and GO@H₂O systems, respectively, in order to ensure efficient fiber processing and to obtain desired rGO-Fs in both systems. The solvent together with the non-solvent coagulant will result in distinct rGO-F morphologies which will be discussed later. In addition, we kept all the other wet-spinning parameters (*i.e.* spinneret, draw ratio 1.5, drying *etc.*) and GO reduction processes the same, for the purpose of direct comparison between these two systems.

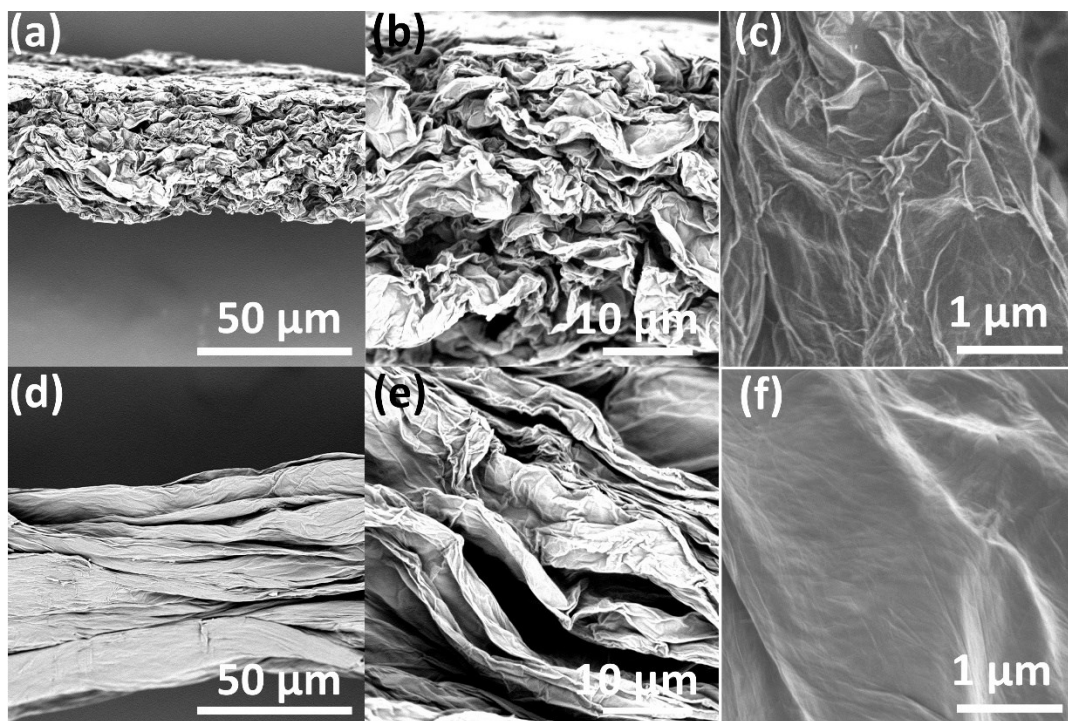


Figure 2.6 SEM images of rGO@NMP-F (a, b, c) and rGO@H₂O-F (d, e, f).

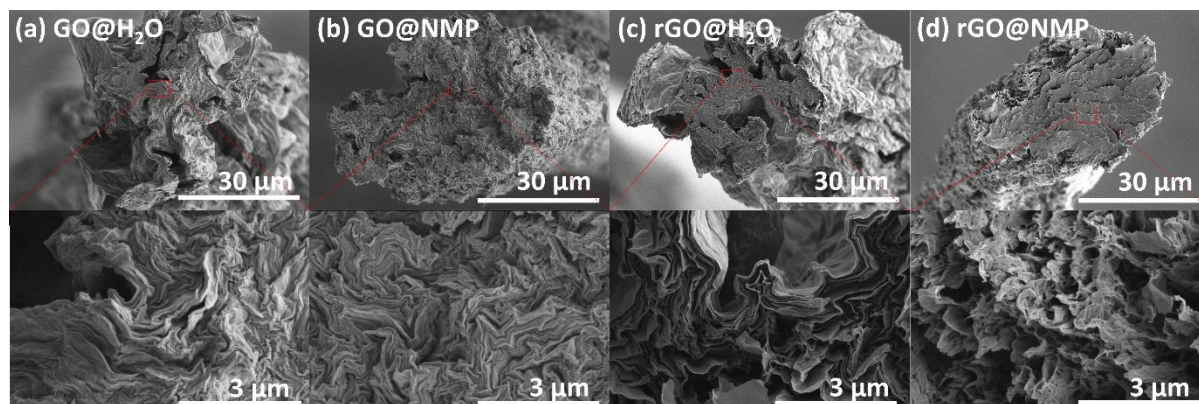


Figure 2.7 SEM images of fiber cross-sections of (a) GO@H₂O-F; (b) GO@NMP-F; (c) rGO@H₂O-F; (d) rGO@NMP-F.

The surface and cross-sectional morphologies of GO-Fs/rGO-Fs are revealed by SEM (Figure 2.6 and Figure 2.7). The diameters (the largest width of cross-section) of rGO@NMP-F

and rGO@H₂O-F are ~40 μm and ~45 μm respectively. The rGO@NMP-Fs are obviously rougher and more wrinkled with porous structure on the surface (Figure 2.6b & c). In comparison, the surface of rGO@H₂O-Fs was rather smooth with few grooves. As shown in Figure 2.7, GO@H₂O-Fs present irregular multi-armed structure (Figure 2.7a), whereas higher circularity was observed in the cross-sections of GO@NMP-Fs (Figure 2.7b). In addition, GO sheets in both GO-Fs are compactly packed and well aligned along the longitudinal direction, but are with more microscale wrinkles in GO@NMP-Fs. After chemical reduction, the highly aligned structure is well maintained in both rGO-Fs, and microvoids are generated between graphene sheets (Figure 2.7c & d), resulting in higher porosity. The much more wrinkled rGO sheets in rGO@NMP-Fs exhibit more disturbed stacking throughout the transverse section. Methylene blue (MB) adsorption SSA measurement showed that the rGO@NMP-F with SSA of 803 m² g⁻¹ was almost twice than that of rGO@H₂O-F (445 m² g⁻¹). Obviously, the rough and wrinkled morphology of rGO@NMP-Fs favors the diffusion and adsorption of ions in gel-state electrolyte, thus improving the electrochemical performance of the corresponding FSCs.

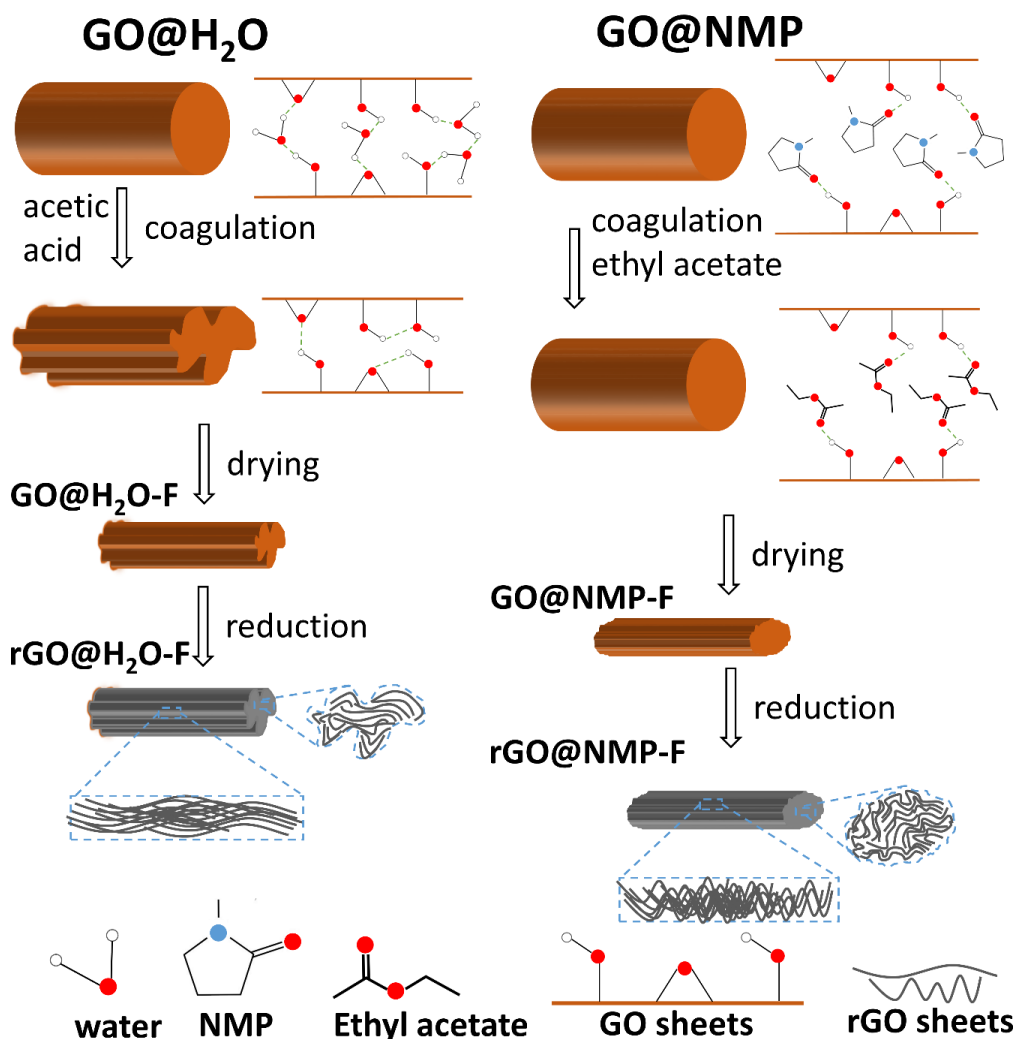


Figure 2.8 A proposed mechanism for the formation of rGO@H₂O-F and rGO@NMP-F. Comparing to water, NMP molecules carry fewer hydrogen bonding sites and cannot form hydrogen bonding with themselves. In the coagulation process, ethyl acetate diffuses into GO sheets, the larger size of ethyl acetate and weaker hydrogen bonding between GO and ethyl acetate lead to larger distance between GO sheets. After the evaporation of ethyl acetate, the larger inter-sheet distance would shrink more, and result in rougher and more wrinkled morphology in both longitudinal and transverse directions. In addition, rGO@H₂O-Fs present irregular multi-armed structure with less wrinkles, while the contour of rGO@NMP-Fs is more regular but with much more microscale wrinkles on sheet surfaces.

Usually in a solvent-nonsolvent coagulation system, to enable the wet-spinning process, the imbibition rate (see supplementary for details) of coagulant should be higher compared to the solvent, *i.e.* the ratio should be higher than 1.¹¹⁹ The imbibition rate of a liquid is in proportion to $k(\sigma/\mu)^{1/2}$, where k is a constant, σ is the surface tension of the spreading liquid and μ is the viscosity of the spreading liquid.¹¹⁹ The imbibition rate ratio of ethyl acetate/NMP is 1.44, ensuring the successful coagulation. However, in acetic acid/water combination, this ratio is 0.54, highlighting the acidity of the coagulant apart from its non-solvent nature. For GO@H₂O, once the GO@H₂O spinning jet gets in contact with acetic acid, the hygroscopic property of acetic acid promotes the dehydration and the formation of hydrogen bonds between the GO sheets, inducing an immediate precipitation of GO at the interface. The larger volumes of acetic acid molecules will retard their diffusion into the spinning dope, resulting in a lower coagulation rate and a higher difference in mass-transfer rate.¹³⁵ These factors together facilitate the formation of the irregular multi-armed fiber structure. As for GO@NMP, the exchange of NMP and ethyl acetate is more balanced around the contour of the spinning jet, due to the weaker interaction between GO sheets and NMP/ethyl acetate, as well as smaller difference in molecular sizes between the dope solvent and the coagulant, resulting in more regular cross-section structure. On the other hand, the much rougher and more wrinkled morphology of rGO@NMP-Fs may be subject to larger molecular size of ethyl acetate and weaker hydrogen bonding between GO sheets and ethyl acetate, which leads to larger distance between GO sheets. When the trapped coagulant molecules evaporate during the drying process, the fiber with larger sheets distance would shrink and result in a rough surface, inducing GO-sheet stacking with more wrinkles in both longitudinal and transverse directions and being well maintained after reduction, as illustrated in Figure 2.8.

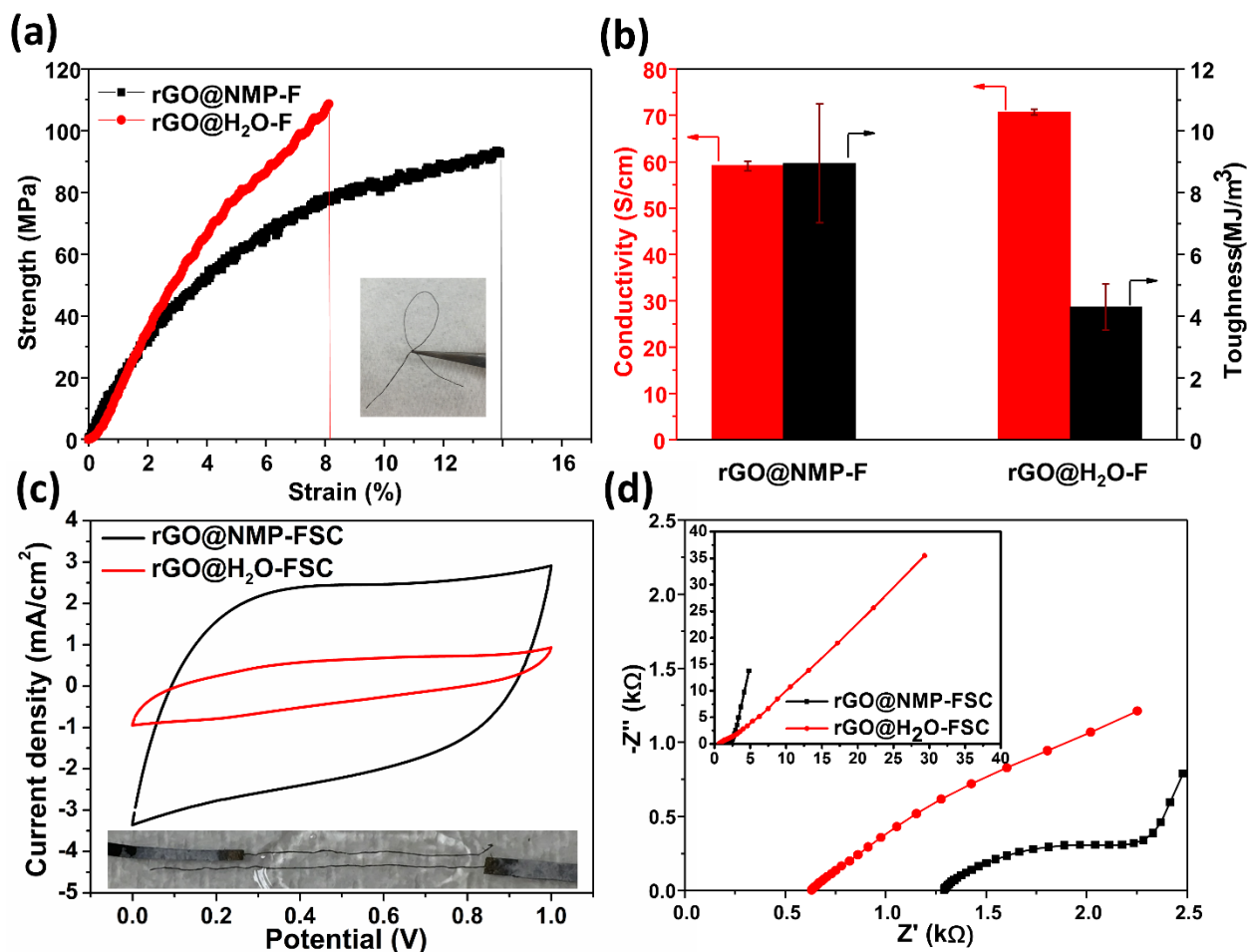


Figure 2.9 (a) Typical strength-strain curves of rGO-F. The inset shows a highly flexible rGO-F. (b) conductivity and toughness of rGO-F. (c) CV curves at scan rate 40 mV s^{-1} . Inset is a photo of a FSC assembled from two parallel single fibers (scale bar, 2mm). (d) Nyquist plots from the EIS tests of rGO@NMP-FSC and rGO@H₂O-FSC.

Both rGO@NMP-F and rGO@H₂O-F have rGO sheets highly aligned along the longitudinal direction and well packed with micro-scale delamination along the transverse direction, leading to reasonable mechanical strength and electrical conductivity. Figure 2.9a shows the typical stress-strain curves of rGO@NMP-F and rGO@H₂O-F respectively. The tensile strength of rGO@H₂O-F (107 MPa) is slightly higher than that of rGO@NMP-F (93 MPa). It is comparable to the reported values of chemically reduced rGO fibers. For example, the coaxial rGO sodium

carboxymethyl cellulose (CMC) composite fiber has a tensile strength of 73-116 MPa¹³⁶ and rGO-F coagulated by NaOH/methanol solution shows a tensile strength of 140 MPa². Notably, in terms of breakage elongation, rGO@NMP-F (~14%) is almost twice of that of rGO@H₂O-F (~7.8%), and much higher than that of the reported rGO fiber spun from GO water dispersion (~6.6%) with comparable tensile strength of ~104 MPa,^{2, 118} indicating good flexibility and higher toughness (Figure 2.9b) against fracture under tensile stress. This robustness is suitable for the applications in woven or knitting fabrics.¹³⁶ The higher elongation is mainly attributed to the wrinkled structure of rGO sheets existing in the rGO@NMP-F along fiber axis. This also suggests that the tensile strength of rGO-Fs could further be improved by optimizing spinning process. The electrical conductivities were calculated to be ~60 and 71 S cm⁻¹ for rGO@NMP-F and rGO@H₂O-F respectively (Figure 2.9b), which was comparable to that of rGO-Fs reported in literatures.¹³⁶⁻¹³⁷ The lower conductivity of rGO@NMP-F may be ascribed to the lower level of alignment of rGO sheets along the fiber axis and fewer edge-to-edge contacts in between.

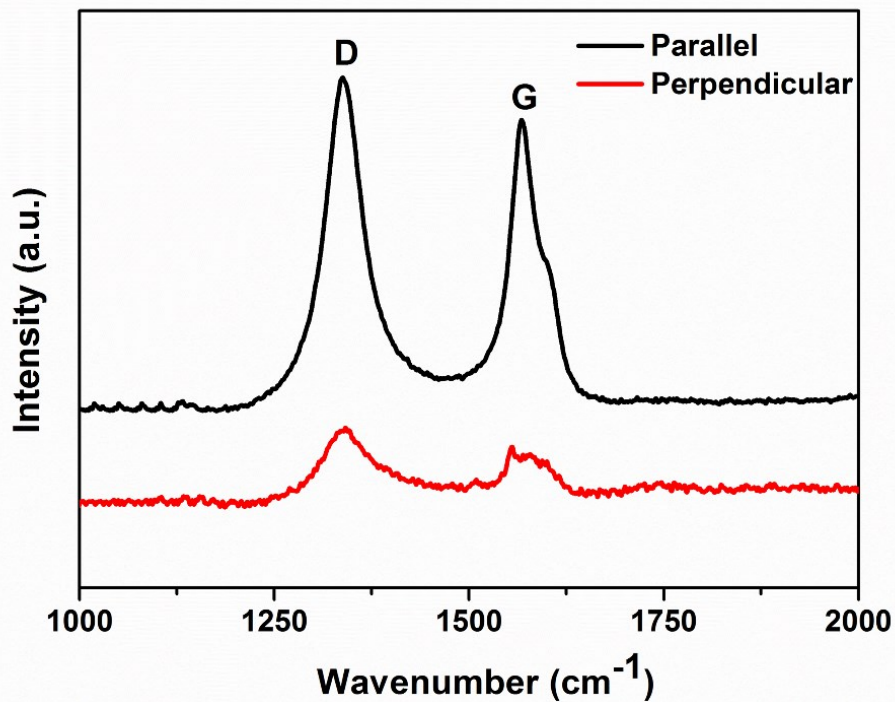


Figure 2.10 Polarized Raman spectra of an rGO@NMP-F with the incident laser beam parallel and perpendicular to the fiber axis, respectively. The Raman ratio, which is determined from the ratio between the G peak intensities of the two spectra (parallel vs. perpendicular), provides a useful probe for the relative degree of alignment.

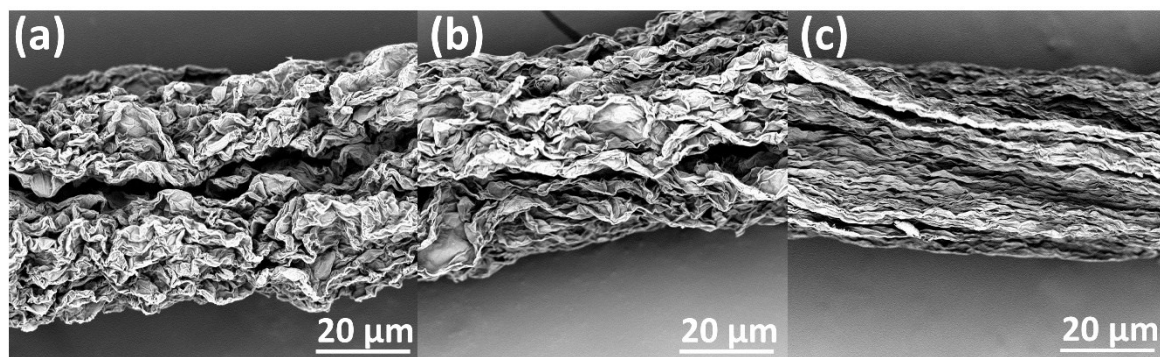


Figure 2.11 SEM images of rGO@NMP-Fs with draw ratio of (a) 1.5, (b) 1.75 and (c) 2 respectively.

Table 2.1 Mechanical and electrical properties of rGO@NMP-Fs as a function of draw ratio applied in the wet-spinning processes

Draw ratio	Orientation degree (I_{\parallel}/I_{\perp})	Linear density/ dtex	Tensile strength/ MPa	Elongation /%	Modulus/ GPa	Electrical conductivity/ S cm ⁻¹
1.5	3.75	3.33	93.4±6	14.1±0.8	2.4±0.2	59.2±1.1
1.75	4.21	2.92	121.8±5	11.8±0.5	6.1±0.3	75.2±1.5
2	4.78	1.52	163.4±6	10.2±1	10.7±0.5	86.3±0.7

In this context, we also studied the mechanical properties and electrical conductivity of rGO@NMP-Fs as a function of rGO-sheet orientation obtained at different draw ratios (from 1.5 to 2), by controlling the rotation speed of the coagulation bath. Polarized Raman spectroscopy has been used to probe the degree of rGO-sheet alignment from the ratio of G-band intensities between the parallel and perpendicular directions.⁷⁴ Figure 2.10 shows polarized Raman spectra of rGO@NMP-F (draw ratio at 1.5) along the parallel direction and perpendicular directions, respectively. As shown in Table S1, the relative degree of orientation increased monotonically along with the increment in the draw ratio. Correspondingly, in SEM images (Figure 2.11), the fiber with higher draw ratio has smaller diameter and less wrinkled structure. Consequently, the tensile strength, modulus and conductivity of rGO@NMP-Fs exhibited monotonic change along with the degree of orientation, with highest values of ~163 MPa, ~10.7 GPa and ~86 S cm⁻¹, respectively, at the highest draw ratio of 2. These results indicate the impact of rGO-sheet orientation on the fiber properties.

The structures and properties of the wet-spun fibers largely depend on the wet-spinning parameters. The fiber morphology and electrical conductivity have great influence on the electrochemical performance of the fiber electrodes in energy-storage devices. The

electrochemical performance of the FSCs was tested in a two-electrode system in a parallel configuration (Figure 2.9c inset). Two rGO-Fs were fixed in parallel with an effective length of 1.5 cm on a glass slide, and the distance in between them is *ca.* 1 mm. PVA/H₂SO₄ was used as both the gel electrolyte and the separator.

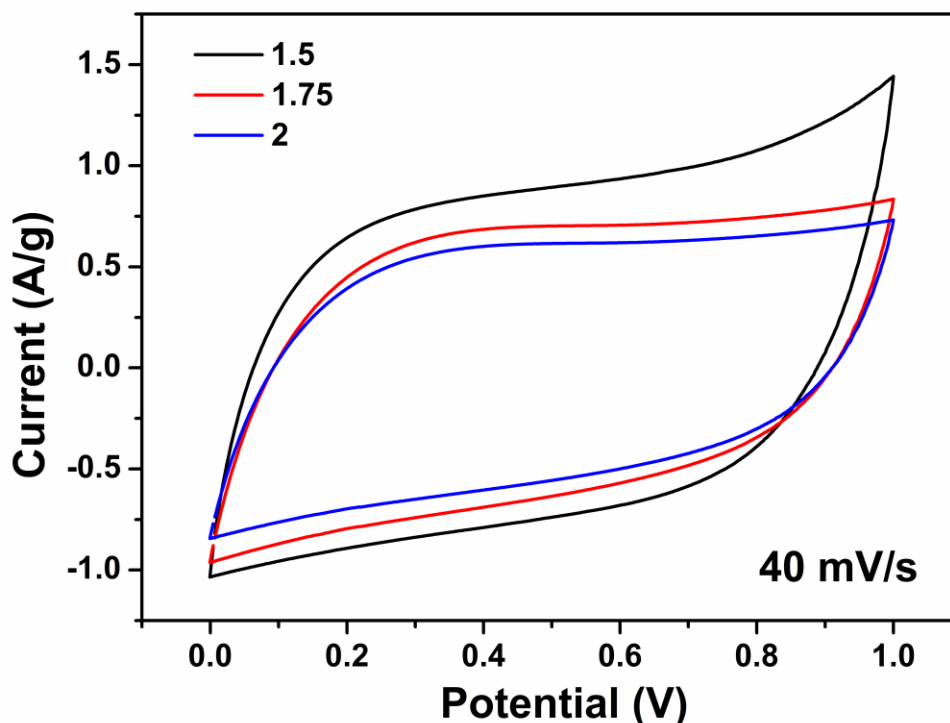


Figure 2.12 Cyclic voltammetry (CV) curves of rGO@NMP-FSCs with rGO@NMP-Fs at different draw ratios (1.5, 1.75 and 2). Among these, rGO@NMP-F at draw ratio of 1.5 exhibited the highest specific capacitance.

Among all the rGO@NMP-Fs with different degrees of orientation, the fibers prepared at draw ratio of 1.5 demonstrated the highest specific capacitance (Figure 2.12), mainly due to the highest surface roughness maintained at the lowest draw ratio. The comparison of rGO@NMP-FSC and rGO@H₂O-FSC are shown in Figure 2.9 with both draw ratios of 1.5. The cyclic

voltammetry (CV) curves of both FSC (Figure 2.9c) are close to rectangular, indicating that the FSCs behave the same as typical carbon-based EDLCs. The area of rGO@NMP-FSC CV curve is obviously larger than that of rGO@H₂O-FSC, indicating that the rGO@NMP-FSC offers much higher capacitance, owing to the wrinkled surface structure and the larger electrolyte-ion accessible surface area. The calculated specific capacitance C_A and C_L of rGO@NMP-FSC reaches 98.6 mF cm⁻², 0.92 mF cm⁻¹ at 40 mV s⁻¹ (99.7 mF cm⁻² and 0.94 mF cm⁻¹ at current density of 2.83 mA cm⁻²), almost ~5 folds higher than that of rGO@H₂O-FSC (19 mF cm⁻², 0.24 mF cm⁻¹ at 40 mV s⁻¹), and also higher than the reported wet-spun rGO fiber FSC with rGO@H₂O-F coagulated in CaCl₂ solution (5.1 mF cm⁻² or 0.036 mF cm⁻¹ at 0.1 mA cm⁻²)¹³⁸ and non-LC spun rGO@H₂O-F coagulated in acetic acid (67.7 mF cm⁻² or 0.88 mF cm⁻¹ at 0.21 mA cm⁻²)¹¹⁸.

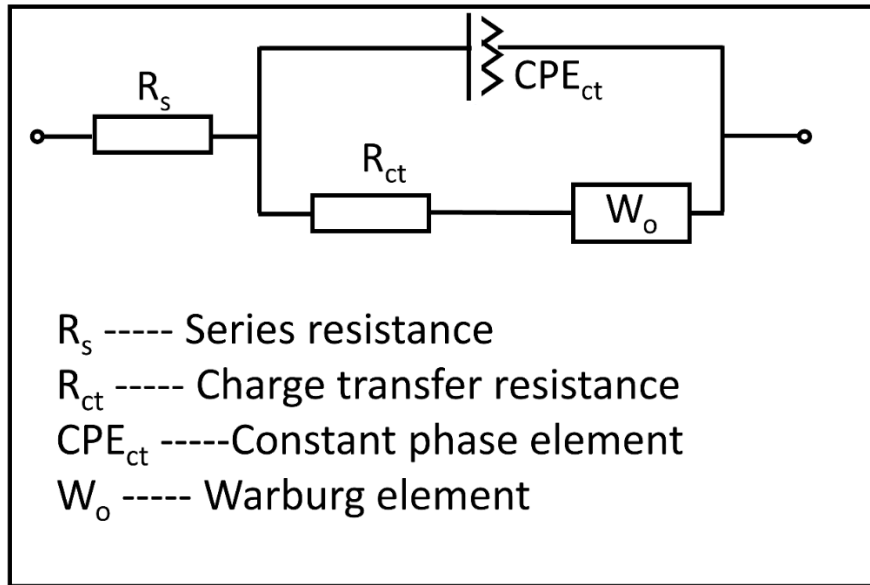


Figure 2.13 Equivalent circuit for fitting Nyquist plots in the high frequency region by Z-view.

Table 2.2 Z-view fitting results for Nyquist plots in Figure 2.9c and d with the equivalent circuit shown in Figure 2.12.

Fitting Parameters	R_s/Ω	R_{ct}/Ω	CPE _{ct}		W _o			CPE _{dl}	
			Y_0/mF	α	R_w/Ω	T_w/s	α	Y_0/F	α
NMP	1267	1210	0.097	0.51	1350	20.13	0.53	0	0.92
H ₂ O	624.2	4000	0.077	0.54	33791	299	0.99	0	0.65

Figure 2.9d shows the Nyquist plot from the electrochemical impedance spectroscopy (EIS) test with frequency from 0.01 Hz to 0.1 MHz with amplitude of 10 mV. For quantitative analysis, an equivalent circuit (Figure 2.13) was adopted to fit the Nyquist plots. From high frequency on the real axis, we can see the series resistance (R_s) of rGO@NMP-FSC and rGO@H₂O-FSC are *ca.* 1.26 k Ω and 0.62 k Ω respectively (Table 2.2). The series resistance includes electrode resistance, solution resistance and contact resistance in the FSC. Considering we used the same electrolyte and FSC structure, the R_s difference between these two FSC is originated from the electrodes and this is consistent with the conductivity results of these two kinds of fibers. Comparing to rGO@H₂O-FSC, there is an obvious semi-circle in rGO@NMP-FSC, which could be attributed to much more accessible rGO sheets of rGO@NMP-F and thus more exposed residual oxygen-containing groups. In addition, rGO@NMP-FSC showed obvious short 45° Warburg region, and a more vertical line at low frequency, suggesting much better EDLC performance.

Figure 2.14a shows the CV curves of rGO@NMP-FSC from 10 to 100 mV s⁻¹ scan rates. At low scan rate, it exhibits good quasi-rectangular shape. However, as scan rate increases, it turns to fusiform shape as observed in most FSCs, with the specific capacitance dropped. The highest C_V (Figure 2.14b) of rGO@NMP-FSC was 196.7 F cm⁻³ (147.5 mF cm⁻²) at scan rate of 10 mV s⁻¹, which is among the best values reported in the literature. The linear density of rGO@NMP-F

was 3.33 dtex (1 dtex = 1 g km⁻¹), and the mass capacitance (C_M) of rGO@NMP-FSC was 69.5 F g⁻¹. The C_V decayed to 48% of its initial capacitance at 100 mV s⁻¹. Similar as the situation reported in literatures, Zhao *et al.* reported that the specific volumetric capacitance decayed to 50% of its initial capacitance at 100 mV s⁻¹ in PVA/H₂SO₄ electrolyte.¹³⁹ This capacitance decay at high scan rate was most likely due to the insufficient ionic transport in the charge/discharge process.¹⁴⁰ The galvanostatic charge-discharge (GCD) curves at different current densities (Figure 2.14c) exhibits triangular shapes with a columbic efficiency of *ca.* 92%, suggesting good reversibility of the FSC and good charge propagation between the two fiber electrodes. Compared with other solid-state metal wires and/or carbonaceous-fiber based FSCs, the specific capacitance of rGO@NMP-FSCs (149.5 mF cm⁻², 199.4 F cm⁻³ at 0.35 mA cm⁻²) is higher than that of the CNT coated carbon FSC (86.8 mF cm⁻² at 0.38 mA cm⁻²),⁸² almost two times the value of the non-LC spun rGO-FSC (78.7 mF cm⁻² at current density of 0.085 mA cm⁻²),¹¹⁸ and much higher than mesoporous carbon/CNT composite FSC (39.7 mF cm⁻² at 0.08 mA cm⁻²),¹⁴¹ core-shell rGO FSC (1.7 mF cm⁻² at 0.02 mA cm⁻²),⁹⁶ and even FSCs with pseudocapacitive materials incorporated, such as rGO/polyaniline (PANi) composite FSC (66.6 mF cm⁻² at 0.1 mA cm⁻²),¹³⁸ CNT/poly(3,4-ethylenedioxythiophene) (PEDOT)/Pt wire composite FSC (179 F cm⁻³ at 10 mV s⁻¹),¹⁴² and MnO₂/CNT fiber composite FSC (69.3 mF cm⁻³ at 0.1 A cm⁻³)⁹⁷. The detailed comparison has been listed in Table 2.3 in the supporting information.

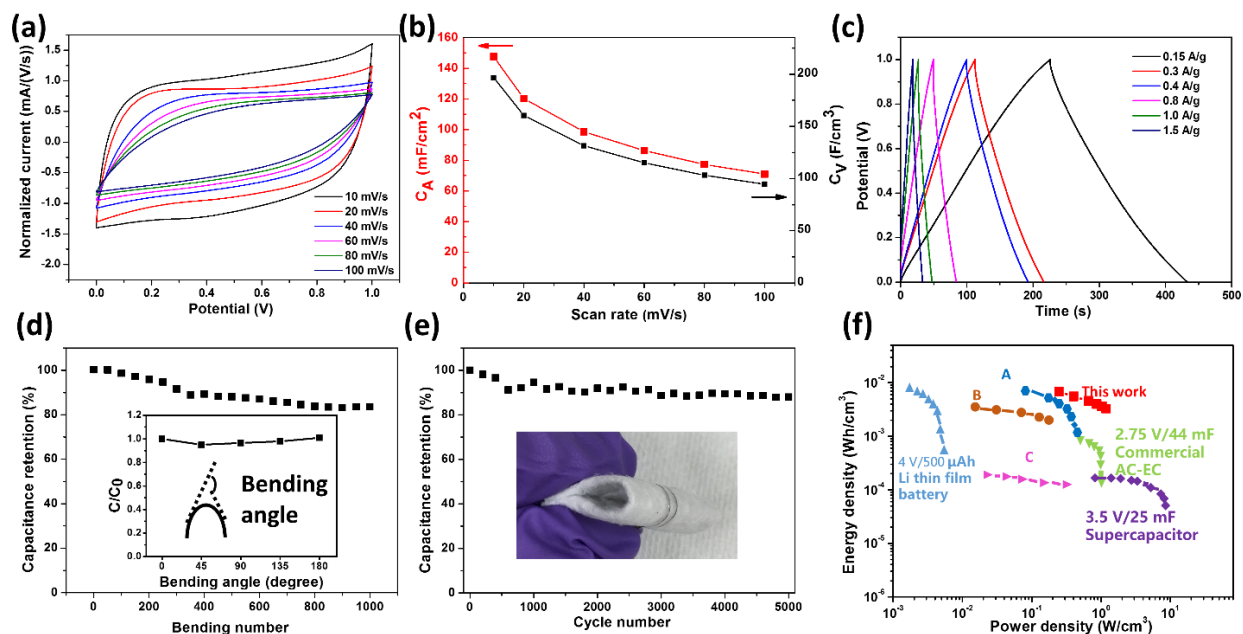


Figure 2.14 Electrochemical performance of rGO@NMP-FSC. (a) CV curves at different voltage scan rates. The current is normalized by the scan rates. (b) C_A and C_V at different scan rates; (c) GCD curves at different current density; (d) Capacitance retention as a function of bending cycles. The inset is capacitance stability during bending from 0° to 180° . The inset photo in (e) shows the 180° bending state. (e) cycling stability for 5000 cycles. (f) Ragone plot of different FSCs and some commercial devices. Commercially available 4 V/500 μ Ah Li thin-film battery,¹⁴³ 2.75 V/44mF commercial AC-EC,⁷ 3.5 V/25 mF SC¹⁴⁰ and some published experimental data (A) a non-LC spinning pure rGO FSC,¹¹⁸ (B) a CNT/rGO@CMC hybrid FSC¹³⁶ and (C) a MnO₂ incorporated carbon fiber SC¹⁴⁴.

In order to measure the flexibility of FSC, we used a nonwoven fabric to replace the glass slide (Figure 2.14e inset). Figure 2.14d inset shows a capacitance retention of rGO@NMP-FSC under different bending angles from 0° to 180° . The capacitance retention was tested by CV at 20 mV s^{-1} and it exhibited less than 5% fluctuation during the bending. In addition, it also retained 90% after 1000 bending cycles (Figure 2.14d), demonstrating excellent flexibility and bending

stability of the rGO@NMP-FSC device. A capacitance retention rate of 88% was observed after 5000 charge-discharge cycles (Figure 2.14e) at 1 A g^{-1} . The small capacitance loss may be attributed to the evaporation of water in the gel electrolyte.

The Ragone plot of rGO@NMP-FSC derived from the CV curves is presented in Figure 2.14f at various power densities. The volumetric energy density and power density of the FSCs are more meaningful parameters for evaluating the energy-storage performance of the device. It can be seen that the E_V and P_V of our rGO@NMP-FSC are at the upper corner of the Ragone plot. The maximum E_V of the rGO@NMP-FSC is 6.8 mWh cm^{-3} (at a power density of 120.4 mW cm^{-3}), which is approximately sevenfold higher than that of $2.75 \text{ V}/44 \text{ mF}$ commercial AC-EC⁷ and 30-fold higher than that of $3.5 \text{ V}/25 \text{ mF SC}$,¹⁴⁰ and is even comparable to that of $4 \text{ V}/500 \mu\text{Ah}$ Li thin-film battery ($0.3\text{-}10 \text{ mWh cm}^{-3}$)¹⁴³. This E_V is among the highest values of recently reported FSCs. The power densities ($120.4\text{-}1183 \text{ mW cm}^{-3}$) are also among the best value compared with the other reported data.

Table 2.3 Comparison of specific capacitance (based on a single electrode) and energy density (based on device) of solid-state FSC.

Electrode material	Electrolyte	C_A (mF cm ⁻²)	C_V (F cm ⁻³)	C_M (F g ⁻¹)	C_L (mF cm ⁻¹)	E_A (μWh cm ⁻²)	E_V (mWh cm ⁻³)
rGO@NM P-F This work	H ₂ SO ₄ -PVA	149.5 @0.15A g ⁻¹ , 0.35 mA cm ⁻²	199.4	69.5 @10 mV s ⁻¹	1.4	5.12	6.8
NLC-spun rGO fiber ¹¹⁸	H ₂ SO ₄ -PVA	78.7 @0.2 A g ⁻¹ , 0.085 mA cm ⁻²	226 @0.2 A g ⁻¹ , 0.085 mA cm ⁻²	185 @0.2 A g ⁻¹ ,	/	/	7.26
rGO+CNT @CMC fiber ¹³⁶	H ₃ PO ₄ -PVA	177 @0.1 mA cm ⁻²	158 @0.1 mA cm ⁻²	/	/	/	3.5
rGO+PANi fiber ¹³⁸	H ₃ PO ₄ -PVA	66.6 @0.1 mA cm ⁻²	76.1 @0.1 mA cm ⁻²	/	0.7 @0.1 mA cm ⁻²	/	/
CNT coated carbon fiber ⁸²	H ₃ PO ₄ -PVA	86.8 @0.38 mA cm ⁻²	14.1 @5 mV s ⁻¹	11.1 @5 mV s ⁻¹	/	/	0.14
N-doped rGO+CNT fiber ¹⁰⁶	H ₃ PO ₄ -PVA	/	~200 @0.267 A cm ⁻³	/	/	/	~6.3
Mesoporous carbon+CNT composite fiber ¹⁴¹	H ₃ PO ₄ -PVA	39.7 @0.08 mA cm ⁻²	/	/	150 @0.125 A g ⁻¹	/	/
PEDOT+CNT fiber+Pt wire ¹⁴²	H ₃ PO ₄ -PVA	73@10 mV s ⁻¹	179 @10 mV s ⁻¹	/	0.46@10 mV s ⁻¹	/	1.4
MnO ₂ +PPy @CNT fiber ⁹⁷	H ₃ PO ₄ -PVA	/	69.3 @0.1 A cm ⁻³	/	/	/	/
Core-shell rGO fiber ⁹⁶	H ₃ PO ₄ -PVA	1.7 @0.02 mA cm ⁻²	/	38 @0.2 A g ⁻¹	/	/	/

2.4. Conclusion

In summary, we fabricated continuous wet-spun rGO-Fs with large surface area and high toughness from the combination of NMP/ethyl acetate as the dope-solvent/coagulant pair, which is favored over the H₂O/glacial acetic acid pair for solid-state FSC applications. These fibers possessed wrinkled morphology and porous structure which could facilitate the adsorption and diffusion of electrolyte ions. The specific capacitance of rGO@NMP-FSC was up to 196.7 F cm⁻³ (147.5 mF cm⁻²), almost five times higher than that of rGO@H₂O-FSC and higher than existing pure or hybrid rGO-Fs and CNT fibers. The energy density of this rGO@NMP-FSC was 6.8 mWh cm⁻³, which was comparable to that of 4 V/500 μAh Li thin-film battery. The power density was 1183 mW cm⁻³, among the highest values of recently reported FSCs. This approach opens a new avenue to design and fabricate conductive, mechanical strong and high surface area rGO-Fs and its application in FSCs and paves the way for the production of low cost, flexible, biosafe and high electrochemical performance wearable electronic energy storage devices.

Chapter 3 Mordant Inspired Wet-Spinning of Graphene Fibers for High Performance Flexible Supercapacitors

3.1. Introduction

Graphene, due to its extraordinary molecular-level properties, such as large surface area, excellent mechanical strength, good optical transparency, and high thermal and electrical conductivities,¹⁴⁵⁻¹⁴⁷ has been extensively studied as electrode materials for electrochemical double-layer capacitors (EDLCs).¹⁴⁸⁻¹⁴⁹ Various macroscopic structures, including one-dimensional (1D) fibers,¹⁵⁰ two-dimensional (2D) films¹⁵¹ and three-dimensional (3D) frameworks have been assembled.¹⁵² Among these architectures, fiber-shaped supercapacitors (FSCs) have attracted enormous attention, mainly due to their high flexibility which enables them to be manually woven or knitted into fabrics with excellent wearability/breathability, working as energy-storage yarns or fabrics in smart textiles.^{9, 153-156} More importantly, fiber-shaped energy-storage devices can become attractive power sources for miniaturized electronic devices such as microrobots, physiological sensors, and even implantable medical devices, since they can have small volumes and could be easily integrated into all kinds of shaped structures.^{5, 157-158}

Solution-processing of graphene oxide (GO) followed by chemical or thermal reduction is a well-established protocol to synthesize large quantities of graphene-like structures.¹⁵⁹ Owing to the abundant oxygen-containing groups (OCGs) on the basal planes and edges, GO can be well dispersed in water. The excellent dispersibility together with its large aspect ratio renders the formation of lyotropic lamellar liquid crystals (LCs) of GO sheets in water with orientational orders, enabling their wet spinning into continuous GO fibers,² and subsequent reduced GO (rGO) fibers *via* either chemical or thermal treatments.

Coagulation bath in wet-spinning process is one of the most important factors that influences the structures and properties of the as-spun fibers.¹¹⁷ So far, alkaline baths (such as KOH and NaOH), divalent cations (CaCl₂ and CuSO₄), positive charged polymer and small molecules (chitosan, CTAB, and diamine), and non-solvents (acetone and glacier acetic acid)^{9, 119, 125, 137, 160} have all been used as coagulants. Among those, insulating polymers or macromolecules will improve the mechanical properties of the resulted fibers but would inevitably compromise the electrical conductivity. In contrast, small metal cations (*e.g.* Ca²⁺) can diffuse into the as-spun fibers in wet state, crosslink GO sheets in-situ, and result in improved mechanical strength and unaffected electrical conductivity of final rGO fibers. However, these Ca²⁺ cross-linked fibers are typically made of dense packing of GO/rGO flakes, which is unfavorable for capacitive energy storage. On the other hand, Abouralebi *et al.*¹¹⁹ found that rGO fibers from acetone coagulant generated more porous structure with higher specific surface area (SSA), offering higher capacitance over that of the fibers from Ca²⁺ bath. However, the mechanical and electrical properties of acetone-based rGO fibers were almost one order of magnitude lower than that of the Ca²⁺-coagulated fibers, mainly due to weak interactions among rGO sheets. Therefore, a trade-off between SSA and mechanical strength/electrical conductivity has to be made for these rGO fibers as supercapacitor electrodes. Hitherto we are still waiting for rGO fibers that can offer excellent energy-storage capability while being compatible with machine weaving and/or knitting.

Historically, mordants (alum/tannin, or aluminium acetate) are widely used in dyeing industry to improve color efficiency and wash fastness of natural dyes such as Alizarin and Saffron. A mordant is basically a chemical binding reagent that helps the adhesion between polymeric fibers (cotton, silk, and wool) and dye molecules. Traditional mordants used include alum (AlK(SO₄)₂·12 H₂O), cuprous sulfate (CuSO₄·5 H₂O), ferrous sulfate (FeSO₄), and aluminum

acetate ($\text{Al}(\text{OOCCH}_3)_3$), all of which are environmentally friendly and cost-effective.¹⁶¹ To our knowledge, the binding effect of mordants mainly comes from the interactions existing between the multivalent cations and the local chemical moieties in the dye/polymer molecules. Also, according to the classic Schulze-Hardy rule,¹⁶²⁻¹⁶³ the higher valence the cations have, the stronger charge screening the cations can provide. Therefore, trivalent cations (Al^{3+} and Fe^{3+}) are the most widely used inorganic coagulants in wastewater treatment.¹⁶⁴ With regard to GO, trivalent cations, such as Al^{3+} , have been reported to be an effective cation for stabilizing GO membranes in water.^{165, 166} In aqueous dispersions, cations with different charges and electronegativity have different adsorption affinity with GO, leading to transformation and aggregation of GO sheets into various sphere-like flocculation, as reported by Yang *et al.*¹⁶⁷ In addition, trivalent cations have been reported as better cross-linkers for alginate gel than divalent cations for mechanical performance.¹⁶⁸

GO sheets typically carry various OCGs on their basal planes and the edges, resulting in small sp^2 -C domains isolated within the sp^3 -C matrix.¹⁶⁹ These functional moieties could offer different interactions with the intercalated ions in between GO sheets, leading to the deformation or corrugation of the GO sheets and thus distinct fiber morphologies.¹⁶⁷ All these interactions are strongly depending on the intrinsic physiochemical properties of the cation, such as its electron configuration, size, valence number *etc.* So far, to our knowledge, no report has used trivalent cations as a coagulant for wet spinning of GO/rGO fibers. Inspired by the prominent differences brought by the application of trivalent cations in GO membranes, GO dispersions and alginate gels, we have applied trivalent cations in the coagulating process of GO to target enhanced fiber mechanical and morphological features, which are of the primary demands for fiber electrodes in FSC applications.

In our experiment, two types of trivalent metal cations, Al^{3+} and Fe^{3+} , were used as coagulants for rGO fibers (rGOF- Al^{3+} and rGOF- Fe^{3+}) for the first time. In comparison, Ca^{2+} cross-linked and acetic-acid coagulated rGO fibers (rGOF- Ca^{2+} and rGOF-Acetic acid) were also prepared as control systems. rGOF- Al^{3+} fibers, owing to their compact and well-aligned structure, offered the highest electrical conductivity, superior to most of rGO fibers reported in literature prior to thermal annealing. Meanwhile, trivalent cations, especially Al^{3+} , have led to more wrinkled fiber morphology with at least 20.5 % higher toughness and 4.8 times higher volumetric capacitance, as compared to that of Ca^{2+} and acetic acid coagulated rGO fibers.

3.2. Experimental Section

3.2.1. Materials

Natural graphite flakes (300 μm) were obtained from Asbury Graphite Mills USA. KMnO_4 , HI acid (55%), CaCl_2 , AlCl_3 , and FeCl_3 were purchased from Sigma-Aldrich and used as received. Concentrated H_2SO_4 (98%), HNO_3 , HCl (36.5%), glacier acetic acid, ethanol and H_2O_2 (30%) were purchased from Fisher Chemical.

3.2.2. Synthesis of GO

GOs were prepared from graphite powders following a modified Hummers' method.^{129,}
¹⁷⁰ Graphite powder (2 g) was added to a H_2SO_4 (98%, 100 mL) and HNO_3 (33 mL) mixture, stirring for 24 hours at room temperature. Then, the mixture was poured slowly into 1 L de-ionized (DI) water, followed by filtration to collect the solid. The solid was washed using DI water to neutralize pH and dried at room temperature to obtain the intercalated graphite compounds.

The intercalated graphite compounds were thermally expanded using a microwave (750 W) for 5 seconds to obtain worm-like expanded graphite (EG). EG was added to a 500 mL flask containing H_2SO_4 (98%, 267 mL) in an ice bath (0°C). KMnO_4 (10 g) was then added slowly to

the mixture under continuous stirring. After the introduction of KMnO_4 , the mixture was kept at room temperature and stirred for 12 hours. 1.5 L water was then added slowly to an ice bath (0°C). Shortly after the dilution with DI water, 30 mL H_2O_2 (30%) was added to the mixture, resulting in a bright yellow, bubbling solution.

We left the mixture to settle for 2 days after we decanted the clear supernatant. The remaining mixture was washed with HCl solution (10 %) and DI water successively until neutral, followed by dialysis for 2 weeks.

3.2.3. Fabrication of rGO Fibers

With a lab-scale, home-built wet-spinning apparatus, a GO spinning dope (15 mg mL^{-1}) was extruded through a spinneret (24 gauge) into the rotating coagulation bath, yielding a draw ratio of 1.3. The coagulation baths tested include 0.5 M AlCl_3 , 0.5 M FeCl_3 , 0.5 M CaCl_2 in H_2O /ethanol (3/1 v/v), and glacier acetic acid, respectively.

Subsequently, as-spun wet-state GO fibers from AlCl_3 , CaCl_2 , and FeCl_3 coagulation baths were washed with DI water. The reduced GO (rGO) fibers were prepared with hydroiodic acid (HI) reduction at 80°C for 12 hours, followed by cleansing with water and ethanol, and drying at 60°C in vacuum for 8 hours.

3.2.4. Structure Characterizations

The morphology of rGO fibers were characterized using a scanning electron microscope (SEM). Electrical conductivity of rGO fibers were measured by standard four-probe method. Mechanical properties were measured using a Q-test system with 1 mm/min extension rate and 1 cm gauge distance. All the electrical conductivity and mechanical properties were the average results of at least 5 samples.

The SSA of rGO fibers were measured by methylene blue adsorption method.^{119, 171} Generally, around 10 mg of rGO fibers were put into a flask and 100 μL of 1 mg/mL of MB solution were added at regular time. Then the remnant concentration of MB was measured by UV-Vis spectrophotometer at 664 nm. The SSA was calculated by the equation: $SSA = (m_{MB}/M_{MB})A_V A_{MB}(1/m_{fiber})$, where m_{MB} is the mass of the adsorbed MB, M_{MB} is the molar molecular weight (319.87 g mol⁻¹) of MB, A_V is Avogadro's number ($6.02 \times 10^{23}/\text{mol}$), A_{MB} is the area covered by one MB molecule (assumed to be 1.35 nm²) and m_{fiber} is the mass of rGO fibers.

3.2.5. Electrochemical Performance Characterizations

Electrochemical measurements, including the CV, GCD, and EIS were conducted in the solid state using electrochemical workstation (Autolab, Metrohm, USA). Two rGO fibers were aligned in parallel, soaked with gel electrolyte of H₂SO₄/polyvinyl alcohol (PVA)/H₂O (1/1/10 in weight), and dried at room temperature.

The specific volumetric capacitance (C_V), and area capacitance (C_A) of the electrode in a two-electrode cell was calculated according to $C_V = 2C/V_{fiber}$, and $C_A = 2C/S_{fiber}$, respectively, where C is the measured two-electrode configuration FSC capacitance, V_{fiber} and S_{fiber} are the volume, mass and surface area of the single fiber respectively. C could be obtained from CV test: $C = (1/2v) \times \oint IdU/\Delta U$, where v is the scan rate, I is the instantaneous current, ΔU is the voltage range. C could also be from GCD test: $C = t \times I/(\Delta U - U_{drop})$, where t is the discharge time, I is the discharge current, ΔU is the potential window, U_{drop} is the voltage drop in the discharge curve.

For the solid-state FSC, the volumetric capacitance ($C_{V-device}$) of the device was derived from the equation: $C_{V-device} = C/V_{device}$, where V_{device} is the volume of two fiber electrodes. The

volumetric energy density (E_V) and power density (P_V) of the FSC can be obtained from $E_V = C_{v-device} \times U^2/7200$, $P_V = E_V \times 3600/t$.

3.2.6. Density Functional Theory Calculations

The revised Perdew-Burke-Ernzerhof (RPBE)¹⁷² generalized gradient approximation (GGA)¹⁷³ functionals in conjunction with the projector augmented wave (PAW)¹⁷⁴ pseudopotentials were employed in our density functional theory (DFT)¹⁷⁵⁻¹⁷⁸ calculations using the Vienna Ab Initio Simulation package (VASP)¹⁷⁹⁻¹⁸². The plane-wave cutoff energy was set as 500 eV. The atomistic structures in our calculations were allowed to relax to the tolerance of atomic force at 0.01 eV/Å. Our graphene-oxide (GO) model was constructed from a perfect graphene structure (Figure 3.1). A GO layer was placed in a simulation cell with a size of 12.82 Å × 12.34 Å in the basal plane and with at least 13 Å vacuum in the normal direction. A 3×3×1 Monkhorst-Pack grid¹⁸³ was used to sample the Brillouin zone in our calculations.

The binding energy of hydrated cation on GO surface (E_b) was calculated as:

$$E_b = E_{tot} - E_{M-OH}$$

where, E_{tot} is the DFT calculated energy of the optimized structure with metal hydrated cation adsorbed on GO and E_{M-OH} is the DFT calculated energy of an isolated hydrated cation (*i.e.*, ion chelated by two OH groups).

To evaluate the strength of the cross-link formed by Al, Fe, and Ca between two GO layers, we calculated the energies of breaking the crosslink through removal of the bonds linked to either the upper or the lower GO layer. Namely, we performed the following two calculations for each crosslink.

$$E_{BD-up} = E_{M-GO-down} + E_{GO-up} - E_{tot}$$

$$E_{BD-down} = E_{M-GO-up} + E_{GO-down} - E_{tot}$$

where, E_{BD-up} and $E_{BD-down}$ denote the energies for breaking the bonds with the upper and lower GO layer, $E_{M-GO-down}$ and $E_{M-GO-up}$ are the DFT calculated energies of the relaxed lower and upper GO layer with metal atom adsorbed on, and E_{GO-up} and $E_{GO-down}$ are the DFT calculated energy of the relaxed upper and lower GO layer, respectively. Thus, the activation energy to break the crosslink is defined as the lower value of E_{BD-up} and $E_{BD-down}$.

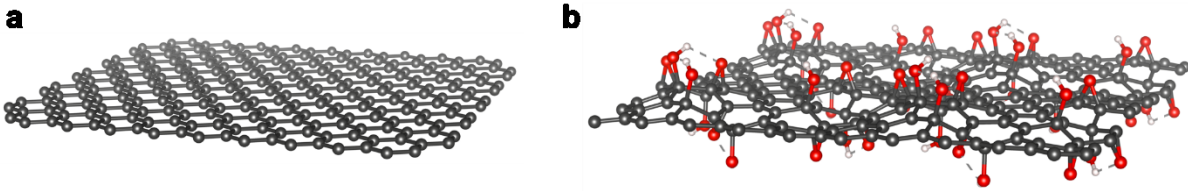


Figure 3.1 Atomistic structure of (a) single-layer graphene and (b) optimized structure of single layer graphene oxide (GO). In the figure, carbon, oxygen and hydrogen atoms are plotted as the black, red and white balls, respectively.

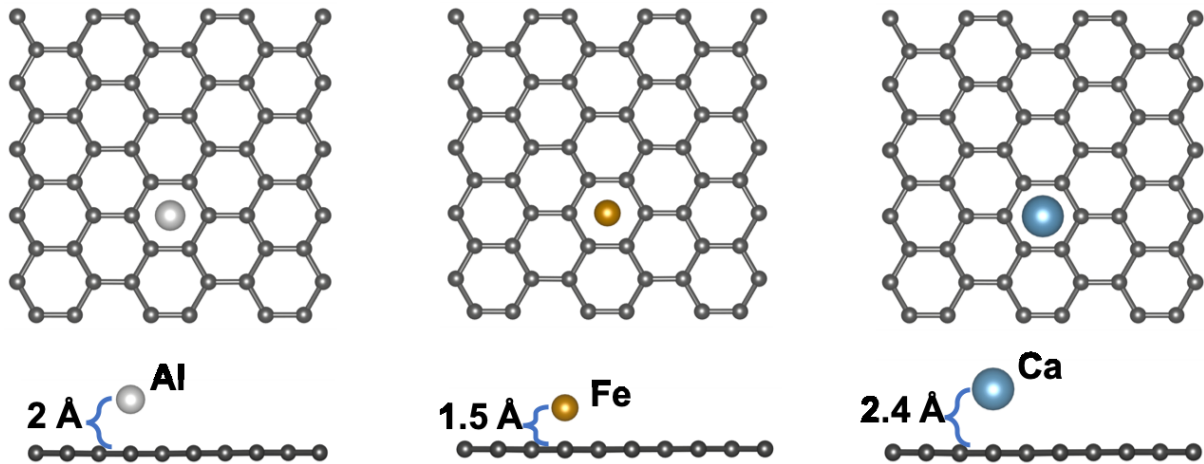


Figure 3.2 Top view (top) and lateral view (bottom) of metal cations adsorption configuration on a graphene layer through cation- π interaction and optimized by DFT method.

3.3. Results and Discussion

According to the wet-spinning protocol reported in our previous work (Figure 3.3),⁹ an aqueous dispersion of GO sheets, with average lateral dimension around 16 μm (Figure 3.4), was

extruded into a coagulation bath to form continuous GO fibers at room temperature. The GO sheets can be viewed as a 2D carbon lattice consisting of clustered nano- sp^2 regions and sp^3 carbon matrices.¹⁸⁴ In terms of coagulation mechanism, the interactions between multivalent metal cations and OCGs on GO sheets are believed to be responsible for the fiber formation and stabilization. In addition, due to the presence of abundant sp^2 clusters, the cation- π interactions between the cations and the π -ring electrons might also play a role for the fiber formation. With the shear stress applied during spinning and the wet-drawing applied during coagulation, GO sheets could be easily aligned along the fiber axis with multivalent cations bridged among them in our processes. The collected as-spun wet-state GO fibers were then washed with DI water to remove physically trapped cations, and then chemically reduced with hydroiodic acid (HI), during which the remaining OCGs were removed and the π -conjugation was partially restored for electrical conductivity.

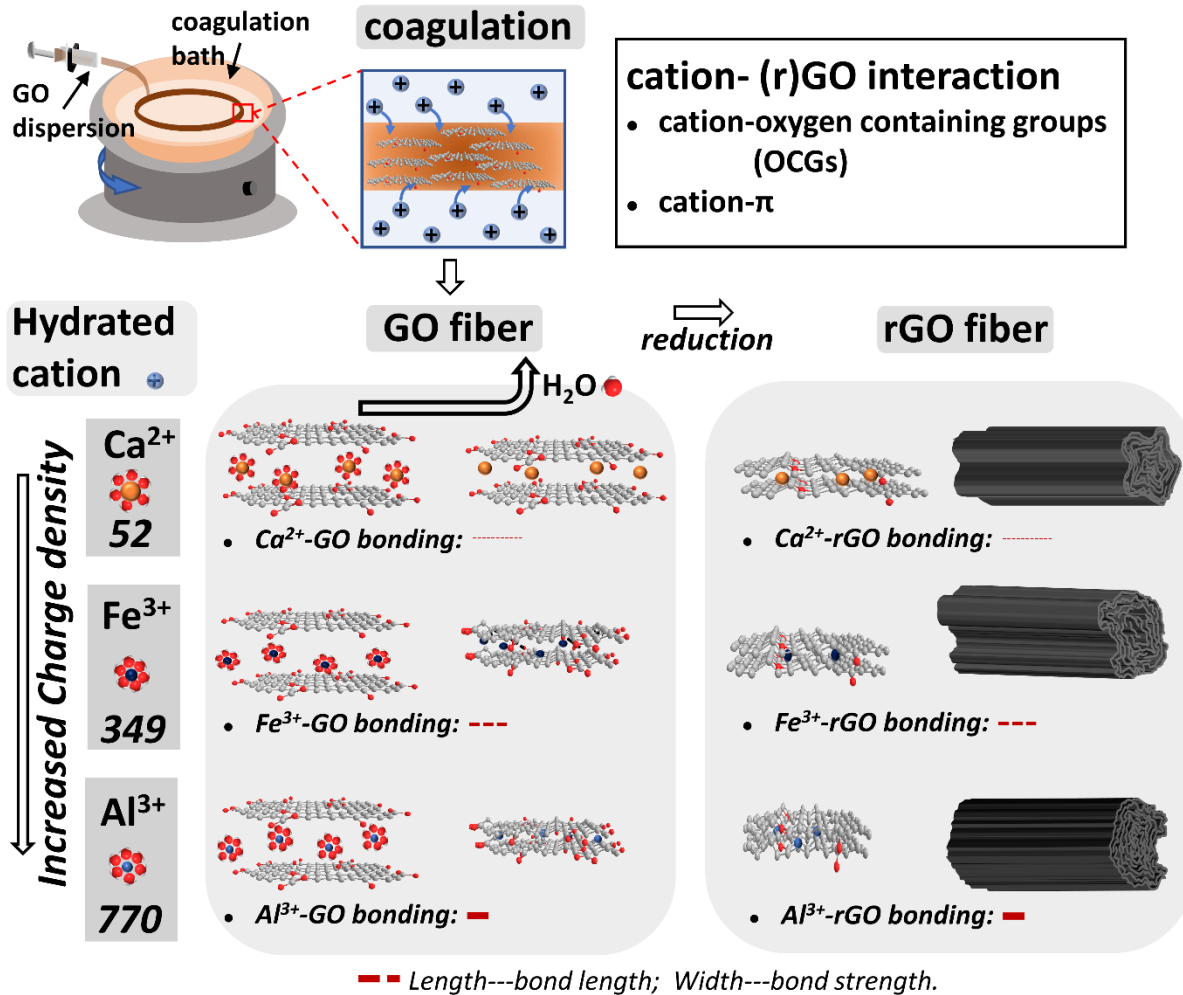


Figure 3.3 Schematic illustration of the formation of rGO fibers from divalent and trivalent cations in coagulation baths, respectively. After solvent evaporation and chemical reduction, rGO fibers with different cation cross-linking resulted in dramatically different morphologies.

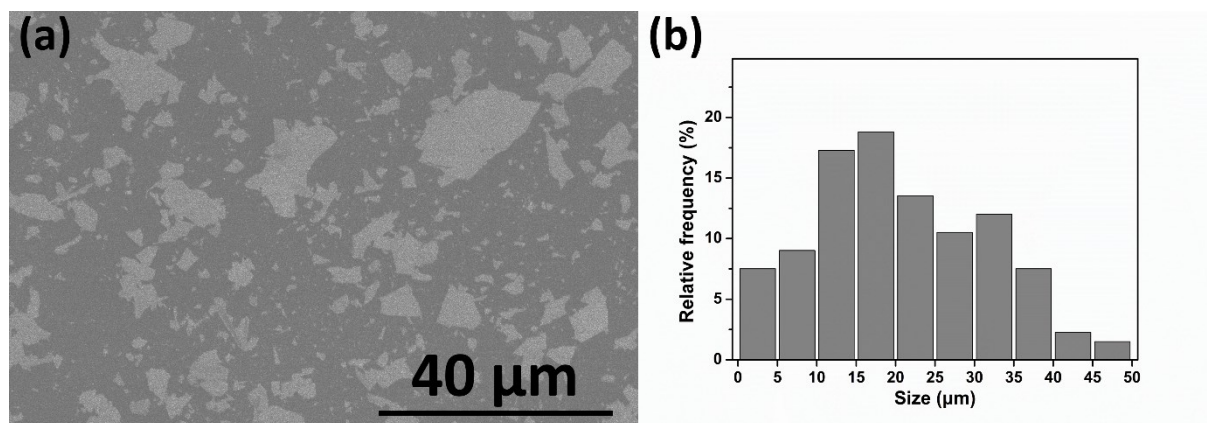


Figure 3.4 Size distribution of Graphene Oxide (GO) sheets. (a) an SEM image of GO sheets drop-casted onto a silica wafer; (b) the corresponding size distribution of the GO sheets. The average size of GO sheets is calculated to be *ca.* 16 μm.

The SEM images as shown in Figure 3.5 are highlighting the morphological disparity among the rGO fibers made from different coagulation baths. The trivalent cations (Al^{3+} and Fe^{3+}) coagulated rGO fibers are obviously much more wrinkled with macroscale pores on their surfaces. In comparison, the surfaces of rGO fibers from divalent cation Ca^{2+} and acetic acid are much smoother with only a few grooves aligned along the fiber axis direction. During the coagulation process, the hydrated cations (Al^{3+} , Fe^{3+} or Ca^{2+} ions) diffuse into the spaces in between the GO sheets (Figure 3.3) and form chemical bonding with the negatively charged OCGs on the GO surfaces. Meanwhile, these multivalent cations can also bind to the aromatic region through cation- π interactions.^{166, 169} To gain understanding of the interaction between cations and GO, we have performed the first-principles density functional theory (DFT) calculations (computational details are given in SI) to quantitatively investigate the interaction between cations and OCG abundant regions in GO, which we believe is the primary interaction existing in our system. DFT prediction of the structure and energy of partially hydrated Al^{3+} , Fe^{3+} or Ca^{2+} cations adsorbed on GO surface was first developed. A 78-atom GO model proposed by Shi-Tu^{166, 185} and Klinowski¹⁸⁶ *et al.* was

used with a formula of $C_{10}O_1(OH)_1$ and with OCGs, which are hydroxyl (-OH) and epoxy (-O-), randomly distributed on both sides of the GO sheet (Figure 3.1). Partial hydration of the cations was modeled as an ion chelated by two -OH groups. Figure 3.6a shows the optimized adsorption of the hydrated cations on GO surface. Our DFT results indicate that the cations prefer to be adsorbed on GO through the formation of ionic bonds with two adjacent epoxy groups at an average bond length of 1.87 Å for Al^{3+} -O, 1.90 Å for Fe^{3+} -O, and 2.38 Å for Ca^{2+} -O. Moreover, our DFT calculation predicted the binding strength of the partially hydrated cations on the GO surface to be 4.39 eV for Al^{3+} , 2.52 eV for Fe^{3+} , and 1.24 eV for Ca^{2+} , respectively. Consequently, our DFT results suggest that hydrated Al^{3+} has the highest tendency to form strong bonding with OCGs followed by Fe^{3+} , whereas hydrated Ca^{2+} has the lowest affinity among the three. Moreover, DFT method was used to calculate the binding energy between Al, Fe and Ca and the sp^2 carbon region *via* cation- π interaction (Figure 3.2)¹⁶⁹. It was predicted that the cation- π interaction with graphene were 0.73 eV for Al, 0.23 eV for Fe, and 0.24 eV for Ca, respectively. Hence, the cation-OCG interaction is dominantly stronger over the cation- π interaction in our DFT models. Meanwhile, the binding strength between the cation and the OCGs really depends on the physiochemical characteristics of the employed cations (Table 3.1), with higher charge density, leading to stronger cation-OCG interaction.

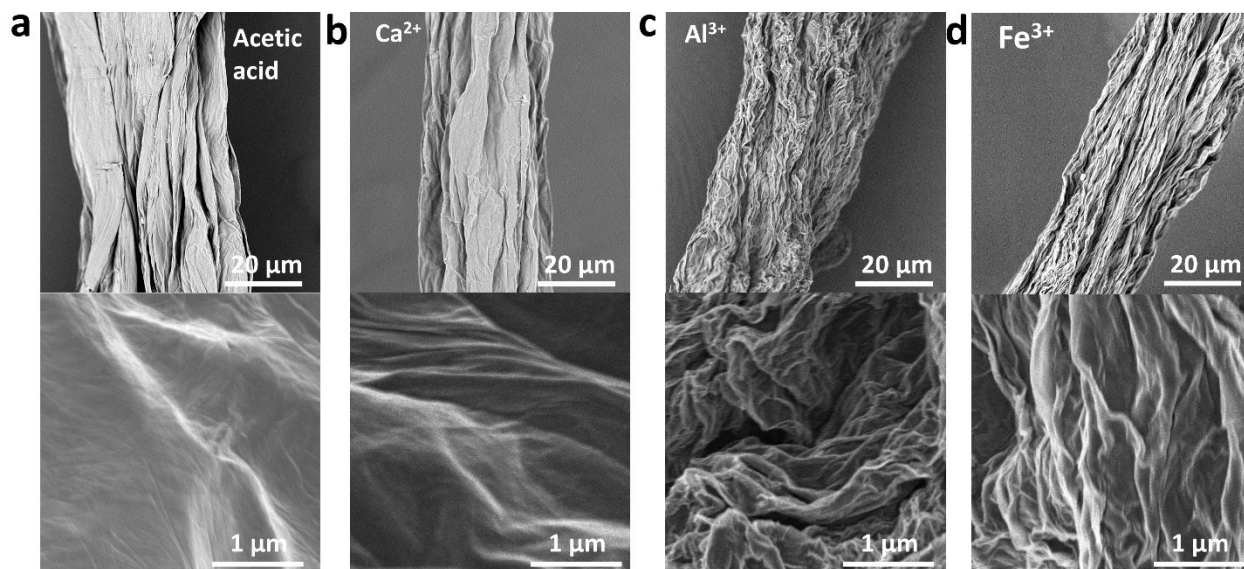


Figure 3.5 Morphologies of rGO fibers. SEM images of (a) acetic-acid coagulated rGO fiber; (b) Ca²⁺ coagulated rGO fiber; (c) Al³⁺ coagulated rGO fiber; (d) Fe³⁺ coagulated rGO fiber.

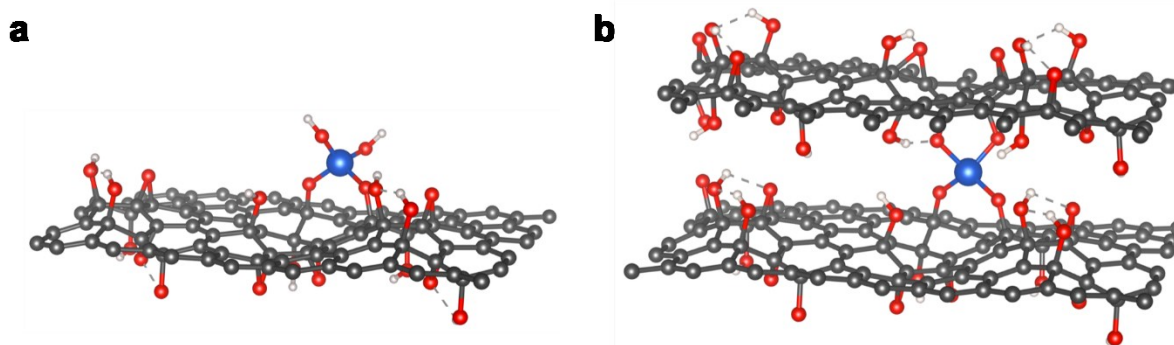


Figure 3.6 Atomic structures of hydrated cations adsorption on a single layer GO surface (a) and intercalated atoms between two GO layers (b). In the figure, the black, red, white, and blue balls represent carbon, oxygen, hydrogen, and cations (Al³⁺, Fe³⁺, or Ca²⁺), respectively.

Table 3.1 Physicochemical Properties of the Cations¹⁸⁷⁻¹⁸⁸

Metal cations	Ionic radius (Å)	Hydration shell thickness (Å)	electronegativity	Charge density (C mm⁻³)
Ca ²⁺	1.00	1.71	1.01	52
Fe ³⁺	0.65	2.88	1.83	349
Al ³⁺	0.50	3.24	1.61	770

As interlayer water molecules evaporate during drying process, the hydration shells of cations shrink gradually. As cations dehydrate (*i.e.*, releasing the two OH groups) and GO sheets approach each other, cations that are intercalated between two GO layers start to bind with two epoxy groups of the other GO layer (Figure 3.6b). In this case, the two GO layers are distorted around the intercalated cations, forming large wrinkles and pillars. According to our DFT calculation, it requires 3.97 eV, 2.77 eV, and 2.15 eV activation energy to break such a crosslink formed by Al³⁺, Fe³⁺, and Ca²⁺, respectively. Therefore, the local pinning of the GO layers by Al³⁺ and Fe³⁺ is very difficult to break once it is formed, leading to the corrugated assembly of GO layers. In the case of Ca²⁺, we believe that its low binding strength on the single layer GO (Figure 3.6a) has led to much less adsorption density on GO surface in the first step. Combining with relatively weak crosslinks between two neighboring GO layers, Ca²⁺ cations favor the formation of face-to-face stacking of GO sheets with less out-of-plane distortion comparing to Fe³⁺ and Al³⁺ cations.

After HI reduction, OCGs are partially removed and graphitic lattice is somewhat restored in rGO fibers. Al³⁺ cations, remaining in the rGO sheet galleries (Figure 3.7), possessing the strongest binding with the residue OCGs and graphitic lattice, give rise to the most buckling structure as observed in rGOF-Al³⁺ (Figure 3.5c). Regarding the bulking direction, due to the external force that applied along fiber axis during fibers formation, the wrinkles are mostly formed

throughout the cross-section of rGO fibers and perpendicular to fiber axis (Figure 3.8). Meanwhile, along the fiber axis, most of the rGO sheets have less prominent wrinkles and still maintain high level of orientation (calculation details are given in SI, Figure 3.9 and Table 3.2). From XRD patterns, Ca^{2+} cations with large radius leads to interrupted sheets stacking and broad XRD signal (Figure 3.10). Because of relative smaller radius of Al^{3+} , rGOF- Al^{3+} has a narrower peak with slightly lower inter-sheet spacing of 0.375 nm, as compared to that of rGOF- Ca^{2+} (0.377 nm). Comparing within trivalent cations, Fe^{3+} with lower charge density possesses weaker interaction with rGO sheets, resulting in less compact structure with larger inter-layer spacing (0.382 nm) (Figure 3.10) than that of rGOF- Al^{3+} . The SSA measurement results through methylene blue (MB) adsorption are (Table 3.2) in agreement with the morphological observations of rGO fibers. The rGOF- Al^{3+} gives the highest value of $685.8 \text{ m}^2 \text{ g}^{-1}$, ~14 % higher than that of rGOF- Fe^{3+} ($601.1 \text{ m}^2 \text{ g}^{-1}$) and ~51 % higher than that of rGOF- Ca^{2+} ($454.7 \text{ m}^2 \text{ g}^{-1}$) and rGOF-Acetic acid ($445.9 \text{ m}^2 \text{ g}^{-1}$).

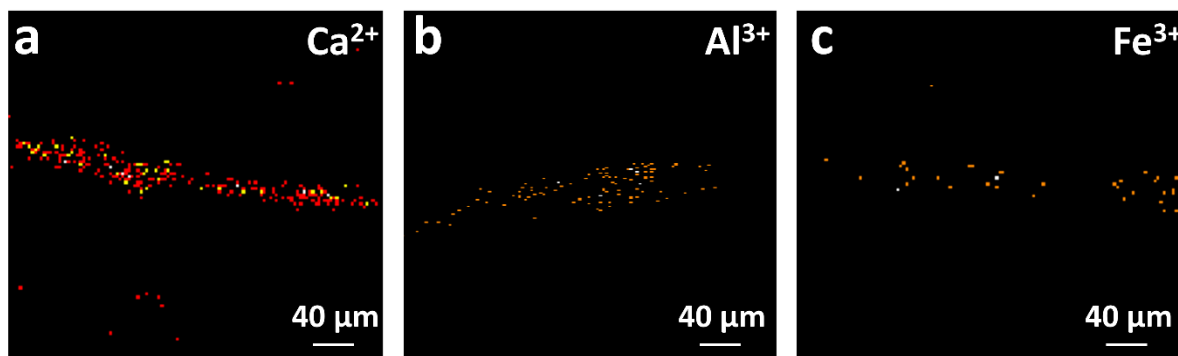


Figure 3.7 TOF SIMS secondary ion images of (a) Ca^{2+} , (b) Al^{3+} and (c) Fe^{3+} acquired from corresponding rGO fibers along fiber axis direction, confirming the existing of cations in rGO fibers. TOF-SIMS measurements were conducted with an ION-TOF TOF-SIMS V instrument with bismuth beam for analysis and cesium beam for sputtering.

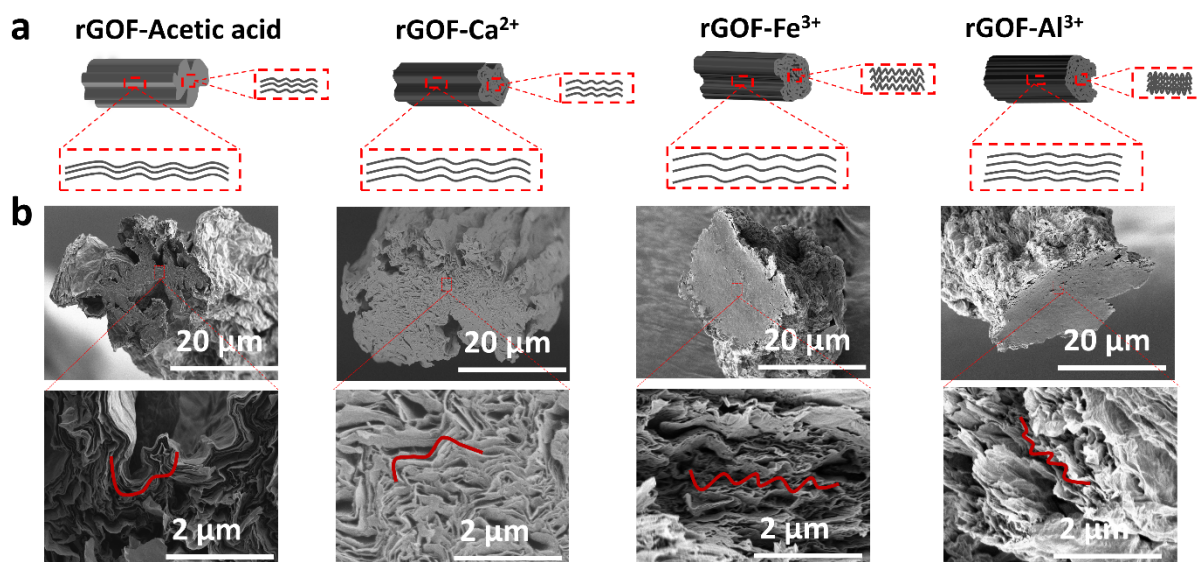


Figure 3.8 (a) Schematic illustration of the wrinkling direction of rGO sheets in each rGO fibers. (b) Cross-sectional SEM images of rGO fibers. rGOF- Al^{3+} has the most wrinkled structure through fiber cross-section (perpendicular to fiber axis), but still maintain good alignment along fiber axis.

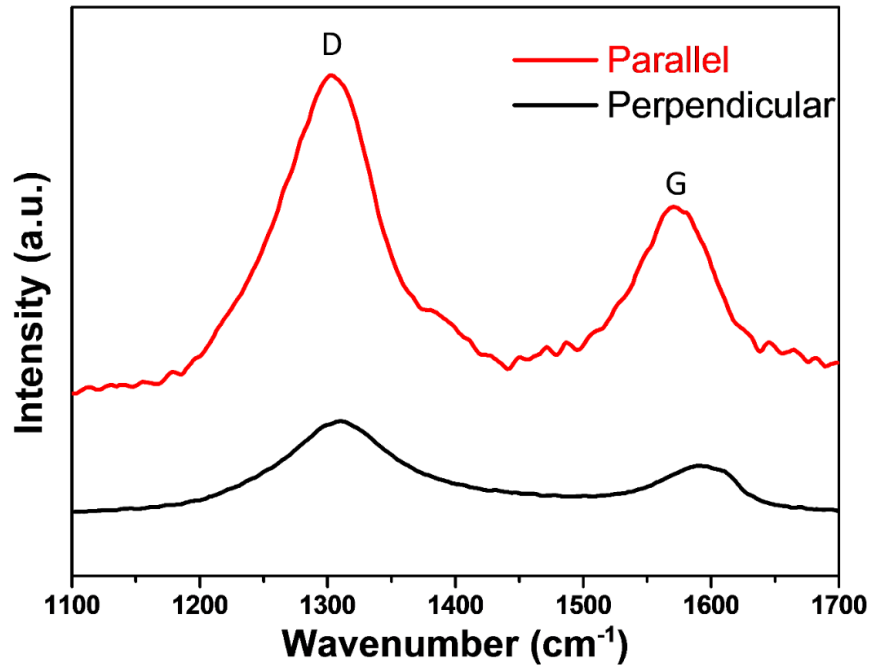


Figure 3.9 Typical polarized Raman spectroscopy of rGOF- Al^{3+} fiber with the incident laser beam parallel and perpendicular to the fiber axis, respectively. The Raman ratio, which is determined from the ratio between the G peak intensities of the two spectra (parallel I_{\parallel} vs. perpendicular I_{\perp}), provides a useful probe for the relative degree of alignment.

Table 3.2 SSA, mechanical, electrical and alignment properties of rGO Fibers. Fiber alignment was calculated from the ratio of G peak intensities (parallel I_{\parallel} vs. perpendicular I_{\perp}) of rGO fibers.

The ratio is the average of five measurements made over different positions of each fiber.

Sample	SSA/ $\text{m}^2 \text{g}^{-1}$	Tensile strength/ MPa	Breakage elongation/ %	Toughness/ $\text{MJ}\cdot\text{m}^{-3}$	Electrical conductivity/ $\text{S}\cdot\text{cm}^{-1}$	I_{\parallel}/I_{\perp} ratio
GO- Al^{3+}	685.8	164.9 ± 2.1	10.3 ± 2.1	10.0 ± 2.1	171.3 ± 9.1	2.36 ± 1.03
rGO- Fe^{3+}	601.1	154.7 ± 5.5	11.2 ± 3.5	8.7 ± 2.5	110.6 ± 5.7	1.80 ± 0.97
rGO- Ca^{2+}	454.7	240.9 ± 32.5	6.2 ± 0.9	8.3 ± 1.2	128.0 ± 6.2	1.67 ± 0.37
rGO- Acetic acid	445.9	145.6 ± 11.8	6.9 ± 0.8	4.1 ± 0.8	85.7 ± 0.9	1.92 ± 0.45

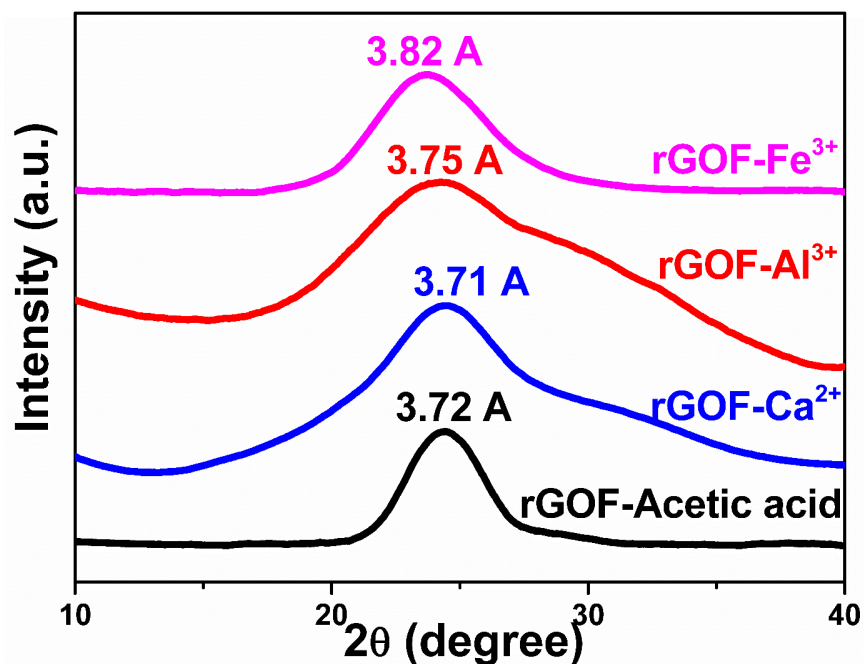


Figure 3.10 XRD patterns of rGO fibers. Fixed Time mode, step size 0.05 degree, dwell time 4 second. Wavelength to compute d-spacing 1.54059 Å, Cu/K-alpha 1.

Representative stress-strain curves of rGO fibers are depicted in Figure 3.11a and the mechanical properties along with the electrical conductivities of rGO fibers are summarized and compared in Table 3.2. It is evident that the composition of coagulation bath significantly influences the mechanical properties of the resulted rGO fibers. As expected, rGO fibers prepared by ionic cross-linking displayed higher tensile strength and toughness as compared to the non-solvent coagulation bath (acetic acid) where the cross-linking effect is absent. For rGO fibers coagulated from acetic acid, the lateral cohesion of adjacent rGO sheets can be assigned as van der Waals interactions as well as some residual hydrogen-bonding. For fibers coagulated from metal cations, in addition to van der Waals interactions, the interaction between cations with residue OCGs and aromatic planes also contributes to improve the fiber mechanical performance.

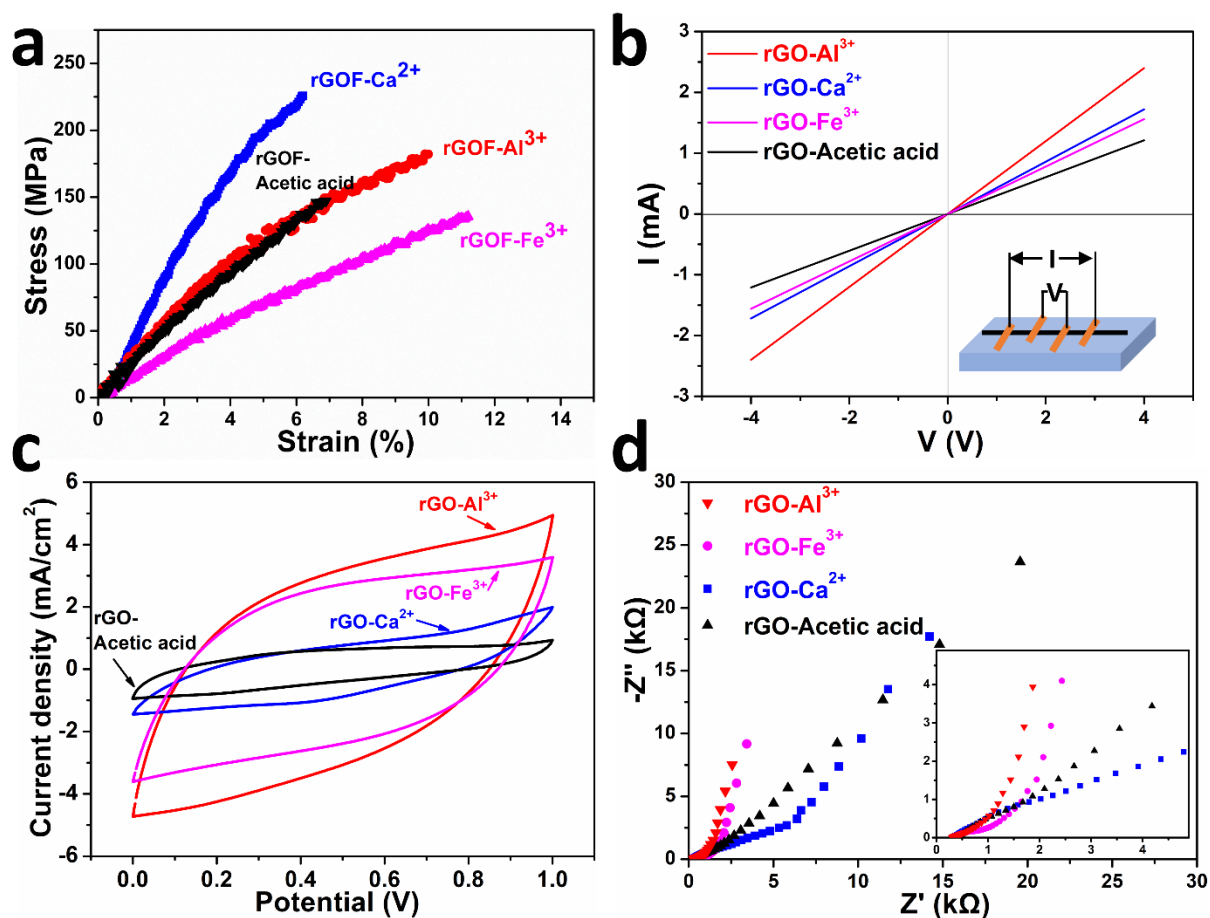


Figure 3.11 Comparison on the mechanical, electrical and electrochemical properties of rGO fibers coagulated from trivalent cation baths (Al^{3+} and Fe^{3+}), divalent cation baths (Ca^{2+}), and non-crosslinker acetic acid. (a) Representative stress-strain curves of rGO fibers prepared using various coagulation baths. (b) Typical I-V curves of rGO fibers with the length of 2 cm. The inset shows a schematic of our four-probe apparatus for the electrical conductivity measurements. (c) CV curves at 40 mV s^{-1} . (d) Nyquist plot from the EIS test.

Generally, Al^{3+} and Fe^{3+} cross-linked fibers exhibited medium tensile strength, but larger breaking elongation, resulting in higher toughness than that of Ca^{2+} and acetic acid coagulated fibers. Specifically, rGOF- Al^{3+} has a tensile strength of $164.9 \pm 2.1 \text{ MPa}$ at breaking elongation of $10.3 \pm 2.1 \%$, resulting in a toughness value of $10.0 \pm 2.1 \text{ MJ m}^{-3}$, 20.5 %, and 144.6 % higher than

that of rGOF-Ca²⁺ and rGOF-Acetic acid. High toughness against fracture under tensile stress indicates good flexibility which is favored for textile processing, such as twisting, weaving and knitting. Toughness of rGO fibers can be divided into two parts, *i.e.* the strain energy stored in the in-plane tensile deformation of rGO sheets and the one in the shear deformation of interlayer crosslinks¹⁸⁹. As compared to divalent Ca²⁺ and acetic acid coagulated rGO fibers, Al³⁺ and Fe³⁺ coagulated fibers have more wrinkled rGO sheets along the fiber axis, which can contribute more to the in-plane tensile deformation. Within rGO fibers coagulated from trivalent ions, rGOF-Al³⁺ with more compact structure exhibits higher tensile strength and slightly lower breaking strain as comparing to rGOF-Fe³⁺ with larger layer spacing.

The electrical conductivity of rGO fibers was measured by the four-probe method (Figure 3.11b inset) rather than two-probe method, mainly to eliminate the effect of contact resistance that originates from the contacting interfaces of electrical leads and connections.¹⁹⁰ Figure 3.11b shows the typical I-V curves of these rGO fibers. The rGOF-Al³⁺ shows the highest electrical conductivity ($171.3 \pm 9.1 \text{ S cm}^{-1}$) in comparison with other rGO fibers, mainly due to its compact structure and well-aligned rGO sheets along fiber axis. The capacitive performance of these rGO fibers is mainly ascribed to double-layer capacitance, which is proportional to electrolyte accessible surface area. rGO fibers coagulated from various chemicals were assembled into symmetrical parallel FSCs and evaluated based on their cyclic voltammogram (CV) responses at 40 mV s^{-1} (Figure 3.11c). All FSCs showed a quasi-rectangular CV curve representative of good double-layer formation. Obviously, fibers coagulated from trivalent ions exhibited much higher capacitance. For example, rGOF-Al³⁺ FSC exhibited a capacitance of 148.5 mF cm^{-2} (213.7 F cm^{-3}), ~ 4.8 times and 6.8 times higher than that of rGOF-Ca²⁺ and rGOF-Acetic acid based FSCs, respectively. This originated from the more wrinkled surfaces of trivalent cation-crosslinked rGO fibers as observed in Figure

3.5, offering much larger accessible area to electrolyte, and favoring the diffusion and adsorption of electrolyte ions.

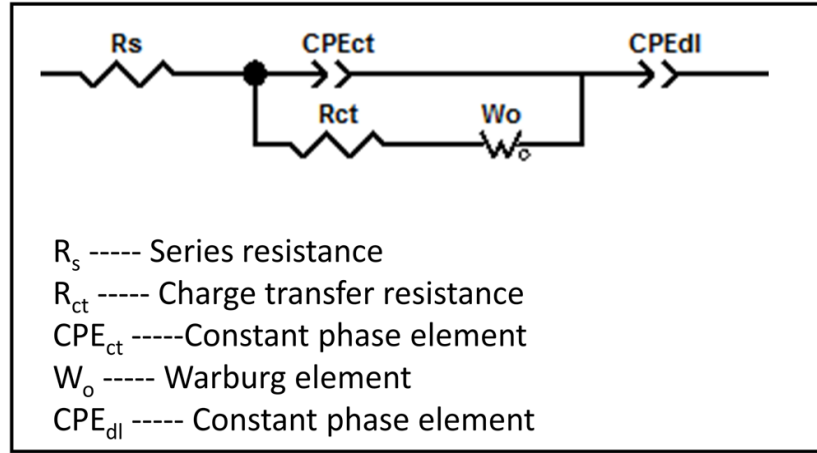


Figure 3.12 Equivalent circuit for fitting Nyquist plots in the high frequency region by Z-view.

Table 3.3 Z-view fitting results for Nyquist plots in Figure 3.8 d with the equivalent circuit shown in Figure 3.9.

Fitting Parameters	R_s/Ω	W_o			CPE_{dl}	
		R_w/Ω	T_w/s	α	Y_0/F	α
rGOF- Al^{3+}	227	889	20.13	0.53	0.51	0.92
rGOF- Fe^{3+}	349	1046	50.18	0.47	0.49	0.89
rGOF- Ca^{2+}	285	3379	299	0.99	0.14	0.65
rGOF-acetic acid	424	3890	357	0.99	0.08	0.59

In addition, electrochemical impedance spectroscopy (EIS) characterization was applied to evaluate the equivalent series resistance (ESR) of all the FSCs. Figure 3.11d shows the Nyquist plot with frequency ranging from 0.01 Hz to 0.1 MHz with amplitude of 10 mV which is analyzed by the equivalent circuit model (Figure 3.12). As presented in this model, R_s is the series resistance, which is related to both the electron conductivity and ion mobility.¹³² Since the same electrolyte used in all these FSCs, the R_s is in the same sequence as that of the electrical conductivity of the

corresponding fiber electrode. The charge transfer resistance (R_{ct}) represents the faradaic processes at the electrode and electrolyte interfaces. All the FSC systems here are absent of a semicircle in high frequency region, indicating that there are negligible R_{ct} between the electrolyte and electrodes. Warburg impedance (W_0) is associated with the diffusion of electrolyte ions within electrodes. CPE_{dl} represents the straight line, parallel to imaginary axis in the Nyquist plots at lower frequency, and it is proportional to the capacitance of these FSCs. As we can see, FSCs assembled from trivalent ions coagulated fibers have obviously shorter Warburg region (lower W_0), indicating better ion transport in the porous network. The shorter and more vertical line at lower frequency domain, imply the larger double layer capacitance in trivalent ion fibers. Accordingly, trivalent ion coagulated fibers exhibited much better EDLC performance comparing to the other rGO fibers. For comparison within trivalent ions coagulated fibers, rGOF- Al^{3+} exhibited 28% larger specific capacitance and 20% lower ESR than that of rGOF- Fe^{3+} , mainly owing to the higher electrical conductivity of rGOF- Al^{3+} .

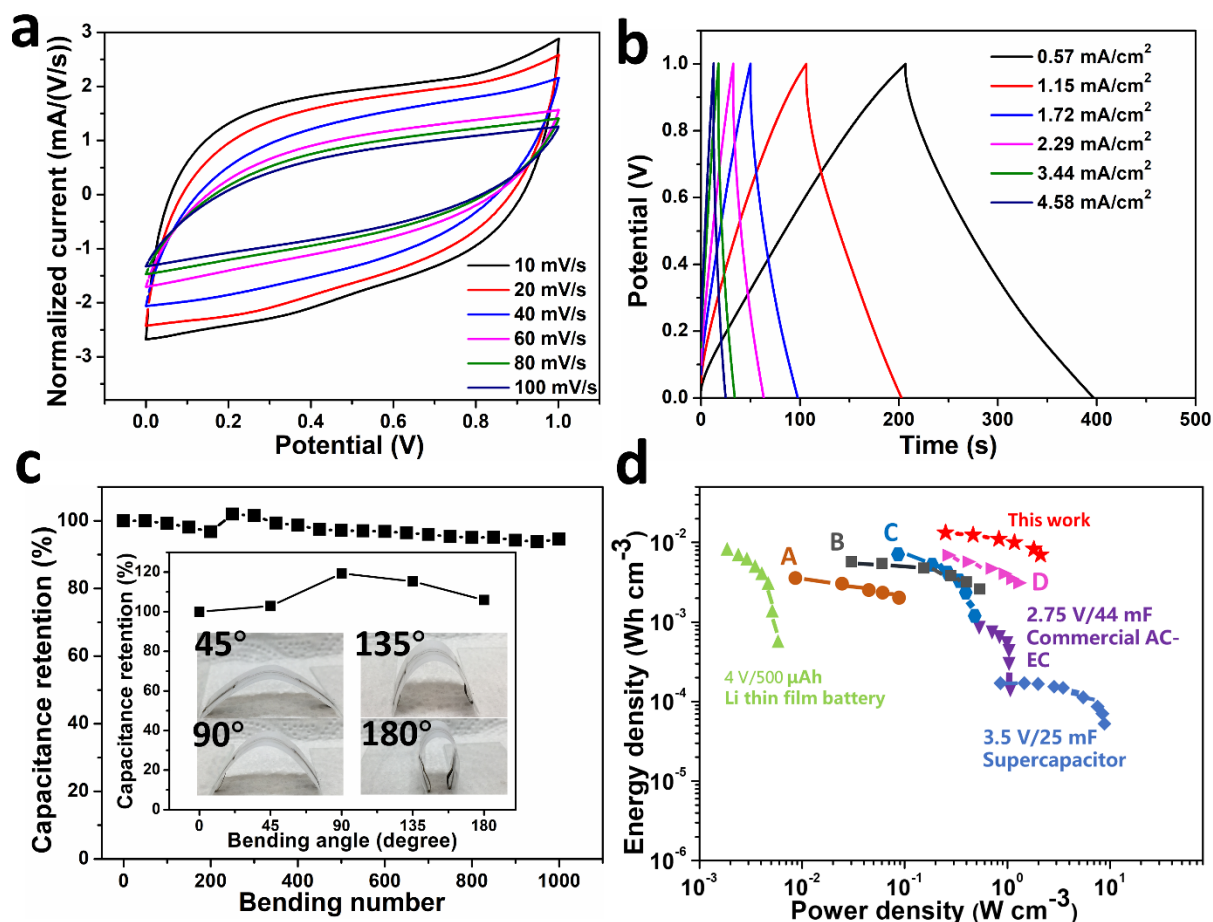


Figure 3.13 Electrochemical characterization of rGOF-Al³⁺ FSC in PVA/H₂SO₄ electrolyte. (a) CV curves at different scan rates and (b) Galvanostatic charge/discharge curves at different current density. (c) Capacitance retention as a function of bending cycles, the inset is capacitance stability upon bending from 0° to 180°. (d) Ragone plot of rGOF-Al³⁺ FSC compared with some commercial devices and other reported FSCs, including commercially available 4 V/500 μAh Li thin-film battery,¹⁹¹ 3.5 V/25 mF SC,¹⁹² 2.75 V/44mF commercial AC-EC⁷ and (A) hierarchically porous sheath-core graphene based FSC,⁸ (B) rGO/cellulose hybrid FSC,¹⁹³ (C) non-LC spinning pure rGO FSC,¹⁷¹ (D) rGO@NMP-FSC.⁹

To fully understand the performance of solid-state rGOF-Al³⁺ assembled FSC, we characterized its electrochemical behavior using CV and galvanostatic charge/discharge (GCD) measurements. As shown by the CV curves at different scan rates in Figure 3.13a, the FSC almost presents quasi-rectangular shape and can maintain their shape at the scan rate of 100 mV s⁻¹. The GCD curves exhibit nearly linear symmetrical shapes with coulombic efficiency of ~94%, implying the good reversibility of the FSC and good charge propagation between two rGOF-Al³⁺ electrodes (Figure 3.13b). The specific area capacitance of rGOF-Al³⁺ FSC calculated from discharge curve is showed in Figure 3.14. Clearly, rGOF-Al³⁺ FSC displays a large specific capacitance of 286.59 mF cm⁻² at a current density of 0.53 mA cm⁻². When the current density increases to as high as 10.62 mA cm⁻², the specific capacitance decreased to 106.51 mF cm⁻². This capacitance decay at high current density was most likely due to the insufficient ionic transport in the charge/discharge process.

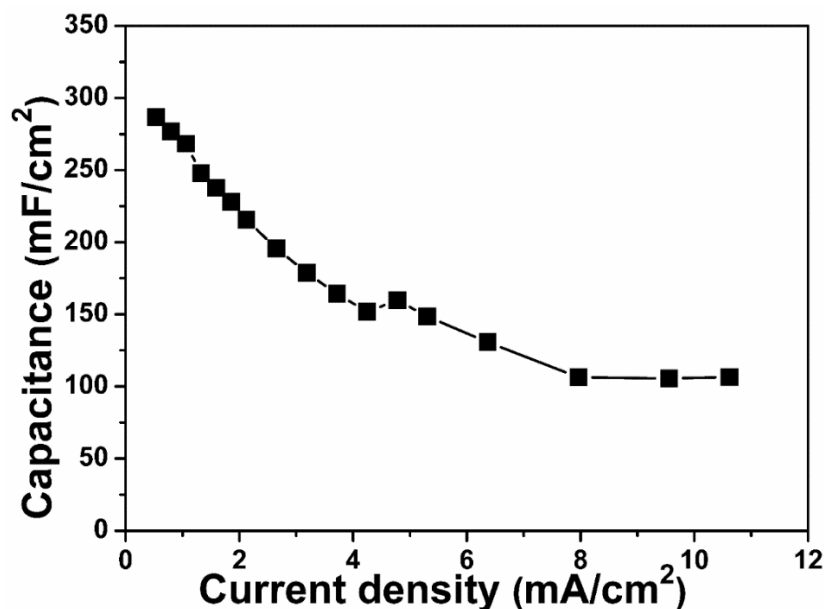


Figure 3.14 The calculated specific capacitance of rGOF-Al³⁺ FSC at different current density.

Table 3.4 Comparison of specific capacitance (based on a single electrode) and energy density (based on device) of solid-state FSC.

Fiber electrode	C_A (mF cm ⁻²)	C_V (F cm ⁻³)	C_M (F g ⁻¹)	C_L (mF cm ⁻¹)	E_A (μWh cm ⁻²)	E_V (mWh cm ⁻³)
GO@H ₂ O, AlCl ₃ bath, HI reduced (this work)	286.59 @0.53 mA cm ⁻²	382.12		2.7		13.26
GO@NMP, ethyl acetate bath, HI reduced ⁹	149.5 @0.15 A g ⁻¹ , 0.35 mA cm ⁻²	199.4	69.5 @10 mV s ⁻¹	1.4	5.12	6.8
NL GO@H ₂ O, acetic acid bath, HI reduced ¹⁷¹	78.7 @0.2 A g ⁻¹ , 0.085 mA cm ⁻²	226 @0.2 A g ⁻¹ , 0.085 mA cm ⁻²	185 @0.2 A g ⁻¹	/	/	7.26
GO&CNT@H ₂ O, CaCl ₂ bath, HI reduced ⁵³	177 @0.1 mA cm ⁻²	158 @0.1 mA cm ⁻²	/		/	3.5
CNT coated carbon fiber by spray coating ⁸²	86.8@ 0.38 mA cm ⁻²	14.1@5 mV s ⁻¹	11.1@5 mV s ⁻¹	/	/	0.14
GO@H ₂ O, CaCl ₂ bath, 800°C annealed followed by dip coating & carbonization ⁸	391.2 @0.1 mA cm ⁻²				8.7	
GO&CNC@H ₂ O, AA bath, HI reduced ¹⁹³		155.8@ 0.126 A cm ⁻³	123.3 @ 0.1 A g ⁻¹			5.1
GO@H ₂ O, CaCl ₂ bath, 800°C annealed, plasma ¹⁹⁴	36.25 @0.1 mA cm ⁻²				0.8	
GO&PEDOT:PSS, VC reduced ¹⁵⁶	115 @0.1 mA cm ⁻²	46			4.55 @0.02 mA cm ⁻²	1.8
GO&CNT, chitosan/AA bath, HI reduced ¹⁹⁵		38.8 @ mA cm ⁻³		0.35		1
GO&PPy&CNF, FeCl ₃ &HCl bath, HI reduced ¹⁹⁶	218 @0.1 mA cm ⁻²	334		4.2	7.4	7.4
GO&Mn ₃ O ₄ @DMF, ethyl acetate bath ¹⁹⁷						
GO@H ₂ O, NaOH/methanol bath, 650°C reduced, coating MnO ₂ ¹⁹⁸	16.7 @ 1 A g ⁻¹		245			
GO&MnO ₂ @H ₂ O, acetic acid bath, hydrazine reduction ¹⁹⁹	82.6 @60 mA cm ⁻³	66.1				5.8

Note: in wet spinning method, unless other mentioned, the spinning dopes are aqueous pure GO dispersion.

The fiber-shaped solid-state FSC also exhibited high flexibility, and is robust enough to undergo the one thousand bending cycles, which is a key requirement for wearable electronics applications. We measured the capacitance retention of the FSC under various bending angles (0° , 45° , 90° , 135° and 180°) (Figure 3.13c inset). An improved capacitance is observed upon bending and peaked at 90° (improved by 19%). This improvement might be due to the enhancement of electrolyte penetration within the unfolded wrinkles in the stretched region. In addition, high bending durability is observed with less than 10% decrease in capacitance after 1,000 bending cycles at 180° bending angle (Figure 3.13c).

The volumetric energy density (E_V) and power density (P_V) of the FSCs are more meaningful parameters for evaluating the energy-storage performance of the device. Figure 3.13d presents the Ragone plot of rGOF- Al^{3+} FSC, showing its E_V and P_V compared with commercially available supercapacitors and other FSC systems. It can be seen that the E_V and P_V of our rGOF- Al^{3+} FSCs are at the upper corner of the Ragone plot. The E_V of the rGOF- Al^{3+} (based on device) is up to $13.26 \text{ mWh cm}^{-3}$ at the current density of 0.71 A cm^{-3} (corresponding to a power density of $250.87 \text{ mW cm}^{-3}$), better than that of the $2.75 \text{ V}/44 \text{ mF}$ commercial activated carbon (AC)-electrochemical capacitor (EC) (0.7 mWh cm^{-3} at 590 mW cm^{-3}),⁷ and $3.5 \text{ V}/25 \text{ mF SC}$,¹⁹² and higher than that of $4 \text{ V}/500 \mu\text{Ah}$ Li thin-film battery ($0.3\text{-}10 \text{ mWh cm}^{-3}$).¹⁹¹ Moreover, this value also outperforms the recently reported various graphene and carbon fiber based FSCs (Table 3.4), such as hierarchically porous sheath-core graphene based FSC ($2\text{-}3.4 \text{ mWh cm}^{-3}$),⁸ rGO/cellulose hybrid FSC (5.1 mWh cm^{-3} at 30.7 mW cm^{-3}),¹⁹³ non-LC spinning pure rGO FSC (7.03 mWh cm^{-3} at 57.7 mW cm^{-3}),¹⁷¹ and our previously work: a FSC assembled from pure wet-spun rGO fiber originated from NMP based spinning dope (rGO@NMP-FSC) (6.8 mWh cm^{-3} at 120.4 mW cm^{-3}).⁹ The maximum volumetric power densities of our rGOF- Al^{3+} FSC was as high as 2109 mW

cm^{-3} at the current density of 5.7 A cm^{-3} , holding an obvious advantage over most of the reported systems.

3.4. Conclusion

In summary, we have demonstrated the use of Al^{3+} cations as a novel coagulant in the wet-spinning of GO/rGO fibers, which leads to higher toughness, superior electrical conductivity, and improved capacitance density of resulted rGO fibers as compared to that of other rGO fibers. As a trivalent cross-linker for GO fibers, Al^{3+} has an advantage over divalent cations (*e.g.* Ca^{2+}) in terms of generating much more wrinkled morphologies in the fibers, which facilitate the adsorption and diffusion of electrolyte ions. DFT modeling results have indicated the highest binding energy of Al^{3+} among the three cations with GO, providing a reasonable explanation of high wrinkling resulted in the Al^{3+} -based fibers. When compared to Fe^{3+} cations, Al^{3+} cations with much larger charge density, lead to more compact structure, and thus stronger and more conductive rGO fibers. The specific area capacitance of solid-state FSCs assembled with rGOF- Al^{3+} was up to 148.5 mF cm^{-2} at 40 mV s^{-1} , 1.4, 4.8 and 6.8 times higher than that of FSCs from rGOF- Fe^{3+} , rGOF- Ca^{2+} and rGOF-Acetic acid, respectively. It also shows excellent stability upon bending at various angles and good long-term bending durability. Furthermore, the maximum energy density of $13.26 \text{ mWh cm}^{-3}$ at 0.71 A cm^{-3} and the maximum power density of 2109 mW cm^{-3} at 5.7 A cm^{-3} of rGOF- Al^{3+} FSC are much higher than those of the reported rGO and carbon based FSCs. The investigation of trivalent ions as coagulation reagents for wet-spun GO fibers has shed light to the design and fabrication of conductive, flexible and high surface area rGO fibers for applications in wearable technologies.

Chapter 4 Graphene/MXene Supercapacitor Yarns as Weaveable

Energy-Storage Units

4.1. Introduction

Nowadays, more and more flexible electronic units have shown their potentials in a variety of wearable applications, such as high-performance sportswear, functional military uniforms, and biomedical garments, *etc.*²⁰⁰⁻²⁰¹ Researchers are currently trying to incorporate these pliable electronic components into fabrics, wherein they can function as sensors, actuators, communication devices, *etc.*, leading to smart fabrics that are of high demand in both civilian and military applications. However, one of the major obstacles in smart-textile (or e-textile) technologies, is the development of light-weight, wearable, and flexible power sources. The existing technologies such as pouch lithium batteries, coin cells, or hard “battery packs”, are bulky and rigid, and they consequently fail to meet the flexibility requirements of e-textiles.²⁰²⁻²⁰³ Thus, the development of wearable energy-storage devices exhibiting high mechanical flexibility, competitive performance and long-term stability is crucial to the widespread of applications of smart textiles.

Over the last decade, although some progress have been made on 2D film-based energy-storage devices using solid-state electrolytes (including polymer based and inorganic based solid-state electrolytes),²⁰⁴ sweat and vapor permeation are the major limiting factors when it comes to wearable applications, leading to inferior wearability and comfortness for e-textiles.^{203, 205} To mitigate these issues, one-dimensional (1D) devices such as fiber/yarn shaped batteries/supercapacitors, have emerged as an important alternative.^{53, 206-208} 1D devices with diameters ranging from micrometers to millimeters, are generally small in size, light-weight, and highly flexible. They can be woven or knitted into breathable fabrics with excellent wearability.

In addition, such unique 1D architectures also render them great design versatility since they can be conformed into desired shapes and can be placed at different locations compared to their 2D counterparts.²⁰⁹⁻²¹⁰ Furthermore, 1D devices have great potential to be easily integrated with other electronic fabrics, such as energy harvesting devices or sensors, to form integrated multifunctional systems.²⁰³

Supercapacitors (SCs), with fast charge-discharge and long cycling capabilities, are one of the promising power sources for portable and wearable applications.²¹¹ They can fill the gap between batteries and conventional capacitors, possessing a higher power density than batteries and fuel cells, and a higher energy density than conventional capacitors. For electrochemical double layer capacitors (EDLCs), carbonaceous materials such as activated carbon (AC), carbon nanotubes (CNTs), graphene *etc.*, being electrically conductive and retaining high specific surface areas (SSA), have been the dominating choices for electrode materials of supercapacitors.²¹² Among these materials, graphene (oxide) offers high wet-chemical processability, which can be easily wet-spun into fibers and yarns adopting traditional solution-spinning recipes, thus graphene has been selected as the basic building blocks for 1D wearable devices, *via* the solution processing of its chemical precursor, *i.e.*, graphene oxide (GO). Many researchers have focused on fabrication of high-performance graphene-based fiber-shaped SCs (FSCs) by improving the SSA or wettability of graphene fiber electrodes.^{9, 118, 193, 213-214}

However, due to the nature of EDLC, the specific capacitance originated from the pure graphene fiber is still limited. As compared to EDLC, pseudocapacitor is another sub-class of SCs, utilizing both faradic redox reactions and double-layer capacitance, which can potentially provide much higher energy densities.²¹⁵ Thus, introducing pseudocapacitive materials into graphene-based fibers is a feasible and an attractive way to improve the capacitance and energy density

within limited fiber volumes. Commonly used pseudocapacitive materials include metal oxides and sulfides, such as MnO_2 ,²¹⁶⁻²¹⁷ Mn_3O_4 ,¹⁹⁷ MoS_2 ,²¹⁸ NiCo_2S_4 ²¹⁹ *etc.* all of which have been introduced into graphene fibers to explore its potential. However, because of their low electrical conductivity, these materials led to compromised power density in FSCs.

In recent years, a new family of 2D early transition metal carbides, “MXene”, have attracted enormous attention as a new group of 2D functional materials.²²⁰ MXene with a general formula of $\text{M}_{n+1}\text{X}_n\text{T}_x$, (M = transition metal, X = C, n = integer between 1 and 3, and T_x = surface functional groups), possess good electrical conductivity, good redox function, and high capacitance.²²¹ So far, Razal's²²² and Gao's²²³ groups have reported the successful incorporation of MXene ($\text{Ti}_3\text{C}_2\text{X}$) flakes into graphene fibers through direct wet-spinning processes, which led to higher capacitance of the resulted fiber electrodes, as compared to their pure graphene fibers counterparts.

In order to achieve practical application towards energy-storage fabrics, individual fiber electrodes need to be assembled into SCs in yarn structures (YSCs), which can then be converted into fabrics through textile processing (weaving or knitting). So far, researches in this field have been dedicated to fabricating individual fibers but their processability into YSCs and ultimate fabrics remain largely unexplored. Besides the twisting of wet-spun fibers, another strategy towards YSCs is to start with existing yarns, such as cotton yarns, Nylon, PET or carbon yarns *etc.*^{192, 202, 224-226} and coat or electrochemically deposit active materials onto the fiber surfaces within the yarns. This method has a few disadvantages: 1) it does not provide enough crock fastness, since the coated materials can easily fall off upon friction; 2) those natural yarns contribute to the weight and volume as structural materials, but do not store energy or offer electrical conductivity. On the contrary, YSCs made of individual GO/MXene fibers exhibit more

stable and adjustable structure, offering higher volumetric/gravimetric densities, since no extra supporting framework was involved.

In this study, we report the fabrication of heterostructured fibers of titanium carbide ($\text{Ti}_3\text{C}_2\text{T}_x$) MXene and graphene (oxide) *via* wet-spinning. More importantly, liquid electrolyte mediation has been employed in our system to improve the electrolyte diffusion in each fiber electrodes, *via* the incorporation of the H_2SO_4 electrolyte in between graphene and MXene layers, thus leading to excellent linear and areal energy and power performance of our YSCs. The scalable fabrication of YSCs is also demonstrated by twisting certain number of fibers together. The capacitance of ultimate YSCs can be adjusted by controlling fiber numbers that are incorporated in one yarn. In addition, here we evaluate the bending stability of the YSCs and their feasibility for further textile processing.

4.2. Experimental Section

4.2.1. Synthesis of GO and MXene ($\text{Ti}_3\text{C}_2\text{T}_x$)

GO was prepared from graphite flakes ($\sim 300 \mu\text{m}$) by a modified Hummers' method according to our previous published paper. Multilayered $\text{Ti}_3\text{C}_2\text{T}_x$ was synthesized through etching of Ti_3AlC_2 powders. Specifically, 2.4 g of LiF was dissolved in 30 mL of 9 M HCl. Then 1.5 g of Ti_3AlC_2 powders was added gradually into the above mixture solution and kept at 23°C for 24 h while stirring. Afterword, the solid residue was washed with deionized (DI) water and then centrifuged until the pH of the supernatant was 6~7, followed by vacuum filtration and drying under vacuum to obtain multilayered $\text{Ti}_3\text{C}_2\text{T}_x$.

4.2.2. Fabrication of Fibers

$\text{Ti}_3\text{C}_2\text{T}_x$ solution with certain concentration was prepared by adding multilayered $\text{Ti}_3\text{C}_2\text{T}_x$ in DI water, followed by sonication for 1 h. A given amount of GO aqueous dispersion was added

to $\text{Ti}_3\text{C}_2\text{T}_x$ solution according to various weight ratio between GO and MXene. The mixture was magnetically stirred for 24 h at 200 rpm.

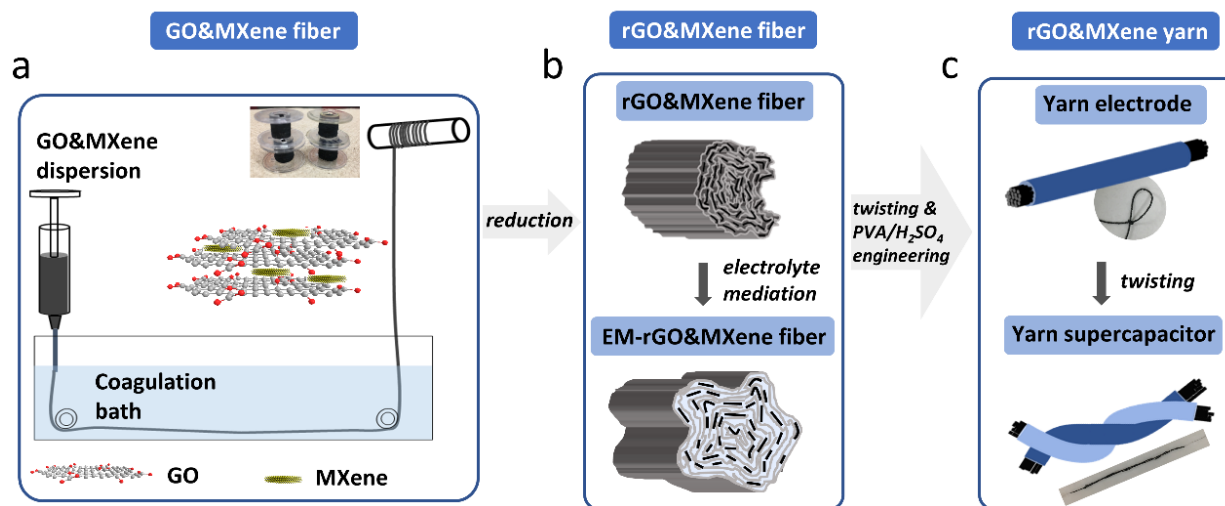


Figure 4.1 Fabrication of rGO & MXene based fibers and corresponding YSCs. (a) Schematic illustration of wet-spun GO & MXene fibers. (b) Fabrication of electrolyte mediated rGO&MXene fibers. (c) Fabrication of rGO&MXene fibers-based yarn electrodes and supercapacitors.

The GO&MXene mixture was loaded into a 10 ml plastic syringe with a spinneret (24 gauge) and injected into the trough-shaped coagulation bath (glacier acetic acid), followed by collecting on a bobbin (Figure 4.1a). Then, the dried GO&MXene fibers were reduced by HI at 85°C for 12 h. After washing with ethanol and drying in vacuum, final rGO&MXene fibers were obtained.

For electrolyte mediation to fabricate hydrogel EM-rGO&MXene fibers, the as-reduced wet-state rGO&MXene fibers were put in a 1 M H_2SO_4 solution and stirred continuously at a rate of 200 rpm for 24 h, allowing water in wet-state fibers to be fully exchanged with the mixture solution, *i.e.* miscible mixture of volatile (H_2O) and nonvolatile liquids (H_2SO_4); afterwards, the

fibers were moved to a vacuum oven. Thus, the volatile liquid (H_2O) inside the gel fiber would evaporate and be selectively removed. The non-volatile part (H_2SO_4) in the gel fiber would remain.

4.2.3. Fabrication of YSCs

Continuous EM-rGO&MXene yarn electrode was prepared by introducing twists automatically in assistance of the mechanical motor. The direction of twist and degree of twist were controlled by the rotation direction and rotation speed of the turntable, respectively. Certain fibers were twisted with 5 twists per centimeter. The prepared yarns were soaked with PVA- H_2SO_4 solution (1/1/10 in weight) for 5 mins, and then allowed to solidify at room temperature for 10 mins. The coating was repeated for three times to get the yarn electrode. Then two yarn electrodes were plied and inserted with twists to get the ultimate YSCs.

4.2.4. Structural Characterizations

The structure and morphology of fibers were characterized by SEM (FEI Verios 460L). The XRD patterns were recorded on Rigaku SmartLab X-ray diffractometer (40 kV, 44 mA, $\text{Cu K}\alpha$ radiation) at room temperature. Raman spectra were recorded using a Nomadic Raman Microscope with a $50\times$ objective lens and a 532 nm He-Ne laser beam at room temperature. Electrical conductivity of fibers was measured by standard four-probe method. The tensile and cyclability tests were performed on the Q-test system. For fibers, the test conditions were 1 mm min^{-1} extension rate and 1 cm gauge distance. For yarns, the test conditions were 10 mm min^{-1} extension rate and 10 cm gauge distance. In tensile cyclic test, the yarns were stretched to certain elongation at a rate of 10 mm min^{-1} and repeated for certain cycles. The final measurement of electrical conductivity and mechanical properties were derived from the average results of 5 samples.

4.2.5. Electrochemical Performance Characterizations

Electrochemical performance, including cyclic voltammetry (CV), galvanostatic charge/discharge (GCD) measurement was conducted using electrochemical workstation (Autolab, Metrohm, USA). For FSCs, two fibers were aligned in parallel, soaked with gel electrolyte of H₂SO₄/Polyvinyl alcohol (PVA)/H₂O (1/1/10 in weight), and dried at room temperature.

The specific gravimetric capacitance (C_M), areal capacitance (C_A) and length capacitance (C_L) of the electrode in a two-electrode cell was calculated according to $C_M = 2C/M_{fiber}$, $C_A = 2C/A_{fiber}$ and $C_L = 2C/L_{fiber}$ respectively, where C is the measured two-electrode configuration FSC capacitance, M_{fiber} , A_{fiber} and L_{fiber} are the mass, surface area and length of the single fiber, respectively. C could be obtained from CV test: $C = (1/2v) \times \oint IdU/\Delta U$, where v is the scan rate, I is the instantaneous current, ΔU is the voltage range. C could also be from GCD test: $C = t \times I/(\Delta U - U_{drop})$, where t is the discharge time, I is the discharge current, ΔU is the potential window, U_{drop} is the voltage drop in the discharge curve.

For the YSC, the areal capacitance ($C_{V-device}$) and length capacitance ($C_{L-device}$) of the device was derived from the equation: $C_{V-device} = C/V_{device}$, and $C_{L-device} = C/L_{device}$, where C is the measured capacitance of the YSC, V_{device} and L_{device} is the volume and length of the YSC, respectively. The energy density (E) and power density (P) of the FSC can be obtained from $E = C_{device} \times U^2/7200$, $P = E \times 3600/t$.

4.3. Results and Discussion

4.3.1. Fabrication of Graphene & MXene Heterostructured Fibers

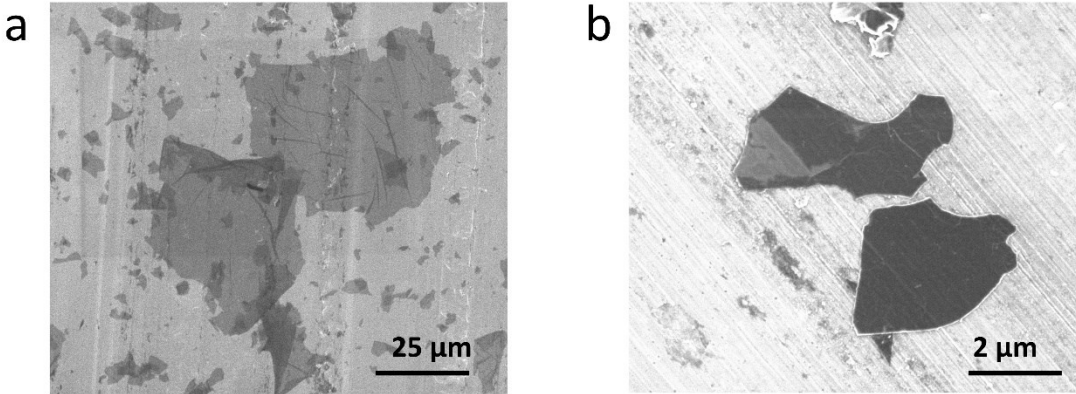


Figure 4.2 SEM images of graphene oxide sheets (a) and MXene sheets (b).

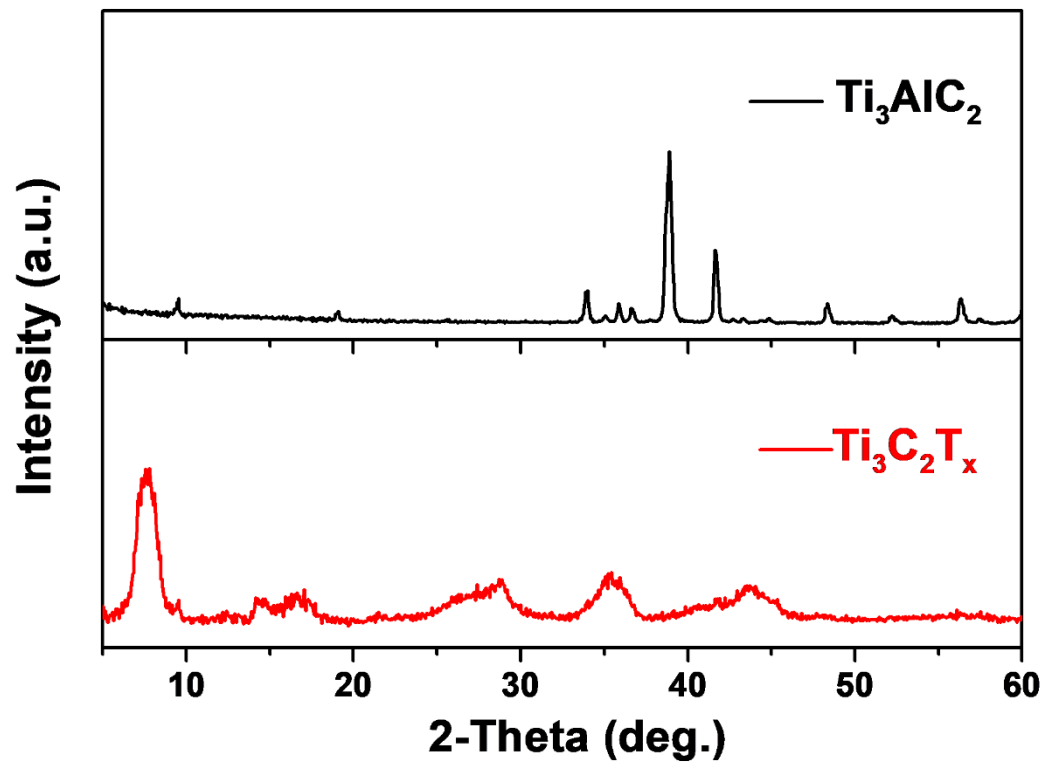


Figure 4.3 XRD pattern of MAX (Ti₃AlC₂) and MXene (Ti₃C₂T_x) powder.

Among all the synthetic techniques used to produce MXene, the one that involves etching the MAX phase (Ti₃AlC₂) in LiF-HCl have been known to offer the most promising

electrochemical performance.^{221, 227} Herein, we synthesized MXene ($\text{Ti}_3\text{C}_2\text{T}_x$) according to this method, with sizes ranging from hundreds of nanometers to several micrometers (0.2 - 3 μm) (Figure 4.2b). The X-ray diffraction (XRD) pattern revealed the characteristic peaks (000 l) of MXene and the disappearance of MAX peaks (Figure 4.3), indicating the successful synthesis of MXene. Together with GO (1- 30 μm , Figure 4.2a), 2D heterostructured graphene oxide (GO)&MXene fibers were fabricated through the wet-spinning process (Figure 4.1a). The corresponding reduced graphene oxide (rGO)&MXene fibers were obtained *via* hydroiodic acid (HI) reduction.

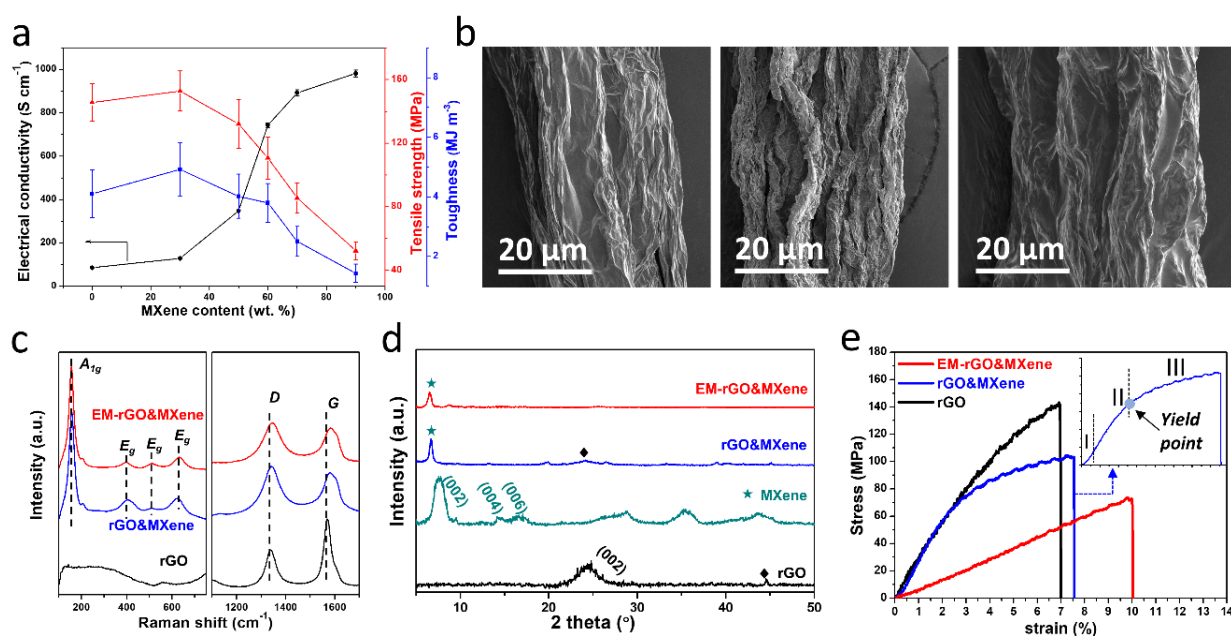


Figure 4.4 Characterization of fibers. (a) The relation between the mass ratio of incorporated MXene with the electrical conductivity, tensile strength and toughness of fibers. (b) SEM images of the surface of rGO fibers (0 wt% MXene), rGO&MXene fibers (60 wt% MXene) and EM-rGO&MXene fibers (60 wt% MXene) (from left to right). (c-e) Raman spectra (c), XRD spectra (besides fibers, the spectra of MXene was collected in particles) (d), and typical stress-strain curves (e) of rGO fibers, rGO&MXene fibers and EM-rGO&MXene fibers.

Thanks to the formation of liquid crystals (LCs), which originates from the large aspect ratio of GO sheets, GO dispersion can be successfully wet-spun into continuous fibers.^{2, 28} Comparing to atomic layers of GO, the LiF-HCl synthesized MXenes are multilayered and each layer of MXene is five-atom thick. Also, the lateral size of MXene ranges from hundreds of nanometers to several micrometers, which brings relative low aspect ratios and high bending rigidity, making them difficult to be wet-spun into continuous fibers. Therefore, the ratio between GO and MXene in the spinning dope would influence its spinnability and the properties of corresponding heterostructured fibers.

Both GO and MXene have negative zeta potential,²²⁸ their mixture in water can easily form a stable dispersion. By comparing the rGO & MXene heterostructured fibers that spun from spinning dopes with different weight ratios between GO and MXene (with MXene content 0%, 30%, 50%, 60%, 70%, and 90%), we identified a trade-off between mechanical properties and electrical conductivity of the final fibers. The 60 wt% of MXene gives a balanced performance of rGO & MXene fibers, which exhibit high electrical conductivity (743.1 S cm^{-1}), while maintaining reasonable mechanical strength (110.7 MPa) and toughness (3.8 MJ m^{-3}) (Figure 4.4a). The heterostructured fibers originated from MXene mass loading of 60 wt% was further investigated and compared with pure rGO fibers. In the following sections, the term rGO&MXene fibers refer to the fibers with 60 wt% MXene. We carefully evaluated the fabrication scalability of rGO&MXene fibers *via* wet-spinning technique. Tens of meters long continuous GO&MXene fibers have been prepared using the wet-spinning setup in Fig 1a from a 10 ml spinning dope. This process can be easily scaled up to get longer fibers by increasing the volume of spinning dope.

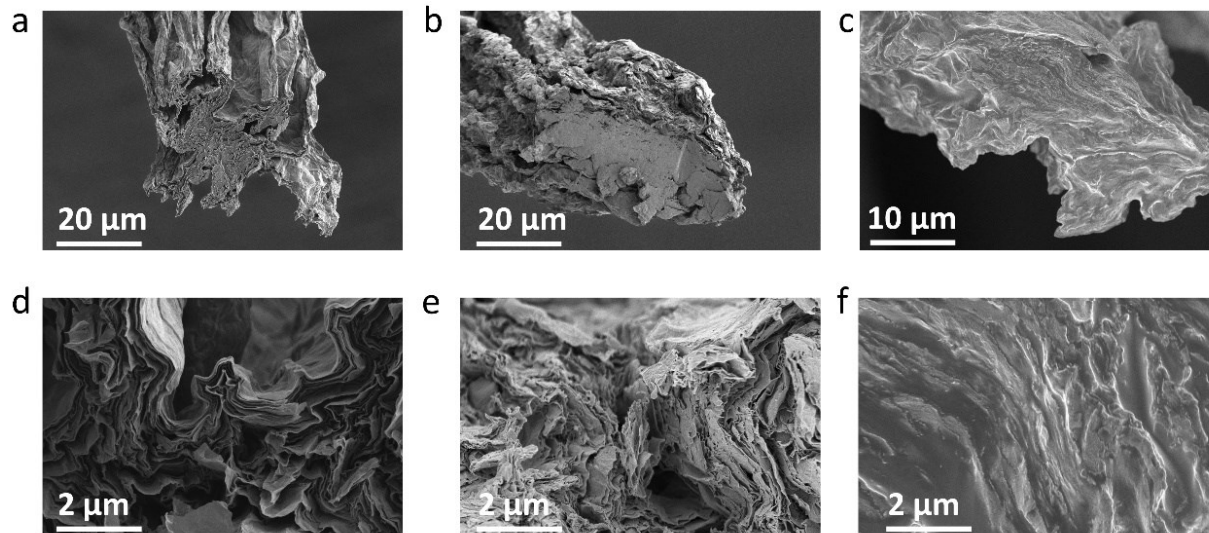


Figure 4.5 SEM images of fiber cross-sections of (a,d) rGO fiber; (b, e) rGO&MXene fiber; (c, f) EM-rGO&MXene fiber.

Scanning electron microscope (SEM) (Figure 4.4b) analysis revealed that the heterostructured rGO&MXene fibers have a more wrinkled surface morphology as comparing to pure rGO fibers which show much smoother surface. This trait can be attributed to the stacking of rGO and MXene sheets with a variety of lateral sizes and thicknesses, leading to distinct thermal fluctuations and elastic strains.²²⁹⁻²³⁰ Due to a negative thermal coefficient and lower in-plane stiffness of rGO sheets, upon interaction with MXene, out-of-pane deformations can be readily formed.²²⁹ The cross-sectional SEM images of pure rGO fibers (Figure 4.5 a&d) show irregular shape with well-aligned, layered structure. With the introduction of MXene sheets, the rGO&MXene fibers (Figure 4.5 b&e) maintain the layered structure but exhibit more crumpled and porous structure, due to more grain boundaries that are brought by the smaller-sized MXene.

Raman spectra (Figure 4.4c) of rGO&MXene fibers exhibited the signatures of the $Ti_3C_2T_x$ -MXene. Specifically, the mode at 198 cm^{-1} are A_{1g} symmetry out-of-plane vibrations of Ti and C atoms, while the modes at 284 , 366 , and 624 cm^{-1} are the E_g group vibrations, including in-plane (shear) modes of Ti, C, and surface functional group atoms.²³¹ With the existence of rGO

sheets, two broad bands appear at 1312 and 1588 cm^{-1} for all kinds of fibers, which are characteristics for the D and G bands of graphitic carbon, specifically.²³² Compared with those of pure rGO fibers, the G band of rGO&MXene fibers redshift by 16 cm^{-1} , which is probably caused by the interaction between MXene and rGO layers, generating tensile strains of rGO sheets.^{231, 233} The D band is due to defects and is related to zone boundary k-point phonons with A_g symmetry.²³⁴⁻²³⁵ The G band corresponds to collective symmetric stretching of sp^2 carbon lattice with E_g symmetry.²³⁴ The ratio of D-band intensity to G-band intensity (I_D/I_G) increase from 0.56 of pure rGO fibers to 1.04 of fibers with 60 wt% MXene incorporated. This indicates that MXene has disturbed the out-of-plane stacking order of rGO sheets.

XRD pattern (Figure 4.4d) provides further evidence of intercalation. rGO fibers displayed a peak at around 24.5° , corresponding to a d_{002} distance of 3.6 Å. After intercalated 60 wt% of MXene in between rGO sheets, the characteristic peak of rGO at 24.5° becomes non-prominent, however, the (000 l) peaks originated from MXene become dominant. But comparing to pure MXene films, the peaks are weak and shifted to lower 2θ angles, as a result of an increase in the c lattice parameter (c -LP) from 23 Å to 28 Å.

In order to qualify as efficient textile fibers, the mechanical performance of individual fiber is critical for textile processing and ultimate application. The typical stress-strain curve (Figure 4.4e) of rGO&MXene fibers, like other wrinkled graphene-based films,²³⁶ exhibits three regions of deformation: straightening region (I), almost linear elastic region (II), and followed by a yield point and a region of plastic deformation (III). Firstly, the high level of wrinkling and waviness of 2D sheets in the rGO&MXene fibers at various length scales are being extended. As the flattening continued, the wrinkles stored strain energy was released, partially canceling out the increment of strain energy that from the stretching of interaction among rGO and MXene sheets, therefore,

resulting in a lower modulus.²³⁷ After the sheets were effectively unfolded and aligned along fiber axis, a noticeable increase in modulus was observed and the elastic deformation became dominant in the second region due to the stretching of the interaction among rGO and MXene sheets. As the strain keep increasing, until the yield point at which the stress is enough to break the interaction, rGO and MXene sheets shear with each other under modest tensile stress, dissipating energy through viscous friction. By comparison, pure rGO fibers contain more flattened rGO sheets that interlocked/tiled in a near-parallel fashion, resulting in mostly linear behavior upon stretching. rGO sheets are stacked at a more compact structure in rGO fibers, resulting in more uniform and strong interaction among each other. These allow for a highly effective load distribution across the entire macroscopic fibers, resulting in higher tensile strength. Because of the heterostructure of rGO&MXene fibers, they are much porous and less-ordered through the cross-sectional direction, leading to more grain boundaries. In addition, interlayer interaction among rGO sheets and MXene sheets are less uniform as comparing to the interaction among pure rGO sheets, interrupting the stress transfer. Therefore, the rGO&MXene fibers have lower tensile strength.

We have also evaluated the electrochemical performance of rGO&MXene fibers and compared with rGO fibers by assembling them into FSCs with PVA-H₂SO₄ electrolyte, respectively. As expected, FSCs from rGO&MXene fibers showed much larger capacitance (342.59 mF cm⁻²) (Figure 4.6a & c), seventeen times higher than that of FSCs from pure rGO fibers (19.16 mF cm⁻²). The improved capacitance mainly originated from the pseudocapacitive performance of MXene and the wrinkled surface morphology of rGO&MXene fibers. In addition, electrochemical impedance spectroscopy (EIS) test was applied to evaluate the equivalent series resistance (ESR) of these two systems. Figure 4.6b shows the Nyquist plots with frequency from 0.01 Hz to 0.1 MHz with amplitude of 10 mV. Due to the high electrical conductivity of

rGO&MXene fibers and better capacitive performance, its corresponding FSCs exhibit seven times lower ESR ($0.58\text{ k}\Omega$) than that of rGO FSCs ($4.35\text{ k}\Omega$), suggesting the potential to deliver high power.

It is worth noting that although capacitive performance of rGO&MXene fiber demonstrates an extent to which performance of fiber electrodes can be improved, the electrolyte diffusion is still limited at the fiber electrode and electrolyte interface. We address realization of the enhanced electrochemical performance in the sections below.

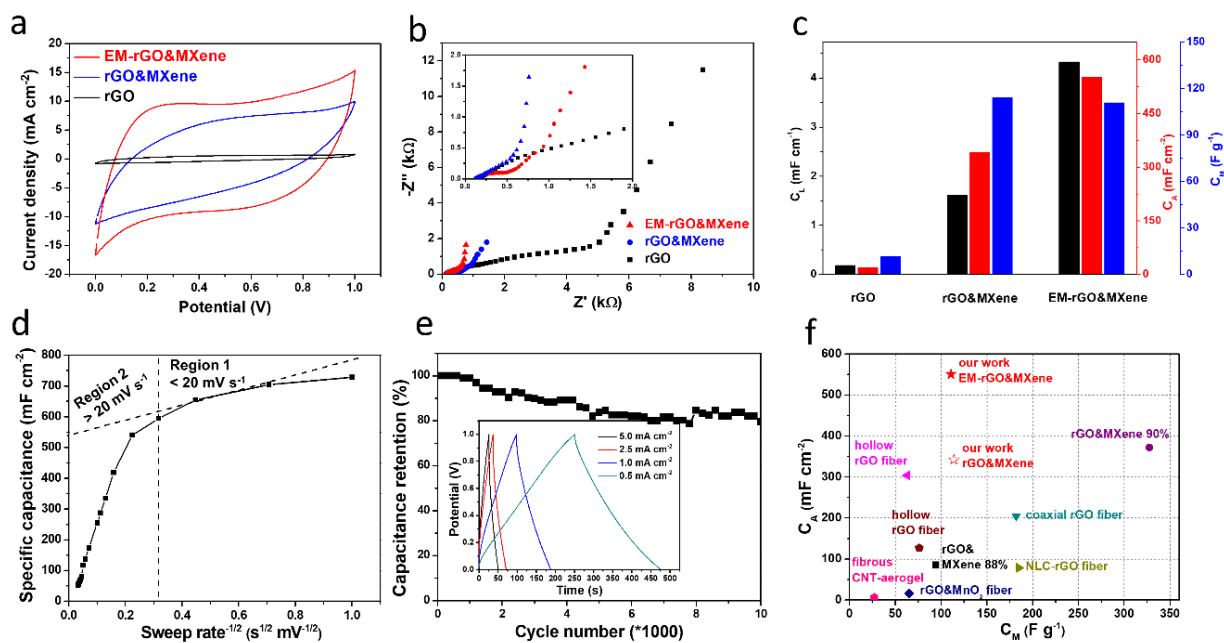


Figure 4.6 Electrochemical performance of FSCs. (a, b) CV curves at 20 mV s^{-1} (a) and Nyquist plots (b) of rGO FSCs, rGO&MXene FSCs and EM-rGO&MXene FSCs. (c) Linear, areal and gravimetric capacitance of rGO fibers, rGO&MXene fibers and EM-rGO&MXene fibers. (d) A plot of C_A versus $v^{-1/2}$, indicating the separation of diffusion-controlled capacitance from capacitive-controlled capacitance. (e) Capacitance retention of the EM-rGO&MXene FSCs performed by galvanostatic cycling at 5 mA cm^{-2} . The inset depicts galvanostatic cycling profiles collected at different current density. (f) Comparison of the areal and gravimetric capacitance of EM-rGO&MXene fiber electrode with other reported fiber electrodes, including hollow rGO fibers,²³⁸⁻²³⁹ non-LC wet-spun rGO fiber,¹¹⁸ rGO&MnO₂ fiber,²¹⁷ fibrous CNT aerogel,¹⁰ rGO&MXene (88%) fibers,²²² and rGO&MXene (90%) fibers.²²³

4.3.2. Electrolyte Mediated Fiber Electrodes for High Capacitive Performance

In order to reduce the interface resistance at the electrode/electrolyte interface, as well as improve the diffusion of electrolyte and the utilization of fiber electrodes with compact layered rGO and MXene sheets, we pre-incorporated the non-volatile liquid (H_2SO_4) into small-size

channels in between the layered structure through electrolyte mediation (EM), forming highly compact EM-rGO&MXene fiber electrodes with a continuous ion transport network (Figure 4.7). This help ions in accessing the interplanar space rather than stay at the fiber surface. This approach was previously used to enhance performance of graphene films in aqueous electrolytes²⁴⁰ and also to enable access of bulky ionic liquid ions to electrochemically active sites of MXene.^{221, 241}

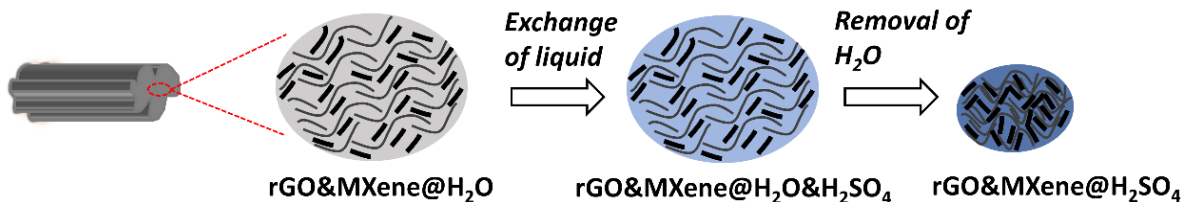


Figure 4.7 Schematic illustration of EM-rGO&MXene fibers preparation procedure.

After electrolyte incorporation, the diameter of fibers was increased from $\sim 30 \mu m$ of dry rGO&MXene fibers to $\sim 50 \mu m$ of EM-rGO&MXene fibers (Figure 4.4b), with linear density increasing from 2.8 g/km to 7.8 g/km (including the mass of electrolyte incorporated). The trapped nonvolatile liquids in between rGO and MXene layers make the wrinkles smooth away, resulting in less wrinkled surface morphology (Figure 4.4b). Raman spectroscopy (Figure 4.4c) showed similar characteristic peaks that originate from MXene and rGO as comparing to rGO&MXene fibers. XRD analysis (Figure 4.4d) showed the EM-rGO&MXene fibers displayed a nearly amorphous structure. Only small and broad peak at 6.4° , corresponding to a c -LP of 27\AA . This indicated that the majority of rGO and MXene sheets do not restack compact. Upon stretching, the electrolyte working as sliding agents, rGO and MXene sheets can slip past each other, dissipating energy through viscous friction, resulting in 28 % lower tensile strength but 24 % larger elongation (Figure 4.4e), as comparing to rGO&MXene fibers. As expected, a single linear stress-strain relationship was observed, indicating good homogeneity and elasticity of the EM-rGO&MXene fibers. In addition, they can be tied into tight knot, exhibiting good bending stability.

Due to the pre-incorporated electrolyte, the CV curve of FSC from EM-rGO&MXene fibers showed quasi-rectangular shape rather than a more fusiform shape displayed by the rGO&MXene FSC (Figure 4.6a), indicating better diffusion of electrolyte in EM-rGO&MXene FSCs. The EIS analysis was also performed to further ascertain the role of the pre-incorporated electrolyte (Figure 4.6b). The plot of EM-rGO&MXene FSC featured a more vertical curve at low frequency, indicating a better capacitive behavior. At high-frequency regions, it also presented a shorter Warburg region followed by a small semicircle, indicating better diffusion of electrolyte. The above results show that pre-incorporation of electrolytes in the EM-rGO&MXene fibers ensures better electrolyte accessibility, resulting in larger capacitance and lower ESR. FSCs from EM-rGO&MXene fibers possess larger areal and linear capacitance ($550.96 \text{ mF cm}^{-2}$, 4.4 mF cm^{-1}), 1.6 times 2.6 times higher than that of rGO&MXene FSCs (Figure 4.6c), respectively, due to the higher utilization of inner layers of rGO and MXene. However, due to the increase of linear density, the gravimetric capacitance of EM-rGO&MXene fibers is $\sim 3\%$ lower than that of rGO&MXene fibers. In addition, as the electrolyte became integrated within the fibers from the start of the preparation process, there was no subsequent wettability issue for these EM-rGO&MXene fibers, which remained a serious problem for the dried rGO based fibers (Figure 4.8).^{193, 214}

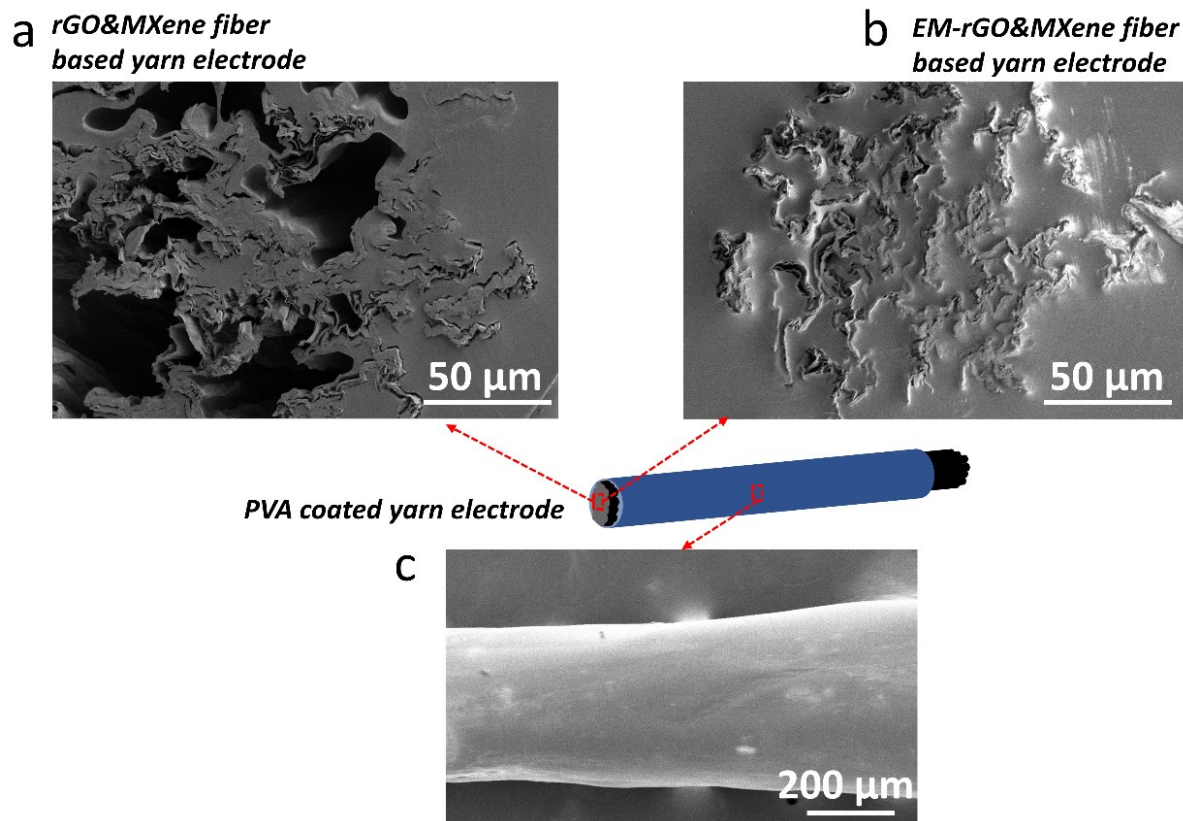


Figure 4.8 SEM images of cross-sectional PVA coated yarn electrode. (a) Cross-sectional SEM image of rGO&MXene fiber based yarn electrode; (b) Cross-sectional SEM image of EM-rGO&MXene fiber based yarn electrode. (c) Surface SEM image of PVA based electrolyte coated yarn electrode.

In order to investigate the nature of the charge storage process, the electrochemical kinetics of EM-rGO&MXene FSCs were evaluated. The relationship between capacitance and scan rate can establish the rate-limiting step of a charge-storage mechanism. In a plot of C versus $\nu^{-1/2}$, regions that are linear represent capacitance limited by semi-infinite linear diffusion whereas capacitance contributions are independent of the scan rate. At scan rate below 20 mV s^{-1} , the extrapolated y-intercept yields the infinite scan rate capacitance. Figure 4.6d shows the plot of normalized capacitance versus $\nu^{-1/2}$ for EM-rGO&MXene FSC from 1 to 500 mV s^{-1} , which can be divided into two regions. In the region at scan rate $< 20 \text{ mV s}^{-1}$ (charging times larger than 50

s), the capacitance is mostly independent of scan rate, since the electrolyte diffusion is not the rate-limiting step for charge storage. There is no indication of diffusion limitations and this intercalation-based system behaves in a fully capacitive manner. However, as increasing scan rate from 40 to 500 mV s⁻¹, the capacitance decreases linearly with $v^{-1/2}$. This indicates that charge storage is mainly diffusion-controlled at high scan rates with charging time < 25 s. At such short charging period, diffusion is limited, and the response is due to surface capacitive effects, whether electrostatic or pseudocapacitive. This behavior is similar to most traditional pseudocapacitive and battery electrodes.

The long-term cycling stability of EM-rGO&MXene FSCs was evaluated by repeating the GAL test at current density of 5 mA cm⁻² for 10,000 cycles. The FSCs exhibits good cycling stability with 15 % deteriorate after 10, 000 cycles (Figure 4.6e). Furtherly, both areal and gravimetric capacitances of EM-rGO&MXene fiber electrodes were evaluated by comparing with some reported typical carbon-based fiber electrodes (Figure 4.6f). The capacitance of single fiber electrode in a two-electrode cell with PVA/H₂SO₄ electrolyte was measured to be 550.96 mF cm⁻² and 110.89 F g⁻¹ at 20 mV s⁻¹, respectively. It outperforms most of the pure carbonaceous materials-based fiber electrodes, such as hollow structured rGO fibers (304.5 mF cm⁻² and 63.1 F g⁻¹ at 0.08 mA cm⁻², 2-181 127.4 mF cm⁻² and 76.1 F g⁻¹ at 1 A g⁻¹),²³⁸ coaxial rGO fibers (205 mF cm⁻² and 182 F g⁻¹ at 10 mV s⁻¹),¹³⁹ non-LC (NLC) wet-spun rGO fibers with large surface area (78.7 mF cm⁻² and 185 F g⁻¹ at 0.2 A g⁻¹),¹¹⁸ fibrous CNT aerogel (6.9 mF cm⁻² and 27.3 F g⁻¹ at 0.1 mA).¹⁰ It is also superior to that with pseudocapacitive materials, such as rGO&MnO₂ fibers (16.7 mF cm⁻² and 65 F g⁻¹ at 0.05 mA cm⁻²),²¹⁷ rGO&MXene (88%) fibers (85.5 mF cm⁻² and 94.4 F g⁻¹ at 6.83 mA cm⁻²).²²² Yang *et al.*²²³ reported higher capacitance (372.2 mF cm⁻² and 327.5 F g⁻¹ at 10 mV s⁻¹) of rGO&MXene fibers with larger amount (90 wt %) of MXene incorporated,

but this will largely compromise the mechanical performance (~ 12.9 MPa in strength, $\sim 87\%$ weaker) of the ultimate fiber electrodes, making them difficult for subsequent textile processing.

EM-rGO&MXene fibers with electrolyte pre-incorporated in between layers show reasonable strength and flexibility. Also, with improved electrolyte accessibility, EM-rGO&MXene fiber electrodes possess high capacitance, good rate capability, rendering them a good candidate for further processing into YSCs.

4.3.3. Assemble YSCs Towards Real Energy Storage Application

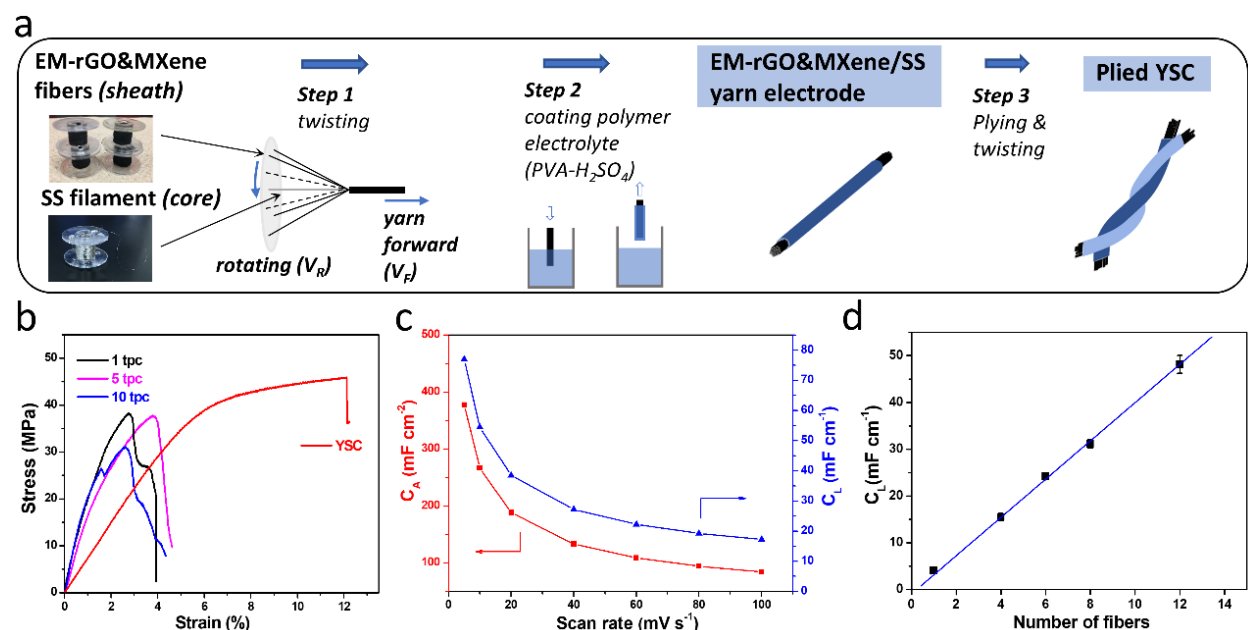


Figure 4.9 Fabrication and electrochemical performance of EM-rGO&MXene YSCs. (a) Schematic illustration of YSC fabrication process. (b) Typical stress-strain curves of yarn electrodes (with various degree of twists) and YSCs. (c) Areal and linear capacitance of EM-rGO&MXene YSCs at different scan rates. (d) Correlation between the linear capacitance of YSCs and the number of EM-rGO&MXene fibers incorporated.

To fully establish the real application of 1D energy storage devices, they are supposed to be processed into fabrics through textile techniques, such as weaving or knitting. In textile

industry, yarns which are the continuous strands of staple fibers (spun yarn) or filaments (filament yarn, either monofilament or multifilament), are usually the suitable form to be processed into fabrics.²⁴² Filament yarns are assembled from multifilaments, by simply grouping filaments together, insert twist in single strand, or multiple strands (plied yarns), to meet desired performance requirement. Multifilament yarns are stronger, more flexible, and more uniform compared to spun yarns. Due to the continuity of the filaments, their yarns can be produced in very low linear density. Spun yarns must have much more number of fibers, which are twisted together, in the cross section since their integrity relay on the inter-fiber-friction resulting in higher linear density. Here, in order to ensure the successful fabrication and function of rGO fibers based energy storage fabric, we adopted twisted filament yarns as our fundamental structure for yarn electrodes.

Yarn properties are defined by individual filament from which they are made and yarn structure which is the result of the yarn twisting conditions.²⁴³ In consideration of the composition of yarn electrodes, EM-rGO&MXene filaments are working as electrochemical active materials. In addition, in order to ensure good electron transfer inside yarn electrodes, stainless steel (SS) filaments are incorporated as current collectors. Regarding the yarn structure, to ensure good contact between each EM-rGO&MXene filaments with SS filaments, as well as the fully usage of each EM-rGO&MXene filament as active material, we chose compound yarn structure which has SS filament as core and EM-rGO&MXene filaments covering outside. The SS filaments are with diameter of 60 μm . The two kinds of filaments were assembled together by inserting twists to form compound multifilament yarn (EM-rGO&MXene & SS yarn). The amount of inserted twist in turns per centimeter (tpc) can be tuned by controlling the rotational speed (V_R) and yarn linear speed (V_F) in fabrication process (Figure 4.9a step 1). We studied the influence of twist on the mechanical properties of the compound yarns. Yarns with different levels of twist (1 tpc

(negligible), 5 tpc (low) and 10 tpc (moderate)) were fabricated, respectively. Figure 4.9b shows the typical stress-strain curves of EM-rGO&MXene & SS compound yarn with three levels of twist. The yarn with low twist level (5 tpc) exhibited comparable strength but higher breaking strain and toughness as compared to that of negligible twist level yarn (1 tpc). As the twist level increases furtherly to tpc of 10, the strength decreases obviously, due to filament obliquity to the yarn axis. This demonstrates that low twist level is reasonable for the mechanical properties of EM-rGO&MXene & SS compound yarn. Then, compound yarn was coated with PVA-H₂SO₄ electrolyte to get what we refer to as single yarn electrode (Figure 4.9a step 2). Two such single yarn electrodes were then plied together to get ultimate YSCs (Figure 4.9a step 3). We tested the electrochemical performance of the YSCs with eight EM-rGO&MXene filaments incorporated in one yarn electrode. Figure 4.10a shows the CV curves of the YSC at scanning rates ranging from 10 mV s⁻¹ to 100 mV s⁻¹. At low scan rate, it exhibits good quasi-rectangular shape. As scan rate increases to 100 mV s⁻¹, it turns to fusiform shape as observed in most YSCs, due to the insufficient ionic transport in the solid electrolyte during the charge/discharge process. The galvanostatic charge-discharge (GCD) curves at different current densities (Figure 4.10b) exhibits triangular shapes with a columbic efficiency of *ca.* 90%, suggesting good reversibility of the FSC and good charge propagation between the two yarn electrodes. Specific capacitances normalized to area (C_A) and length (C_L) of the YSC were calculated using CV curves at different scan rates (Figure 4.9c). With eight EM-rGO&MXene filaments, the capacitance of YSC can reach 32.5 mF cm⁻¹ (188.6 mF cm⁻²@ 20 mV s⁻¹), which is among the highest reported values. The overall capacitance of the assembled YSCs increases linearly with the number of EM-rGO&MXene filaments incorporated (Figure 4.9d), showing good scalability of our YSCs. The ultimate assembled YSC with eight EM-rGO&MXene filaments incorporated has a diameter of ~600 μm. Comparing to other scalable

YSCs with comparable thickness reported in literature, our YSCs are superior in linear capacitance. For example, Zhai *et al.* fabricated a hybrid carbon yarn including carbon fiber as current collector and deposited activated carbon as active material, exhibiting a capacitance of $\sim 14.3 \text{ mF cm}^{-1}$ (@ CV, 20 mV s^{-1}) with the diameter of the final YSC $> 1 \text{ mm}$.²⁴⁴ Jost *et al.* applied cotton fiber and SS plied yarn as current collector and substrate for welding activated carbon.²⁰² The resulted two yarn electrodes with diameter of $\sim 500 \mu\text{m}$ each were assembled into supercapacitor in a parallel structure ($\sim 1 \text{ mm}$ in diameter), exhibiting a capacitance of 13.1 mF cm^{-1} (@ CV, 20 mV s^{-1}). Our YSC has a capacitance of 49.8 mF cm^{-1} (@ CV, 20 mV s^{-1}) at the same diameter ($\sim 1 \text{ mm}$) when twelve EM-rGO&MXene filaments were incorporated in each electrode (Figure 4.9d).

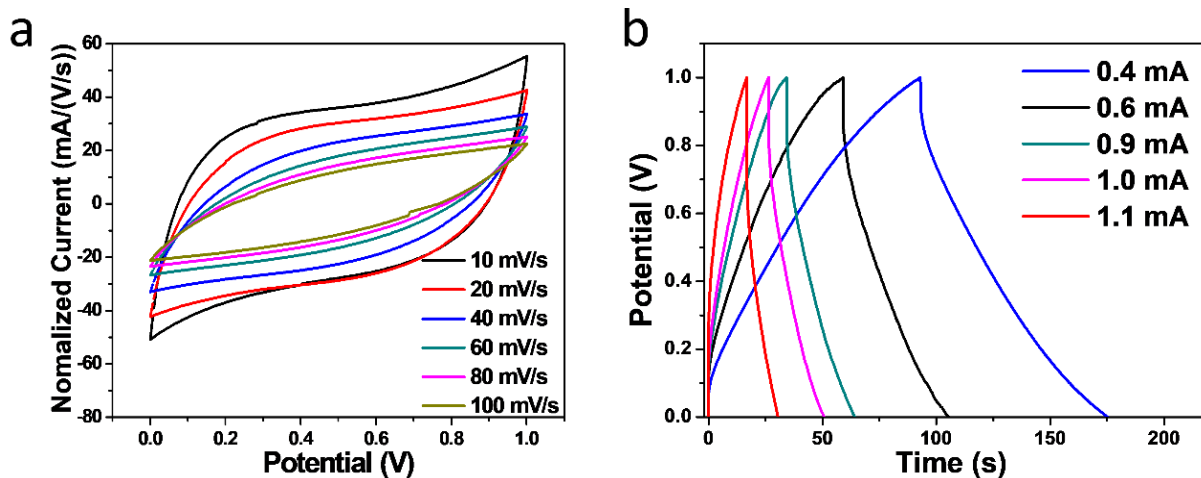


Figure 4.10 (a) CV curves of YSC at different scan rates from 5 mV s^{-1} to 100 mV s^{-1} . (b) GAL charge-discharge curve of YSC at different current.

After coating polymer electrolyte, filaments are bound together to prevent separation and entanglement, and to prevent individual filament breakage from peeling back along its length. Filaments are well integrated and as such they withstand mechanical complex field of stresses (abrasion, tension, bending, and impact) that they experience during integrating them into knitted or woven structures (Figure 4.9b). From the standpoints of large-scale manufacturing, other

advantages of polymer electrolyte coating include improving smoothness of yarn electrodes and YSC (Figure 4.8c). Since yarns are in contact with other yarns and various machine parts, such as the web roller, drop wires, heddle wires and reed wires in weaving process low friction that benefit from smoothness of yarns are good for the efficient production.²⁴⁵ Furthermore, since carbon-based fiber dusts may cause shorting or arcing in power distribution lines and other electrical equipment, the coated insulator layer do not pose such issue.²⁴⁶

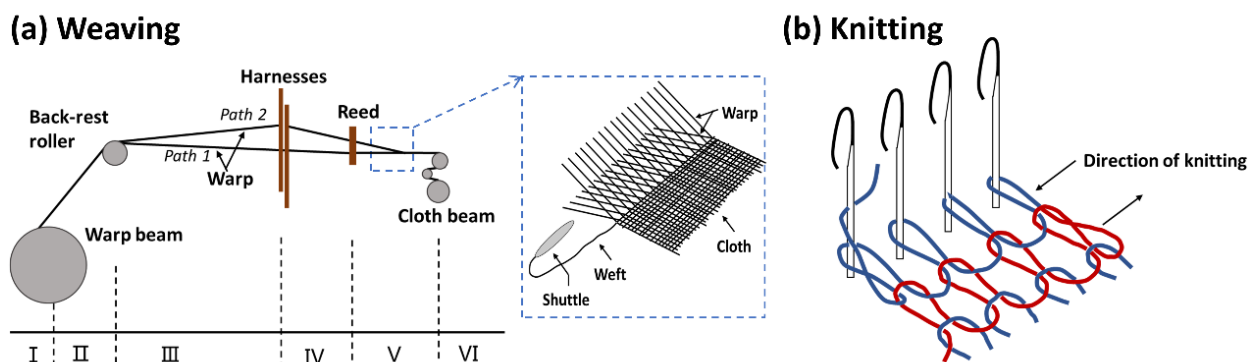


Figure 4.11 (a) Schematic illustration of the warp distribution per-segments on the loom. (b) Schematic illustration of the loop formation in knitting process.

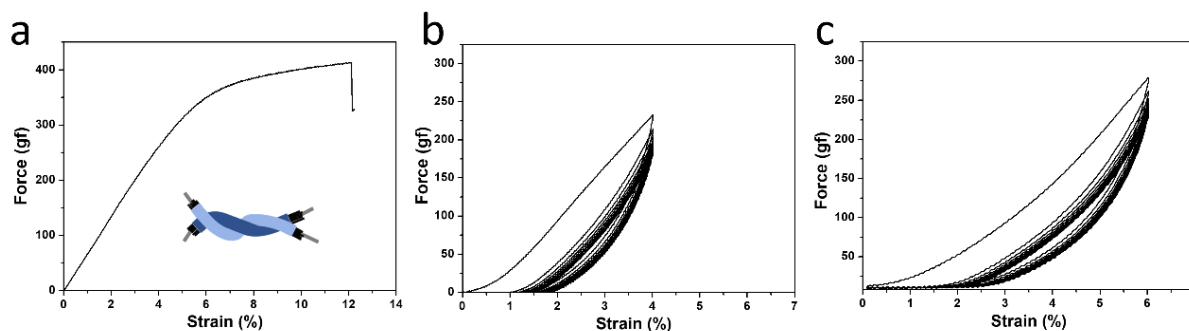


Figure 4.12 (a) Typical load-strain curve of YSCs. (b) Cycling stress-strain curves of EM-rGO&MXene YSCs with 4% (b) and 6% (c) elongation, respectively.

Weaving and knitting are the two foremost textile techniques for manufacturing fabrics. The weaving process converts two perpendicular sets of yarns namely warp and weft threads, by interlacing them according to desired weave design (Figure 4.11a). The ability of yarns to

successfully withstand the stresses imposed is an important determinant of operating efficiency. The criteria for evaluation warp yarns include the tensile strength, elongation at break and cyclic stability under constant strain/stress to simulate what the yarns are experiencing during weaving. Generally, the warp yarns are subjected to various conditions of cyclic extension as it travels from loom beam to the woven fabric (Figure 4.11a). From the typical stress-strain curve of one YSC (Figure 4.9b), we can see that the plastic deformation reaches 6% strain. Depending on weaving parameters and woven fabric structure, the strain levels during processing can be calculated through warp yarns pathways.²⁴⁷ Generally, its extension can be controlled at less than 4%. Thus, we evaluated the loading-unloading cyclic performance by setting the elongation to 4%. It can be seen from Figure 4.12b that there was a permanent strain (about 1%) in the first cycle but remained almost constant with further loading-unloading cycles. This occurrence of plasticity of first cycle can be explained by the yarn structure, where the fibers within the yarn are rearranged under the action of stretching. We also evaluated cyclic stability of yarns upon stretching to 6% for 10 cycles. The YSC can also maintain good cyclability. In knitting, the yarns are knit together by interloping (Figure 4.11b). Besides tensile strength and frictional properties, the knittability of a yarn also depends on its bending ability.²⁴⁸ Here, we demonstrated it can be hand-knitted into fabric as seen in Figure 4.13.



Figure 4.13 Optical image of hand knitted fabrics from EM-rGO&MXene fibers based YSCs.

Weaving and knitting have various requirements on yarns. Comparing to other YSCs that made from coating, one advantage of our yarn is that it is flexible to be designed into different

structures and properties, enabling them to be manufactured into various woven or knitted fabrics. For example, by incorporating different numbers of filaments into one yarn electrode, we can get ultimate YSC with different thickness and achieve required level of tensile strength, flexibility and capacitance *etc.* It is also possible to fabricate individual EM-rGO&MXene filaments with various diameter by modifying wet-spinning parameters and electrolyte mediation conditions. In addition, the SS filaments can be replaced with SS spun yarn and the multifilament yarn structure with numerous variations if so desired based on target performance requirements (energy-storage capacity and mechanical properties) dictated by the weaving/knitting process and the final performance of the resultant woven/knitted fabric.

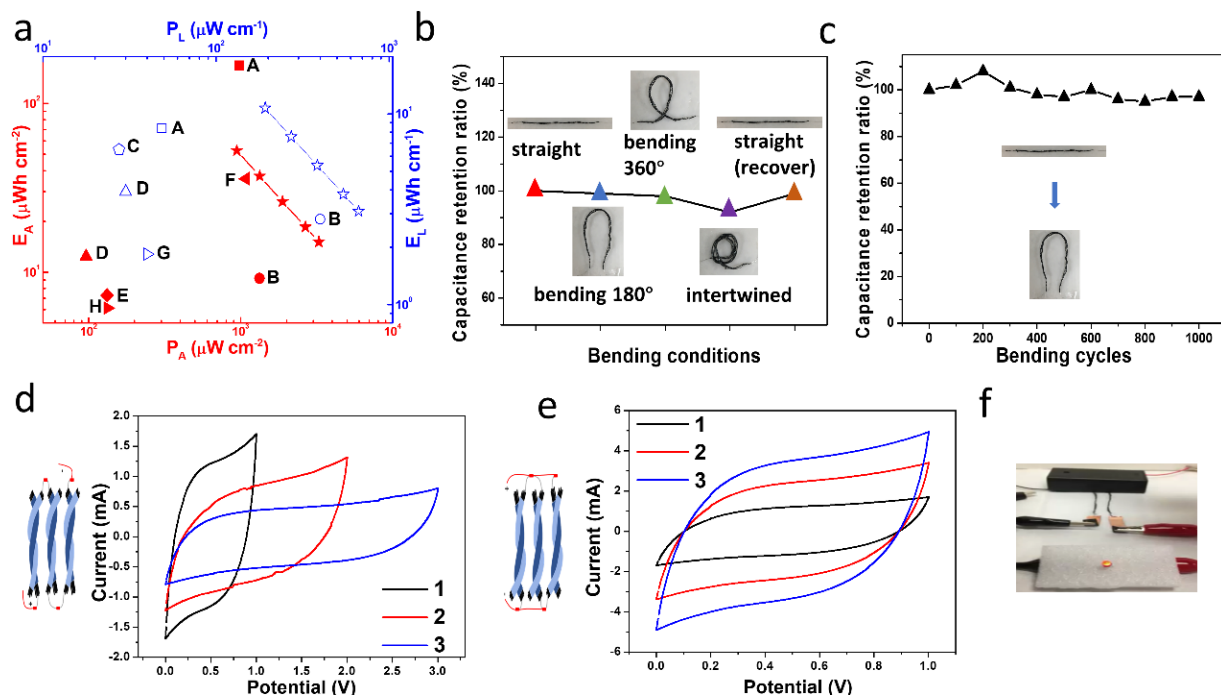


Figure 4.14 (a) Ragone plot of areal (filled red) and linear (unfilled blue) energy density versus power density of EM-rGO&MXene YSCs and some reported YSCs: (A) biscrolled MXene@CNT/RuO₂@CNT asymmetric YSC;²⁴⁹ (B) MnO₂/PPY/rGO@SSY YSC;²⁵⁰ (C) AC@CF YSC;²⁴⁴ (D) NiCoO₂@SSY YSC;²⁵¹ (E) MXene/Ag@Nylon YSC;²²⁴ (F) MnO₂@CNT YSC;¹¹ (G) PPY/CNT@PU/Cotton YSC.²⁵² (b) Capacitance retention of YSC in different bending conditions. Inset: optical images of YSCs in different bending conditions. (c) Capacitance retention at different bending cycles with bending angle of 180°. (d) Schematic illustration of three YSCs in series and CV curves of single, two and three YSCs in series. (e) Schematic illustration of three YSCs in parallel and CV curves of single, two and three YSCs in parallel. (f) Optical image of a red LED powered by two charged YSCs connected in series.

The Ragone plot is a meaningful way to evaluate the energy storage performance of SCs comprehensively. Figure 4.14a demonstrated the excellent both areal and linear energy and power densities of the YSCs compared to literature reports. These values were calculated on the basis of

the total surface area of the YSCs, including coated gel electrolyte. The YSCs deliver an areal energy density of $52.4 \mu\text{Wh cm}^{-2}$ at a power density of $943.2 \mu\text{W cm}^{-2}$ ($10.7 \mu\text{Wh cm}^{-1}$ at $192.5 \mu\text{W cm}^{-1}$). Even at a higher power density of $3267.7 \mu\text{W cm}^{-2}$, the YSC has an energy density of $15.13 \mu\text{Wh cm}^{-2}$ ($3.1 \mu\text{Wh cm}^{-1}$ at $666.9 \mu\text{W cm}^{-1}$). Our YSCs outperformed most of the previously reported YSCs, which were all made from coated yarn electrodes. We also summarized the related YSCs performance values along with the employed fabrication methods, active electrode materials in Table 4.1.

In order to simulate wearing conditions, we also measured the bending stability of the YSCs. Figure 4.14b shows the capacitance retention of the YSC under different bending conditions as illustrated in the inset photos. The capacitance retention was tested by CV at 20 mV s^{-1} and it exhibited less than 5% fluctuation during most of the bending conditions and only exhibited a small decrease ($< 10\%$) when the whole device was intertwined. In addition, it also retained 90% after 1,000 bending cycles (Figure 4.14c), demonstrating excellent flexibility and bending stability of the YSCs.

The single YSC show good electrochemical performance, which makes it promising for wearable electronics. However, the current and potential range offered by a single YSC fail to meet the power and energy requirement of practical electronics. This issue can be well resolved by connecting YSCs in series, or in parallel. Compared with the single YSC that operates at 1 V, three YSCs connected in series (Figure 4.14d) exhibited a 3-V voltage window. In the parallel assembly (Figure 4.14e), the output current was increased by a factor of the number of YSCs that connected in parallel with the same voltage window of 0 to 1 V. The serially connected YSCs can be readily used to power up a light-emitting diode (LED) that operates at a minimum voltage of 1.7 V. The YSCs can be charged by a conventional battery, and then provide adequate energy to

light up the LED. For example, the two 2.5-cm-long YSCs connected in series (Figure 4.14f) were able to power up a red LED for > 40 s.

Table 4.1 Comparison of the fabrication method, specific capacitance, energy density and power density of various YSCs.

Material	Fabrication method	C _A (mF cm ⁻²)	C _L (mF cm ⁻¹)	C _V (F cm ⁻³)	E _A (μWh cm ⁻²)	P _A (μW cm ⁻²)	E _L (μWh cm ⁻¹)	P _L (μW cm ⁻¹)	Test condition
MXene@CNT/RuO ₂ @CNT ²⁴⁹	biscrolling	554	27.8	203	168	975	8.4	48.8	2 mA cm ⁻²
MnO ₂ /PPY/rGO@SSY ²⁵⁰	electrodeposition	411	31	68.52	9.2	1330	2.8	400	11 mA cm ⁻³
AC@CF ²⁴⁴	drop-casting		14.3				6.5	27.5	20 mV s ⁻¹
MXene/PEDOT:PSS@CF ²⁵³	coating	658.5	126.3	54.7					2 mV s ⁻¹
MoO ₃ /CNT/NiCo ₂ O ₄ @PET ²²⁵	hydrothermal			28.8					0.17 A cm ⁻³
rGO/Ni@Cotton yarn ¹⁹²	electrodeposition		110		68.2				
AC/SS@Cotton yarn ²⁰²	weld		13.1						20 mV s ⁻¹
Ni-Co oxides@SSY ²⁵¹	hydrothermal	69.01	21.67		12.4-8.5	90-430	3.9	134	0.06 mA cm ⁻¹
PPY@SSY ²⁵⁴	electropolymerization	586.8	101.5	42.7	52.2	5340	9.02	920	0.21 A cm ⁻³
MXene/Ag@Nylon yarn ²²⁴	drop-casting	328	50		7.3	132			2 mV s ⁻¹
NiCoO ₂ @CF ²²⁶	hydrothermal		1.68						0.05 mA cm ⁻¹
MnO ₂ @CNT yarn ¹¹	biscrolling	888.7	60.6	154.7	35.8	1080			2 mA cm ⁻²
PPY/CNT@PU/Cotton ²⁵²	drop-casting		20.68		6.13	133	1.84	40	
rGO/MXene fiber/SS yarn (our work)	wet-spinning	1089.88*	154*	96.88*					5 mV s ⁻¹
		377.3	77	23.2	26.2	1886	5.3	385	

Note: * values were normalized to single electrode, otherwise, normalized to YSC device.

CNT is short for carbon nanotube; SSY is short for stainless steel yarn; AC is short for activated carbon; CF is short for carbon fiber.

4.4. Conclusion

In summary, we have demonstrated how individual graphene-based functional fibers can be fabricated into high-performance YSCs for real applications *via*. textile manufacturing processes. With 60 wt % MXene incorporated, rGO&MXene fibers possess balanced mechanical properties and electrical conductivity. Also, rGO&MXene FSCs show capacitance of 342.59 mF cm⁻², seventeen times higher than that of FSC from pure rGO fibers (19.16 mF cm⁻²). In addition, EM-rGO&MXene fibers with H₂SO₄ incorporated, demonstrated good wettability and excellent capacitance up to 550.96 mF cm⁻², exceeding most of state-of-the-art fiber electrodes. EM-rGO&MXene fibers can be furtherly twisted into yarn electrodes, followed by electrolyte engineering to get YSCs. Our YSCs show good capacitive performance, with energy density of 52.4 μWh cm⁻² at a power density of 943.2 μW cm⁻². It also exhibits good bending stability upon thousands of bending cycles and various bending angles. This study also indicated that MXene is an effective material for high-performance fiber electrodes in YSCs. Importantly, through our findings here, we confirm that the individual functional fibers are the proper units to be assembled into YSCs for the real wearable energy-storage fabrics.

REFERENCES

1. Xu, Z.; Gao, C., Aqueous Liquid Crystals of Graphene Oxide. *Acs Nano* 2011, 5 (4), 2908-2915.
2. Xu, Z.; Gao, C., Graphene chiral liquid crystals and macroscopic assembled fibres. *Nat Commun* 2011, 2.
3. Xu, Z.; Liu, Z.; Sun, H.; Gao, C., Highly Electrically Conductive Ag-Doped Graphene Fibers as Stretchable Conductors. *Adv Mater* 2013, 25 (23), 3249-3253.
4. Aboutalebi, S. H.; Jalili, R.; Esrafilzadeh, D.; Salari, M.; Gholamvand, Z.; Aminorroaya Yamini, S.; Konstantinov, K.; Shepherd, R. L.; Chen, J.; Moulton, S. E.; Innis, P. C.; Minett, A. I.; Razal, J. M.; Wallace, G. G., High-Performance Multifunctional Graphene Yarns: Toward Wearable All-Carbon Energy Storage Textiles. *ACS Nano* 2014, 8 (3), 2456-2466.
5. Yu, D.; Qian, Q.; Wei, L.; Jiang, W.; Goh, K.; Wei, J.; Zhang, J.; Chen, Y., Emergence of fiber supercapacitors. *Chem Soc Rev* 2015, 44 (3), 647-662.
6. Zhao, X.; Zheng, B.; Huang, T.; Gao, C., Graphene-based single fiber supercapacitor with a coaxial structure. *Nanoscale* 2015, 7 (21), 9399-9404.
7. El-Kady, M. F.; Strong, V.; Dubin, S.; Kaner, R. B., Laser Scribing of High-Performance and Flexible Graphene-Based Electrochemical Capacitors. *Science* 2012, 335 (6074), 1326-1330.
8. Zheng, X.; Zhang, K.; Yao, L.; Qiu, Y.; Wang, S., Hierarchically porous sheath-core graphene-based fiber-shaped supercapacitors with high energy density. *J Mater Chem A* 2018, 6 (3), 896-907.
9. He, N.; Pan, Q.; Liu, Y.; Gao, W., Graphene-Fiber-Based Supercapacitors Favor N-Methyl-2-pyrrolidone/Ethyl Acetate as the Spinning Solvent/Coagulant Combination. *ACS Applied Materials & Interfaces* 2017.

10. Li, Y.; Kang, Z.; Yan, X. Q.; Cao, S. Y.; Li, M. H.; Guo, Y.; Huan, Y. H.; Wen, X. S.; Zhang, Y., A three-dimensional reticulate CNT-aerogel for a high mechanical flexibility fiber supercapacitor. *Nanoscale* 2018, 10 (19), 9360-9368.
11. Choi, C.; Kim, K. M.; Kim, K. J.; Lepro, X.; Spinks, G. M.; Baughman, R. H.; Kim, S. J., Improvement of system capacitance via weavable superelastic bistructured yarn supercapacitors. *Nat Commun* 2016, 7.
12. Gao, W. Graphite oxide: Structure, reduction and applications. Rice University, 2012.
13. Gao, W.; Alemany, L. B.; Ci, L.; Ajayan, P. M., New insights into the structure and reduction of graphite oxide. *Nat Chem* 2009, 1, 403.
14. Narayan, R.; Kim, J. E.; Kim, J. Y.; Lee, K. E.; Kim, S. O., Graphene Oxide Liquid Crystals: Discovery, Evolution and Applications. *Adv Mater* 2016, 28 (16), 3045-3068.
15. Dreyer, D. R.; Park, S.; Bielawski, C. W.; Ruoff, R. S., The chemistry of graphene oxide. *Chem Soc Rev* 2010, 39 (1), 228-240.
16. Paredes, J. I.; Villar-Rodil, S.; Martinez-Alonso, A.; Tascon, J. M. D., Graphene oxide dispersions in organic solvents. *Langmuir* 2008, 24 (19), 10560-10564.
17. Loh, K. P.; Bao, Q.; Eda, G.; Chhowalla, M., Graphene oxide as a chemically tunable platform for optical applications. *Nat Chem* 2010, 2, 1015.
18. Novoselov, K. S.; Geim, A. K.; Morozov, S. V.; Jiang, D.; Zhang, Y.; Dubonos, S. V.; Grigorieva, I. V.; Firsov, A. A., Electric Field Effect in Atomically Thin Carbon Films. *Science* 2004, 306 (5696), 666-669.
19. Novoselov, K. S.; Geim, A. K.; Morozov, S. V.; Jiang, D.; Katsnelson, M. I.; Grigorieva, I. V.; Dubonos, S. V.; Firsov, A. A., Two-dimensional gas of massless Dirac fermions in graphene. *Nature* 2005, 438, 197.

20. Mattevi, C.; Eda, G.; Agnoli, S.; Miller, S.; Mkhoyan, K. A.; Celik, O.; Mastrogiovanni, D.; Granozzi, G.; Garfunkel, E.; Chhowalla, M., Evolution of Electrical, Chemical, and Structural Properties of Transparent and Conducting Chemically Derived Graphene Thin Films. *Adv Funct Mater* 2009, 19 (16), 2577-2583.
21. Erickson, K.; Erni, R.; Lee, Z.; Alem, N.; Gannett, W.; Zettl, A., Determination of the Local Chemical Structure of Graphene Oxide and Reduced Graphene Oxide. *Adv Mater* 2010, 22 (40), 4467-4472.
22. Li, J.; Li, J.; Li, L.; Yu, M.; Ma, H.; Zhang, B., Flexible graphene fibers prepared by chemical reduction-induced self-assembly. *J Mater Chem A* 2014, 2 (18), 6359-6362.
23. Cruz-Silva, R.; Morelos-Gomez, A.; Kim, H.-i.; Jang, H.-k.; Tristan, F.; Vega-Diaz, S.; Rajukumar, L. P.; Elías, A. L.; Perea-Lopez, N.; Suhr, J.; Endo, M.; Terrones, M., Superstretchable Graphene Oxide Macroscopic Fibers with Outstanding Knotability Fabricated by Dry Film Scrolling. *ACS Nano* 2014, 8 (6), 5959-5967.
24. Takajima, T.; Kajiwara, K.; McIntyre, J. E., *Advanced fiber spinning technology*. Woodhead Publishing: 1994.
25. Zhao, J. P.; Pei, S. F.; Ren, W. C.; Gao, L. B.; Cheng, H. M., Efficient Preparation of Large-Area Graphene Oxide Sheets for Transparent Conductive Films. *Acs Nano* 2010, 4 (9), 5245-5252.
26. Onsager, L., THE EFFECTS OF SHAPE ON THE INTERACTION OF COLLOIDAL PARTICLES. *Annals of the New York Academy of Sciences* 1949, 51 (4), 627-659.
27. Poulin, P.; Jalili, R.; Neri, W.; Nallet, F.; Divoux, T.; Colin, A.; Aboutalebi, S. H.; Wallace, G.; Zakri, C., Superflexibility of graphene oxide. *P Natl Acad Sci USA* 2016, 113 (40), 11088-11093.

28. Jalili, R.; Aboutalebi, S. H.; Esrafilzadeh, D.; Konstantinov, K.; Razal, J. M.; Moulton, S. E.; Wallace, G. G., Formation and processability of liquid crystalline dispersions of graphene oxide. *Materials Horizons* 2014, 1 (1), 87-91.
29. Kim, J. E.; Han, T. H.; Lee, S. H.; Kim, J. Y.; Ahn, C. W.; Yun, J. M.; Kim, S. O., Graphene Oxide Liquid Crystals. *Angewandte Chemie International Edition* 2011, 50 (13), 3043-3047.
30. Dan, B.; Behabtu, N.; Martinez, A.; Evans, J. S.; Kosynkin, D. V.; Tour, J. M.; Pasquali, M.; Smalyukh, I. I., Liquid crystals of aqueous, giant graphene oxide flakes. *Soft Matter* 2011, 7 (23), 11154-11159.
31. Aboutalebi, S. H.; Gudarzi, M. M.; Zheng, Q. B.; Kim, J.-K., Spontaneous Formation of Liquid Crystals in Ultralarge Graphene Oxide Dispersions. *Adv Funct Mater* 2011, 21 (15), 2978-2988.
32. van der Kooij, F. M.; Kassapidou, K.; Lekkerkerker, H. N. W., Liquid crystal phase transitions in suspensions of polydisperse plate-like particles. *Nature* 2000, 406, 868.
33. Yao, B.; Chen, J.; Huang, L.; Zhou, Q.; Shi, G., Base-Induced Liquid Crystals of Graphene Oxide for Preparing Elastic Graphene Foams with Long-Range Ordered Microstructures. *Adv Mater* 2016, 28 (8), 1623-1629.
34. Jalili, R.; Aboutalebi, S. H.; Esrafilzadeh, D.; Konstantinov, K.; Moulton, S. E.; Razal, J. M.; Wallace, G. G., Organic Solvent-Based Graphene Oxide Liquid Crystals: A Facile Route toward the Next Generation of Self-Assembled Layer-by-Layer Multifunctional 3D Architectures. *ACS Nano* 2013, 7 (5), 3981-3990.
35. Chhabra, R. P., Non-Newtonian fluids: an introduction. In *Rheology of complex fluids*, Springer: 2010, pp 3-34.
36. Yang, X.; Guo, C.; Ji, L.; Li, Y.; Tu, Y., Liquid Crystalline and Shear-Induced Properties of

- an Aqueous Solution of Graphene Oxide Sheets. *Langmuir* 2013, 29 (25), 8103-8107.
37. Hong, S.-H.; Shen, T.-Z.; Song, J.-K., Flow-induced ordering of particles and flow velocity profile transition in a tube flow of graphene oxide dispersions. *Liquid Crystals* 2015, 42 (2), 261-269.
 38. Naficy, S.; Jalili, R.; Aboutalebi, S. H.; Gorkin Iii, R. A.; Konstantinov, K.; Innis, P. C.; Spinks, G. M.; Poulin, P.; Wallace, G. G., Graphene oxide dispersions: tuning rheology to enable fabrication. *Materials Horizons* 2014, 1 (3), 326-331.
 39. Chen, D. T. N.; Wen, Q.; Janmey, P. A.; Crocker, J. C.; Yodh, A. G., Rheology of Soft Materials. *Annu Rev Condens Ma P* 2010, 1, 301-322.
 40. Jalili, R.; Aboutalebi, S. H.; Esrafilzadeh, D.; Shepherd, R. L.; Chen, J.; Aminorroaya-Yamini, S.; Konstantinov, K.; Minett, A. I.; Razal, J. M.; Wallace, G. G., Scalable One-Step Wet-Spinning of Graphene Fibers and Yarns from Liquid Crystalline Dispersions of Graphene Oxide: Towards Multifunctional Textiles. *Adv Funct Mater* 2013, 23 (43), 5345-5354.
 41. Xu, Z.; Sun, H.; Zhao, X.; Gao, C., Ultrastrong Fibers Assembled from Giant Graphene Oxide Sheets. *Adv Mater* 2013, 25 (2), 188-193.
 42. Gopalsamy, K.; Xu, Z.; Zheng, B.; Huang, T.; Kou, L.; Zhao, X.; Gao, C., Bismuth oxide nanotubes-graphene fiber-based flexible supercapacitors. *Nanoscale* 2014, 6 (15), 8595-8600.
 43. Liu, Z.; Xu, Z.; Hu, X.; Gao, C., Lyotropic Liquid Crystal of Polyacrylonitrile-Grafted Graphene Oxide and Its Assembled Continuous Strong Nacre-Mimetic Fibers. *Macromolecules* 2013, 46 (17), 6931-6941.
 44. Hu, X.; Xu, Z.; Liu, Z.; Gao, C., Liquid crystal self-templating approach to ultrastrong and

- tough biomimic composites. *Sci Rep-Uk* 2013, 3, 2374.
45. Zhao, X.; Xu, Z.; Zheng, B.; Gao, C., Macroscopic assembled, ultrastrong and H₂SO₄-resistant fibres of polymer-grafted graphene oxide. *Sci Rep-Uk* 2013, 3, 3164.
 46. Hu, X.; Xu, Z.; Gao, C., Multifunctional, supramolecular, continuous artificial nacre fibres. *Sci Rep-Uk* 2012, 2, 767.
 47. Xu, Z.; Gao, C., Graphene in Macroscopic Order: Liquid Crystals and Wet-Spun Fibers. *Accounts of Chemical Research* 2014, 47 (4), 1267-1276.
 48. Dong, Z.; Jiang, C.; Cheng, H.; Zhao, Y.; Shi, G.; Jiang, L.; Qu, L., Facile Fabrication of Light, Flexible and Multifunctional Graphene Fibers. *Adv Mater* 2012, 24 (14), 1856-1861.
 49. Hu, C.; Zhao, Y.; Cheng, H.; Wang, Y.; Dong, Z.; Jiang, C.; Zhai, X.; Jiang, L.; Qu, L., Graphene Microtubings: Controlled Fabrication and Site-Specific Functionalization. *Nano Letters* 2012, 12 (11), 5879-5884.
 50. Yu, D.; Goh, K.; Wang, H.; Wei, L.; Jiang, W.; Zhang, Q.; Dai, L.; Chen, Y., Scalable synthesis of hierarchically structured carbon nanotube–graphene fibres for capacitive energy storage. *Nat Nanotechnol* 2014, 9, 555.
 51. Liu, Z.; Li, Z.; Xu, Z.; Xia, Z.; Hu, X.; Kou, L.; Peng, L.; Wei, Y.; Gao, C., Wet-Spun Continuous Graphene Films. *Chemistry of Materials* 2014, 26 (23), 6786-6795.
 52. Hua, C.; Shang, Y.; Li, X.; Hu, X.; Wang, Y.; Wang, X.; Zhang, Y.; Li, X.; Duan, H.; Cao, A., Helical graphene oxide fibers as a stretchable sensor and an electrocapillary sucker. *Nanoscale* 2016, 8 (20), 10659-10668.
 53. Kou, L.; Huang, T.; Zheng, B.; Han, Y.; Zhao, X.; Gopalsamy, K.; Sun, H.; Gao, C., Coaxial wet-spun yarn supercapacitors for high-energy density and safe wearable electronics. *Nat Commun* 2014, 5, 3754.

54. Zhao, Y.; Jiang, C.; Hu, C.; Dong, Z.; Xue, J.; Meng, Y.; Zheng, N.; Chen, P.; Qu, L., Large-Scale Spinning Assembly of Neat, Morphology-Defined, Graphene-Based Hollow Fibers. *ACS Nano* 2013, 7 (3), 2406-2412.
55. Xu, Z.; Zhang, Y.; Li, P.; Gao, C., Strong, Conductive, Lightweight, Neat Graphene Aerogel Fibers with Aligned Pores. *ACS Nano* 2012, 6 (8), 7103-7113.
56. Lee, C.; Wei, X.; Kysar, J. W.; Hone, J., Measurement of the Elastic Properties and Intrinsic Strength of Monolayer Graphene. *Science* 2008, 321 (5887), 385-388.
57. Bolotin, K. I.; Sikes, K. J.; Jiang, Z.; Klima, M.; Fudenberg, G.; Hone, J.; Kim, P.; Stormer, H. L., Ultrahigh electron mobility in suspended graphene. *Solid State Communications* 2008, 146 (9), 351-355.
58. Balandin, A. A.; Ghosh, S.; Bao, W.; Calizo, I.; Teweldebrhan, D.; Miao, F.; Lau, C. N., Superior Thermal Conductivity of Single-Layer Graphene. *Nano Letters* 2008, 8 (3), 902-907.
59. Cong, H.-P.; Ren, X.-C.; Wang, P.; Yu, S.-H., Wet-spinning assembly of continuous, neat, and macroscopic graphene fibers. *Sci Rep-Uk* 2012, 2, 613.
60. Xiang, C.; Young, C. C.; Wang, X.; Yan, Z.; Hwang, C.-C.; Ceriotti, G.; Lin, J.; Kono, J.; Pasquali, M.; Tour, J. M., Large Flake Graphene Oxide Fibers with Unconventional 100% Knot Efficiency and Highly Aligned Small Flake Graphene Oxide Fibers. *Adv Mater* 2013, 25 (33), 4592-4597.
61. Huang, G.; Hou, C.; Shao, Y.; Wang, H.; Zhang, Q.; Li, Y.; Zhu, M., Highly Strong and Elastic Graphene Fibres Prepared from Universal Graphene Oxide Precursors. *Sci Rep-Uk* 2014, 4, 4248.
62. Chen, S.; Ma, W.; Cheng, Y.; Weng, Z.; Sun, B.; Wang, L.; Chen, W.; Li, F.; Zhu, M.; Cheng,

- H.-M., Scalable non-liquid-crystal spinning of locally aligned graphene fibers for high-performance wearable supercapacitors. *Nano Energy* 2015, 15 (Supplement C), 642-653.
63. Xin, G.; Yao, T.; Sun, H.; Scott, S. M.; Shao, D.; Wang, G.; Lian, J., Highly thermally conductive and mechanically strong graphene fibers. *Science* 2015, 349 (6252), 1083-1087.
64. Seyedin, S.; Romano, M. S.; Minett, A. I.; Razal, J. M., Towards the Knittability of Graphene Oxide Fibres. *Sci Rep-Uk* 2015, 5, 14946.
65. Xiang, C.; Behabtu, N.; Liu, Y.; Chae, H. G.; Young, C. C.; Genorio, B.; Tsentlovich, D. E.; Zhang, C.; Kosynkin, D. V.; Lomeda, J. R.; Hwang, C.-C.; Kumar, S.; Pasquali, M.; Tour, J. M., Graphene Nanoribbons as an Advanced Precursor for Making Carbon Fiber. *ACS Nano* 2013, 7 (2), 1628-1637.
66. Xu, Z.; Liu, Y.; Zhao, X.; Peng, L.; Sun, H.; Xu, Y.; Ren, X.; Jin, C.; Xu, P.; Wang, M.; Gao, C., Ultrastiff and Strong Graphene Fibers via Full-Scale Synergetic Defect Engineering. *Adv Mater* 2016, 28 (30), 6449-6456.
67. Liu, Y.; Xu, Z.; Zhan, J.; Li, P.; Gao, C., Superb Electrically Conductive Graphene Fibers via Doping Strategy. *Adv Mater* 2016, 28 (36), 7941-7947.
68. Fang, B.; Xi, J.; Liu, Y.; Guo, F.; Xu, Z.; Gao, W.; Guo, D.; Li, P.; Gao, C., Wrinkle-stabilized metal-graphene hybrid fibers with zero temperature coefficient of resistance. *Nanoscale* 2017, 9 (33), 12178-12188.
69. Li, M.; Zhang, X.; Wang, X.; Ru, Y.; Qiao, J., Ultrastrong Graphene-Based Fibers with Increased Elongation. *Nano Letters* 2016, 16 (10), 6511-6515.
70. Zhang, D.; Peng, L.; Shi, N.; Yu, Y.; Min, Y.; Epstein, A. J., Self-assembled high-performance graphene oxide fibers using ionic liquid as coagulating agent. *Journal of Materials Science* 2017, 52 (13), 7698-7708.

71. Kou, L.; Gao, C., Bioinspired design and macroscopic assembly of poly(vinyl alcohol)-coated graphene into kilometers-long fibers. *Nanoscale* 2013, 5 (10), 4370-4378.
72. Liu, Y.; Xu, Z.; Gao, W.; Cheng, Z.; Gao, C., Graphene and Other 2D Colloids: Liquid Crystals and Macroscopic Fibers. *Adv Mater* 2017, 29 (14), 1606794-n/a.
73. VI. The phenomena of rupture and flow in solids. *Philosophical Transactions of the Royal Society of London. Series A, Containing Papers of a Mathematical or Physical Character* 1921, 221 (582-593), 163-198.
74. Chen, L.; He, Y.; Chai, S.; Qiang, H.; Chen, F.; Fu, Q., Toward high performance graphene fibers. *Nanoscale* 2013, 5 (13), 5809-5815.
75. Zhang, Y.; Li, Y.; Ming, P.; Zhang, Q.; Liu, T.; Jiang, L.; Cheng, Q., Ultrastrong Bioinspired Graphene-Based Fibers via Synergistic Toughening. *Adv Mater* 2016, 28 (14), 2834-2839.
76. Sun, J.; Li, Y.; Peng, Q.; Hou, S.; Zou, D.; Shang, Y.; Li, Y.; Li, P.; Du, Q.; Wang, Z.; Xia, Y.; Xia, L.; Li, X.; Cao, A., Macroscopic, Flexible, High-Performance Graphene Ribbons. *ACS Nano* 2013, 7 (11), 10225-10232.
77. Kim, H.; Jalili, R.; Spinks, G. M.; Wallace, G. G.; Kim, S. J., High-strength graphene and polyacrylonitrile composite fiber enhanced by surface coating with polydopamine. *Composites Science and Technology* 2017, 149 (Supplement C), 280-285.
78. Morimune-Moriya, S.; Ariyoshi, M.; Goto, T.; Nishino, T., Ultradrawing of poly (vinyl alcohol)/Graphene oxide nanocomposite fibers toward high mechanical performances. *Composites Science and Technology* 2017, 152 (Supplement C), 159-164.
79. Liu, Y.; Liang, H.; Xu, Z.; Xi, J.; Chen, G.; Gao, W.; Xue, M.; Gao, C., Superconducting Continuous Graphene Fibers via Calcium Intercalation. *ACS Nano* 2017, 11 (4), 4301-4306.
80. Kim, T. Y.; Park, C.-H.; Marzari, N., The Electronic Thermal Conductivity of Graphene.

- Nano Letters 2016, 16 (4), 2439-2443.
81. Meng, Y.; Zhao, Y.; Hu, C.; Cheng, H.; Hu, Y.; Zhang, Z.; Shi, G.; Qu, L., All-Graphene Core-Sheath Microfibers for All-Solid-State, Stretchable Fibriform Supercapacitors and Wearable Electronic Textiles. *Adv Mater* 2013, 25 (16), 2326-2331.
 82. Le, V. T.; Kim, H.; Ghosh, A.; Kim, J.; Chang, J.; Vu, Q. A.; Pham, D. T.; Lee, J.-H.; Kim, S.-W.; Lee, Y. H., Coaxial Fiber Supercapacitor Using All-Carbon Material Electrodes. *ACS Nano* 2013, 7 (7), 5940-5947.
 83. Ma, W.; Chen, S.; Yang, S.; Chen, W.; Cheng, Y.; Guo, Y.; Peng, S.; Ramakrishna, S.; Zhu, M., Hierarchical MnO₂ nanowire/graphene hybrid fibers with excellent electrochemical performance for flexible solid-state supercapacitors. *J Power Sources* 2016, 306 (Supplement C), 481-488.
 84. Zhang, J.; Yang, X.; He, Y.; Bai, Y.; Kang, L.; Xu, H.; Shi, F.; Lei, Z.; Liu, Z.-H., [small delta]-MnO₂/holey graphene hybrid fiber for all-solid-state supercapacitor. *J Mater Chem A* 2016, 4 (23), 9088-9096.
 85. Ding, X.; Zhao, Y.; Hu, C.; Hu, Y.; Dong, Z.; Chen, N.; Zhang, Z.; Qu, L., Spinning fabrication of graphene/polypyrrole composite fibers for all-solid-state, flexible fibriform supercapacitors. *J Mater Chem A* 2014, 2 (31), 12355-12360.
 86. Yang, Q.; Xu, Z.; Fang, B.; Huang, T.; Cai, S.; Chen, H.; Liu, Y.; Gopalsamy, K.; Gao, W.; Gao, C., MXene/graphene hybrid fibers for high performance flexible supercapacitors. *J Mater Chem A* 2017, 5 (42), 22113-22119.
 87. Hoshida, T.; Zheng, Y.; Hou, J.; Wang, Z.; Li, Q.; Zhao, Z.; Ma, R.; Sasaki, T.; Geng, F., Flexible Lithium-Ion Fiber Battery by the Regular Stacking of Two-Dimensional Titanium Oxide Nanosheets Hybridized with Reduced Graphene Oxide. *Nano Letters* 2017, 17 (6),

- 3543-3549.
88. Yang, Z.; Sun, H.; Chen, T.; Qiu, L.; Luo, Y.; Peng, H., Photovoltaic Wire Derived from a Graphene Composite Fiber Achieving an 8.45 % Energy Conversion Efficiency. *Angewandte Chemie* 2013, 125 (29), 7693-7696.
 89. Cheng, H.; Liu, J.; Zhao, Y.; Hu, C.; Zhang, Z.; Chen, N.; Jiang, L.; Qu, L., Graphene Fibers with Predetermined Deformation as Moisture-Triggered Actuators and Robots. *Angewandte Chemie International Edition* 2013, 52 (40), 10482-10486.
 90. Cheng, H.; Hu, Y.; Zhao, F.; Dong, Z.; Wang, Y.; Chen, N.; Zhang, Z.; Qu, L., Moisture-Activated Torsional Graphene-Fiber Motor. *Adv Mater* 2014, 26 (18), 2909-2913.
 91. Li, Z.; Xu, Z.; Liu, Y.; Wang, R.; Gao, C., Multifunctional non-woven fabrics of interfused graphene fibres. *Nat Commun* 2016, 7, 13684.
 92. Luo, Y.-B.; Yuan, B.-F.; Yu, Q.-W.; Feng, Y.-Q., Substrateless graphene fiber: A sorbent for solid-phase microextraction. *Journal of Chromatography A* 2012, 1268 (Supplement C), 9-15.
 93. Jost, K.; Stenger, D.; Perez, C. R.; McDonough, J. K.; Lian, K.; Gogotsi, Y.; Dion, G., Knitted and screen printed carbon-fiber supercapacitors for applications in wearable electronics. *Energy & Environmental Science* 2013, 6 (9), 2698-2705.
 94. Zeng, W.; Shu, L.; Li, Q.; Chen, S.; Wang, F.; Tao, X. M., Fiber-Based Wearable Electronics: A Review of Materials, Fabrication, Devices, and Applications. *Advanced Materials* 2014, 26 (31), 5310-5336.
 95. Stoppa, M.; Chiolerio, A., Wearable Electronics and Smart Textiles: A Critical Review. *Sensors-Basel* 2014, 14 (7), 11957-11992.
 96. Meng, Y. N.; Zhao, Y.; Hu, C. G.; Cheng, H. H.; Hu, Y.; Zhang, Z. P.; Shi, G. Q.; Qu, L. T.,

- All-Graphene Core-Sheath Microfibers for All-Solid-State, Stretchable Fibriform Supercapacitors and Wearable Electronic Textiles. *Advanced Materials* 2013, 25 (16), 2326-2331.
97. Tao, J. Y.; Liu, N. S.; Ma, W. Z.; Ding, L. W.; Li, L. Y.; Su, J.; Gao, Y. H., Solid-State High Performance Flexible Supercapacitors Based on Polypyrrole-MnO₂-Carbon Fiber Hybrid Structure. *Sci Rep-Uk* 2013, 3.
98. Choi, C.; Lee, J. A.; Choi, A. Y.; Kim, Y. T.; Lepro, X.; Lima, M. D.; Baughman, R. H.; Kim, S. J., Flexible Supercapacitor Made of Carbon Nanotube Yarn with Internal Pores. *Advanced Materials* 2014, 26 (13), 2059-2065.
99. Gwon, H.; Kim, H. S.; Lee, K. U.; Seo, D. H.; Park, Y. C.; Lee, Y. S.; Ahn, B. T.; Kang, K., Flexible energy storage devices based on graphene paper. *Energy & Environmental Science* 2011, 4 (4), 1277-1283.
100. El-Kady, M. F.; Kaner, R. B., Scalable fabrication of high-power graphene micro-supercapacitors for flexible and on-chip energy storage. *Nat Commun* 2013, 4.
101. Salanne, M.; Rotenberg, B.; Naoi, K.; Kaneko, K.; Taberna, P. L.; Grey, C. P.; Dunn, B.; Simon, P., Efficient storage mechanisms for building better supercapacitors. *Nature Energy* 2016, 1, 16070.
102. Qu, G.; Cheng, J.; Li, X.; Yuan, D.; Chen, P.; Chen, X.; Wang, B.; Peng, H., A Fiber Supercapacitor with High Energy Density Based on Hollow Graphene/Conducting Polymer Fiber Electrode. *Advanced Materials* 2016, 28 (19), 3646-3652.
103. Li, P.; Li, J.; Zhao, Z.; Fang, Z.; Yang, M.; Yuan, Z.; Zhang, Y.; Zhang, Q.; Hong, W.; Chen, X.; Yu, D., A General Electrode Design Strategy for Flexible Fiber Micro-Pseudocapacitors Combining Ultrahigh Energy and Power Delivery. *Advanced Science* 2017, 1700003-n/a.

104. Yu, D.; Zhai, S.; Jiang, W.; Goh, K.; Wei, L.; Chen, X.; Jiang, R.; Chen, Y., Transforming Pristine Carbon Fiber Tows into High Performance Solid-State Fiber Supercapacitors. *Advanced Materials* 2015, 27 (33), 4895-4901.
105. Yu, D.; Goh, K.; Zhang, Q.; Wei, L.; Wang, H.; Jiang, W.; Chen, Y., Controlled Functionalization of Carbonaceous Fibers for Asymmetric Solid-State Micro-Supercapacitors with High Volumetric Energy Density. *Advanced Materials* 2014, 26 (39), 6790-6797.
106. Yu, D. S.; Goh, K.; Wang, H.; Wei, L.; Jiang, W. C.; Zhang, Q.; Dai, L. M.; Chen, Y., Scalable synthesis of hierarchically structured carbon nanotube-graphene fibres for capacitive energy storage. *Nat Nanotechnol* 2014, 9 (7), 555-562.
107. Ding, L.; Stilwell, J.; Zhang, T.; Elboudwarej, O.; Jiang, H.; Selegue, J. P.; Cooke, P. A.; Gray, J. W.; Chen, F. F., Molecular Characterization of the Cytotoxic Mechanism of Multiwall Carbon Nanotubes and Nano-Onions on Human Skin Fibroblast. *Nano Lett* 2005, 5 (12), 2448-2464.
108. Cong, H.-P.; Chen, J.-F.; Yu, S.-H., Graphene-based macroscopic assemblies and architectures: an emerging material system. *Chem Soc Rev* 2014, 43 (21), 7295-7325.
109. Li, X.; Zhao, T.; Wang, K.; Yang, Y.; Wei, J.; Kang, F.; Wu, D.; Zhu, H., Directly Drawing Self-Assembled, Porous, and Monolithic Graphene Fiber from Chemical Vapor Deposition Grown Graphene Film and Its Electrochemical Properties. *Langmuir* 2011, 27 (19), 12164-12171.
110. Li, Z.; Liu, Z.; Sun, H.; Gao, C., Superstructured Assembly of Nanocarbons: Fullerenes, Nanotubes, and Graphene. *Chemical Reviews* 2015, 115 (15), 7046-7117.
111. Yang, X. W.; Cheng, C.; Wang, Y. F.; Qiu, L.; Li, D., Liquid-Mediated Dense Integration of

- Graphene Materials for Compact Capacitive Energy Storage. *Science* 2013, 341 (6145), 534-537.
112. Zhu, Y.; Murali, S.; Stoller, M. D.; Ganesh, K. J.; Cai, W.; Ferreira, P. J.; Pirkle, A.; Wallace, R. M.; Cychosz, K. A.; Thommes, M.; Su, D.; Stach, E. A.; Ruoff, R. S., Carbon-based supercapacitors produced by activation of graphene. *Science* 2011, 332 (6037), 1537-41.
113. Gao, W.; Singh, N.; Song, L.; Liu, Z.; Reddy, A. L. M.; Ci, L. J.; Vajtai, R.; Zhang, Q.; Wei, B. Q.; Ajayan, P. M., Direct laser writing of micro-supercapacitors on hydrated graphite oxide films. *Nat Nanotechnol* 2011, 6 (8), 496-500.
114. Hancock, T. A.; Spruiell, J. E.; White, J. L., Wet spinning of aliphatic and aromatic polyamides. *Journal of Applied Polymer Science* 1977, 21 (5), 1227-1247.
115. Zhang, S.; Koziol, K. K. K.; Kinloch, I. A.; Windle, A. H., Macroscopic Fibers of Well-Aligned Carbon Nanotubes by Wet Spinning. *Small* 2008, 4 (8), 1217-1222.
116. De Silva, R.; Vongsanga, K.; Wang, X. G.; Byrne, N., Understanding key wet spinning parameters in an ionic liquid spun regenerated cellulosic fibre. *Cellulose* 2016, 23 (4), 2741-2751.
117. Chen, J.; Wang, C. G.; Dong, X. G.; Liu, H. Z., Study on the coagulation mechanism of wet-spinning PAN fibers. *J Polym Res* 2006, 13 (6), 515-519.
118. Chen, S. H.; Ma, W. J.; Cheng, Y. H.; Weng, Z.; Sun, B.; Wang, L.; Chen, W. P.; Li, F.; Zhu, M. F.; Cheng, H. M., Scalable non-liquid-crystal spinning of locally aligned graphene fibers for high-performance wearable supercapacitors. *Nano Energy* 2015, 15, 642-653.
119. Aboutalebi, S. H.; Jalili, R.; Esrafilzadeh, D.; Salari, M.; Gholamvand, Z.; Yamini, S. A.; Konstantinov, K.; Shepherd, R. L.; Chen, J.; Moulton, S. E.; Innis, P. C.; Minett, A. I.; Razal, J. M.; Wallace, G. G., High-Performance Multifunctional Graphene Yarns: Toward Wearable

- All-Carbon Energy Storage Textiles. *Acs Nano* 2014, 8 (3), 2456-2466.
120. Park, S.; Lee, K.-S.; Bozoklu, G.; Cai, W.; Nguyen, S. T.; Ruoff, R. S., Graphene Oxide Papers Modified by Divalent Ions—Enhancing Mechanical Properties via Chemical Cross-Linking. *ACS Nano* 2008, 2 (3), 572-578.
 121. Konios, D.; Stylianakis, M. M.; Stratakis, E.; Kymakis, E., Dispersion behaviour of graphene oxide and reduced graphene oxide. *J Colloid Interf Sci* 2014, 430, 108-112.
 122. Bouchard, J.; Cayla, A.; Odent, S.; Lutz, V.; Devaux, E.; Campagne, C., Processing and characterization of polyethersulfone wet-spun nanocomposite fibres containing multiwalled carbon nanotubes. *Synthetic Met* 2016, 217, 304-313.
 123. Hou, S. C.; Wang, X. C.; Zhang, X. X., Fabrication and wet spinning of a fully aromatic meta-polybenzimidazole. *High Perform Polym* 2016, 28 (3), 288-295.
 124. Xin, G. Q.; Yao, T. K.; Sun, H. T.; Scott, S. M.; Shao, D. L.; Wang, G. K.; Lian, J., Highly thermally conductive and mechanically strong graphene fibers. *Science* 2015, 349 (6252), 1083-1087.
 125. Xu, Z.; Sun, H. Y.; Zhao, X. L.; Gao, C., Ultrastrong Fibers Assembled from Giant Graphene Oxide Sheets. *Advanced Materials* 2013, 25 (2), 188-193.
 126. Sun, J. K.; Li, Y. H.; Peng, Q. Y.; Hou, S. C.; Zou, D. C.; Shang, Y. Y.; Li, Y. B.; Li, P. X.; Du, Q. J.; Wang, Z. H.; Xia, Y. Z.; Xia, L. H.; Li, X. L.; Cao, A. Y., Macroscopic, Flexible, High-Performance Graphene Ribbons. *Acs Nano* 2013, 7 (11), 10225-10232.
 127. Xu, Z.; Liu, Z.; Sun, H. Y.; Gao, C., Highly Electrically Conductive Ag-Doped Graphene Fibers as Stretchable Conductors. *Adv Mater* 2013, 25 (23), 3249-3253.
 128. Xiang, C. S.; Behabtu, N.; Liu, Y. D.; Chae, H. G.; Young, C. C.; Genorio, B.; Tsentelovich, D. E.; Zhang, C. G.; Kosynkin, D. V.; Lomeda, J. R.; Hwang, C. C.; Kumar, S.; Pasquali, M.;

- Tour, J. M., Graphene Nanoribbons as an Advanced Precursor for Making Carbon Fiber. *Acs Nano* 2013, 7 (2), 1628-1637.
129. Gilje, S.; Han, S.; Wang, M.; Wang, K. L.; Kaner, R. B., A chemical route to graphene for device applications. *Nano Letters* 2007, 7 (11), 3394-3398.
130. Johnson, D. W.; Dobson, B. P.; Coleman, K. S., A manufacturing perspective on graphene dispersions. *Current Opinion in Colloid & Interface Science* 2015, 20 (5–6), 367-382.
131. Gao, W.; Alemany, L. B.; Ci, L.; Ajayan, P. M., New insights into the structure and reduction of graphite oxide. *Nat Chem* 2009, 1 (5), 403-408.
132. He, N.; Yildiz, O.; Pan, Q.; Zhu, J.; Zhang, X.; Bradford, P. D.; Gao, W., Pyrolytic-carbon coating in carbon nanotube foams for better performance in supercapacitors. *J Power Sources* 2017, 343, 492-501.
133. Hansen, C. M., Hansen solubility parameters: a user's handbook. CRC press: 2007.
134. Mezzenga, R.; Meyer, C.; Servais, C.; Romoscanu, A. I.; Sagalowicz, L.; Hayward, R. C., Shear Rheology of Lyotropic Liquid Crystals: A Case Study. *Langmuir* 2005, 21 (8), 3322-3333.
135. Um, I. C.; Kweon, H. Y.; Lee, K. G.; Ihm, D. W.; Lee, J. H.; Park, Y. H., Wet spinning of silk polymer - I. Effect of coagulation conditions on the morphological feature of filament. *Int J Biol Macromol* 2004, 34 (1-2), 89-105.
136. Kou, L.; Huang, T. Q.; Zheng, B. N.; Han, Y.; Zhao, X. L.; Gopalsamy, K.; Sun, H. Y.; Gao, C., Coaxial wet-spun yarn supercapacitors for high-energy density and safe wearable electronics. *Nat Commun* 2014, 5.
137. Cong, H. P.; Ren, X. C.; Wang, P.; Yu, S. H., Wet-spinning assembly of continuous, neat, and macroscopic graphene fibers. *Sci Rep-Uk* 2012, 2.

138. Huang, T. Q.; Zheng, B. N.; Kou, L.; Gopalsamy, K.; Xu, Z.; Gao, C.; Meng, Y. N.; Wei, Z. X., Flexible high performance wet-spun graphene fiber supercapacitors. *Rsc Adv* 2013, 3 (46), 23957-23962.
139. Zhao, X. L.; Zheng, B. N.; Huang, T. Q.; Gao, C., Graphene-based single fiber supercapacitor with a coaxial structure. *Nanoscale* 2015, 7 (21), 9399-9404.
140. Liu, L. B.; Yu, Y.; Yan, C.; Li, K.; Zheng, Z. J., Wearable energy-dense and power-dense supercapacitor yarns enabled by scalable graphene-metallic textile composite electrodes. *Nat Commun* 2015, 6.
141. Ren, J.; Bai, W. Y.; Guan, G. Z.; Zhang, Y.; Peng, H. S., Flexible and Weaveable Capacitor Wire Based on a Carbon Nanocomposite Fiber. *Advanced Materials* 2013, 25 (41), 5965-5970.
142. Lee, J. A.; Shin, M. K.; Kim, S. H.; Cho, H. U.; Spinks, G. M.; Wallace, G. G.; Lima, M. D.; Lepro, X.; Kozlov, M. E.; Baughman, R. H.; Kim, S. J., Ultrafast charge and discharge biscrolled yarn supercapacitors for textiles and microdevices. *Nat Commun* 2013, 4.
143. Pech, D.; Brunet, M.; Durou, H.; Huang, P. H.; Mochalin, V.; Gogotsi, Y.; Taberna, P. L.; Simon, P., Ultrahigh-power micrometre-sized supercapacitors based on onion-like carbon. *Nat Nanotechnol* 2010, 5 (9), 651-654.
144. Xiao, X.; Li, T. Q.; Yang, P. H.; Gao, Y.; Jin, H. Y.; Ni, W. J.; Zhan, W. H.; Zhang, X. H.; Cao, Y. Z.; Zhong, J. W.; Gong, L.; Yen, W. C.; Mai, W. J.; Chen, J.; Huo, K. F.; Chueh, Y. L.; Wang, Z. L.; Zhou, J., Fiber-Based All-Solid-State Flexible Supercapacitors for Self-Powered Systems. *Acs Nano* 2012, 6 (10), 9200-9206.
145. Du, X.; Skachko, I.; Barker, A.; Andrei, E. Y., Approaching ballistic transport in suspended graphene. *Nat Nanotechnol* 2008, 3 (8), 491-495.

146. Lee, C.; Wei, X. D.; Kysar, J. W.; Hone, J., Measurement of the elastic properties and intrinsic strength of monolayer graphene. *Science* 2008, 321 (5887), 385-388.
147. Seol, J. H.; Jo, I.; Moore, A. L.; Lindsay, L.; Aitken, Z. H.; Pettes, M. T.; Li, X. S.; Yao, Z.; Huang, R.; Broido, D.; Mingo, N.; Ruoff, R. S.; Shi, L., Two-Dimensional Phonon Transport in Supported Graphene. *Science* 2010, 328 (5975), 213-216.
148. Stoller, M. D.; Park, S.; Zhu, Y.; An, J.; Ruoff, R. S., Graphene-Based Ultracapacitors. *Nano Letters* 2008, 8 (10), 3498-3502.
149. Liu, C.; Yu, Z.; Neff, D.; Zhamu, A.; Jang, B. Z., Graphene-Based Supercapacitor with an Ultrahigh Energy Density. *Nano Letters* 2010, 10 (12), 4863-4868.
150. Liu, Y. J.; Xu, Z.; Gao, W. W.; Cheng, Z. D.; Gao, C., Graphene and Other 2D Colloids: Liquid Crystals and Macroscopic Fibers. *Adv Mater* 2017, 29 (14).
151. Becerril, H. A.; Mao, J.; Liu, Z.; Stoltenberg, R. M.; Bao, Z.; Chen, Y., Evaluation of solution-processed reduced graphene oxide films as transparent conductors. *ACS nano* 2008, 2 (3), 463-470.
152. Li, J.; Li, J.; Meng, H.; Xie, S.; Zhang, B.; Li, L.; Ma, H.; Zhang, J.; Yu, M., Ultra-light, compressible and fire-resistant graphene aerogel as a highly efficient and recyclable absorbent for organic liquids. *J Mater Chem A* 2014, 2 (9), 2934-2941.
153. Xu, Z.; Gao, C., Graphene fiber: a new trend in carbon fibers. *Materials Today* 2015, 18 (9), 480-492.
154. Seyedin, S.; Yanza, E. R. S.; Razal, J., Knittable energy storing fiber with high volumetric performance made from predominantly MXene nanosheets. *J Mater Chem A* 2017, 5 (46), 24076-24082.
155. Lim, L.; Liu, Y.; Liu, W.; Tjandra, R.; Rasenthiram, L.; Chen, Z.; Yu, A., All-in-One

- Graphene Based Composite Fiber: Toward Wearable Supercapacitor. *ACS Applied Materials & Interfaces* 2017, 9 (45), 39576-39583.
156. Li, B.; Cheng, J.; Wang, Z.; Li, Y.; Ni, W.; Wang, B., Highly-wrinkled reduced graphene oxide-conductive polymer fibers for flexible fiber-shaped and interdigital-designed supercapacitors. *J Power Sources* 2018, 376, 117-124.
 157. Soavi, F.; Bettini, L. G.; Piseri, P.; Milani, P.; Santoro, C.; Atanassov, P.; Arbizzani, C., Miniaturized supercapacitors: key materials and structures towards autonomous and sustainable devices and systems. *J Power Sources* 2016, 326, 717-725.
 158. Li, L.; Lou, Z.; Chen, D.; Jiang, K.; Han, W.; Shen, G., Recent Advances in Flexible/Stretchable Supercapacitors for Wearable Electronics. *Small* 2018, 14 (43), 1702829.
 159. Cong, H. P.; Chen, J. F.; Yu, S. H., Graphene-based macroscopic assemblies and architectures: an emerging material system. *Chem Soc Rev* 2014, 43 (21), 7295-7325.
 160. Kim, Y. S.; Kang, J. H.; Kim, T.; Jung, Y.; Lee, K.; Oh, J. Y.; Park, J.; Park, C. R., Easy Preparation of Readily Self-Assembled High-Performance Graphene Oxide Fibers. *Chemistry of Materials* 2014, 26 (19), 5549-5555.
 161. Mock, G., Fundamentals of dyeing and printing. Lecture notebook, College of Textiles, NCSU 1997.
 162. Overbeek, J. T. G., The Rule of Schulze and Hardy. In *Pure and Applied Chemistry*, 1980; Vol. 52, p 1151.
 163. Sano, M.; Okamura, J.; Shinkai, S., Colloidal Nature of Single-Walled Carbon Nanotubes in Electrolyte Solution: The Schulze–Hardy Rule. *Langmuir* 2001, 17 (22), 7172-7173.
 164. Nowicki, W.; Nowicka, G., Verification of the Schulze-Hardy Rule: A Colloid Chemistry

- Experiment. *Journal of Chemical Education* 1994, 71 (7), 624.
165. Yeh, C. N.; Raidongia, K.; Shao, J. J.; Yang, Q. H.; Huang, J. X., On the origin of the stability of graphene oxide membranes in water. *Nat Chem* 2015, 7 (2), 166-170.
166. Chen, L.; Shi, G.; Shen, J.; Peng, B.; Zhang, B.; Wang, Y.; Bian, F.; Wang, J.; Li, D.; Qian, Z.; Xu, G.; Liu, G.; Zeng, J.; Zhang, L.; Yang, Y.; Zhou, G.; Wu, M.; Jin, W.; Li, J.; Fang, H., Ion sieving in graphene oxide membranes via cationic control of interlayer spacing. *Nature* 2017, 550, 380.
167. Yang, K.; Chen, B.; Zhu, X.; Xing, B., Aggregation, Adsorption, and Morphological Transformation of Graphene Oxide in Aqueous Solutions Containing Different Metal Cations. *Environmental Science & Technology* 2016, 50 (20), 11066-11075.
168. Yang, C. H.; Wang, M. X.; Haider, H.; Yang, J. H.; Sun, J. Y.; Chen, Y. M.; Zhou, J. X.; Suo, Z. G., Strengthening Alginate/Polyacrylamide Hydrogels Using Various Multivalent Cations. *Acs Applied Materials & Interfaces* 2013, 5 (21), 10418-10422.
169. Sun, P.; Zheng, F.; Zhu, M.; Song, Z.; Wang, K.; Zhong, M.; Wu, D.; Little, R. B.; Xu, Z.; Zhu, H., Selective Trans-Membrane Transport of Alkali and Alkaline Earth Cations through Graphene Oxide Membranes Based on Cation- π Interactions. *ACS Nano* 2014, 8 (1), 850-859.
170. Xu, Z.; Peng, L.; Liu, Y. J.; Liu, Z.; Sun, H. Y.; Gao, W. W.; Gao, C., Experimental Guidance to Graphene Macroscopic Wet-Spun Fibers, Continuous Papers, and Ultralightweight Aerogels. *Chemistry of Materials* 2017, 29 (1), 319-330.
171. Chen, S.; Ma, W.; Cheng, Y.; Weng, Z.; Sun, B.; Wang, L.; Chen, W.; Li, F.; Zhu, M.; Cheng, H.-M., Scalable non-liquid-crystal spinning of locally aligned graphene fibers for high-performance wearable supercapacitors. *Nano Energy* 2015, 15, 642-653.

172. Zhang, Y.; Yang, W., Comment on "Generalized Gradient Approximation Made Simple".
Phys Rev Lett 1998, 80 (4), 890-890.
173. Perdew, J. P.; Chevary, J.; Vosko, S.; Jackson, K. A.; Pederson, M. R.; Singh, D.; Fiolhais, C., Atoms, molecules, solids, and surfaces: Applications of the generalized gradient approximation for exchange and correlation. Physical Review B 1992, 46 (11), 6671.
174. Blöchl, P. E., Projector augmented-wave method. Physical Review B 1994, 50 (24), 17953.
175. Hohenberg, P.; Kohn, W., Inhomogeneous electron gas. Physical Review 1964, 136 (3B), B864-B871.
176. Kohn, W.; Sham, L. J., Self-consistent equations including exchange and correlation effects. Physical Review 1965, 140 (4A), A1133-A1138.
177. Parr, R. G.; Yang, W., Density-functional theory of atoms and molecules. Oxford university press: 1989; Vol. 16.
178. Martin, R. M., Electronic structure: basic theory and practical methods. Cambridge university press: 2004.
179. Kresse, G.; Hafner, J., Ab initio molecular-dynamics simulation of the liquid-metal–amorphous-semiconductor transition in germanium. Physical Review B 1994, 49 (20), 14251.
180. Kresse, G.; Furthmüller, J., Efficient iterative schemes for ab initio total-energy calculations using a plane-wave basis set. Physical Review B 1996, 54 (16), 11169.
181. Kresse, G.; Furthmüller, J., Efficiency of ab-initio total energy calculations for metals and semiconductors using a plane-wave basis set. Computational Materials Science 1996, 6 (1), 15-50.
182. Kresse, G.; Joubert, D., From ultrasoft pseudopotentials to the projector augmented-wave

- method. *Physical Review B* 1999, 59 (3), 1758.
183. Monkhorst, H. J.; Pack, J. D., Special points for Brillouin-zone integrations. *Physical Review B* 1976, 13 (12), 5188.
 184. Sun, P.; Liu, H.; Wang, K.; Zhong, M.; Wu, D.; Zhu, H., Selective Ion Transport through Functionalized Graphene Membranes Based on Delicate Ion–Graphene Interactions. *The Journal of Physical Chemistry C* 2014, 118 (33), 19396-19401.
 185. Yang, J.; Shi, G.; Tu, Y.; Fang, H., High Correlation between Oxidation Loci on Graphene Oxide. *Angewandte Chemie International Edition* 2014, 53 (38), 10190-10194.
 186. He, H.; Klinowski, J.; Forster, M.; Lerf, A., A new structural model for graphite oxide. *Chemical Physics Letters* 1998, 287 (1), 53-56.
 187. Marcus, Y., Thermodynamics of solvation of ions. Part 5.-Gibbs free energy of hydration at 298.15 K. *Journal of the Chemical Society, Faraday Transactions* 1991, 87 (18), 2995-2999.
 188. Tansel, B.; Sager, J.; Rector, T.; Garland, J.; Strayer, R. F.; Levine, L.; Roberts, M.; Hummerick, M.; Bauer, J., Significance of hydrated radius and hydration shells on ionic permeability during nanofiltration in dead end and cross flow modes. *Separation and Purification Technology* 2006, 51 (1), 40-47.
 189. Liu, Y.; Xie, B.; Zhang, Z.; Zheng, Q.; Xu, Z., Mechanical properties of graphene papers. *Journal of the Mechanics and Physics of Solids* 2012, 60 (4), 591-605.
 190. Ebbesen, T.; Lezec, H.; Hiura, H.; Bennett, J.; Ghaemi, H.; Thio, T., Electrical conductivity of individual carbon nanotubes. *Nature* 1996, 382 (6586), 54-56.
 191. Pech, D.; Brunet, M.; Durou, H.; Huang, P.; Mochalin, V.; Gogotsi, Y.; Taberna, P.-L.; Simon, P., Ultrahigh-power micrometre-sized supercapacitors based on onion-like carbon. *Nat Nanotechnol* 2010, 5, 651.

192. Liu, L.; Yu, Y.; Yan, C.; Li, K.; Zheng, Z., Wearable energy-dense and power-dense supercapacitor yarns enabled by scalable graphene–metallic textile composite electrodes. *Nat Commun* 2015, 6, 7260.
193. Chen, G.; Chen, T.; Hou, K.; Ma, W.; Tebyetekerwa, M.; Cheng, Y.; Weng, W.; Zhu, M., Robust, hydrophilic graphene/cellulose nanocrystal fiber-based electrode with high capacitive performance and conductivity. *Carbon* 2018, 127, 218-227.
194. Meng, J.; Nie, W.; Zhang, K.; Xu, F.; Ding, X.; Wang, S.; Qiu, Y., Enhancing electrochemical performance of graphene fiber-based supercapacitors by plasma treatment. *ACS applied materials & interfaces* 2018.
195. Ma, Y.; Li, P.; Sedloff, J. W.; Zhang, X.; Zhang, H.; Liu, J., Conductive Graphene Fibers for Wire-Shaped Supercapacitors Strengthened by Unfunctionalized Few-Walled Carbon Nanotubes. *ACS Nano* 2015, 9 (2), 1352-1359.
196. Mo, M.; Chen, C.; Gao, H.; Chen, M.; Li, D., Wet-spinning assembly of cellulose nanofibers reinforced graphene/polypyrrole microfibers for high performance fiber-shaped supercapacitors. *Electrochim Acta* 2018, 269, 11-20.
197. Chen, S.; Wang, L.; Huang, M.; Kang, L.; Lei, Z.; Xu, H.; Shi, F.; Liu, Z.-H., Reduced graphene oxide/Mn₃O₄ nanocrystals hybrid fiber for flexible all-solid-state supercapacitor with excellent volumetric energy density. *Electrochim Acta* 2017, 242, 10-18.
198. Zhang, J.; Yang, X.; He, Y.; Bai, Y.; Kang, L.; Xu, H.; Shi, F.; Lei, Z.; Liu, Z.-H., δ -MnO₂/holey graphene hybrid fiber for all-solid-state supercapacitor. *J Mater Chem A* 2016, 4 (23), 9088-9096.
199. Ma, W.; Chen, S.; Yang, S.; Chen, W.; Cheng, Y.; Guo, Y.; Peng, S.; Ramakrishna, S.; Zhu, M., Hierarchical MnO₂ nanowire/graphene hybrid fibers with excellent electrochemical

- performance for flexible solid-state supercapacitors. *J Power Sources* 2016, 306, 481-488.
200. Jost, K.; Dion, G.; Gogotsi, Y., Textile energy storage in perspective. *J Mater Chem A* 2014, 2 (28), 10776-10787.
201. Wang, Z. L.; Wu, W., Nanotechnology-Enabled Energy Harvesting for Self-Powered Micro-/Nanosystems. *Angewandte Chemie International Edition* 2012, 51 (47), 11700-11721.
202. Jost, K.; Durkin, D. P.; Haverhals, L. M.; Brown, E. K.; Langenstein, M.; De Long, H. C.; Trulove, P. C.; Gogotsi, Y.; Dion, G., Natural Fiber Welded Electrode Yarns for Knittable Textile Supercapacitors. *Advanced Energy Materials* 2015, 5 (4).
203. Yu, D. S.; Qian, Q. H.; Wei, L.; Jiang, W. C.; Goh, K. L.; Wei, J.; Zhang, J.; Chen, Y., Emergence of fiber supercapacitors. *Chem Soc Rev* 2015, 44 (3), 647-662.
204. Zhong, C.; Deng, Y. D.; Hu, W. B.; Qiao, J. L.; Zhang, L.; Zhang, J. J., A review of electrolyte materials and compositions for electrochemical supercapacitors. *Chem Soc Rev* 2015, 44 (21), 7484-7539.
205. Sun, H.; Zhang, Y.; Zhang, J.; Sun, X. M.; Peng, H. S., Energy harvesting and storage in 1D devices. *Nature Reviews Materials* 2017, 2 (6).
206. Bae, J.; Song, M. K.; Park, Y. J.; Kim, J. M.; Liu, M.; Wang, Z. L., Fiber Supercapacitors Made of Nanowire-Fiber Hybrid Structures for Wearable/Flexible Energy Storage. *Angewandte Chemie International Edition* 2011, 50 (7), 1683-1687.
207. Chai, Z.; Zhang, N.; Sun, P.; Huang, Y.; Zhao, C.; Fan, H. J.; Fan, X.; Mai, W., Tailorable and Wearable Textile Devices for Solar Energy Harvesting and Simultaneous Storage. *ACS Nano* 2016, 10 (10), 9201-9207.
208. Huang, Y.; Ip, W. S.; Lau, Y. Y.; Sun, J.; Zeng, J.; Yeung, N. S. S.; Ng, W. S.; Li, H.; Pei, Z.; Xue, Q.; Wang, Y.; Yu, J.; Hu, H.; Zhi, C., Weavable, Conductive Yarn-Based NiCo//Zn

- Textile Battery with High Energy Density and Rate Capability. *ACS Nano* 2017, 11 (9), 8953-8961.
209. Lu, X. H.; Yu, M. H.; Wang, G. M.; Tong, Y. X.; Li, Y., Flexible solid-state supercapacitors: design, fabrication and applications. *Energy & Environmental Science* 2014, 7 (7), 2160-2181.
210. Cai, X.; Peng, M.; Yu, X.; Fu, Y.; Zou, D., Flexible planar/fiber-architected supercapacitors for wearable energy storage. *Journal of Materials Chemistry C* 2014, 2 (7), 1184-1200.
211. Yang, Q.; Xu, Z.; Gao, C., Graphene fiber based supercapacitors: Strategies and perspective toward high performances. *Journal of Energy Chemistry* 2018, 27 (1), 6-11.
212. Simon, P.; Gogotsi, Y., Materials for electrochemical capacitors. *Nature Materials* 2008, 7, 845.
213. Yang, Z.; Zhao, W.; Niu, Y.; Zhang, Y.; Wang, L.; Zhang, W.; Xiang, X.; Li, Q., Direct spinning of high-performance graphene fiber supercapacitor with a three-ply core-sheath structure. *Carbon* 2018, 132, 241-248.
214. Meng, J.; Nie, W.; Zhang, K.; Xu, F.; Ding, X.; Wang, S.; Qiu, Y., Enhancing Electrochemical Performance of Graphene Fiber-Based Supercapacitors by Plasma Treatment. *ACS Applied Materials & Interfaces* 2018, 10 (16), 13652-13659.
215. Wang, G.; Zhang, L.; Zhang, J., A review of electrode materials for electrochemical supercapacitors. *Chem Soc Rev* 2012, 41 (2), 797-828.
216. Ma, W.; Chen, S.; Yang, S.; Chen, W.; Weng, W.; Cheng, Y.; Zhu, M., Flexible all-solid-state asymmetric supercapacitor based on transition metal oxide nanorods/reduced graphene oxide hybrid fibers with high energy density. *Carbon* 2017, 113, 151-158.
217. Zhang, J.; Yang, X.; He, Y.; Bai, Y.; Kang, L.; Xu, H.; Shi, F.; Lei, Z.; Liu, Z.-H., δ -

- MnO₂/holey graphene hybrid fiber for all-solid-state supercapacitor. *J Mater Chem A* 2016, 4 (23), 9088-9096.
218. Wang, B.; Wu, Q.; Sun, H.; Zhang, J.; Ren, J.; Luo, Y.; Wang, M.; Peng, H., An intercalated graphene/(molybdenum disulfide) hybrid fiber for capacitive energy storage. *J Mater Chem A* 2017, 5 (3), 925-930.
219. Cai, W.; Lai, T.; Lai, J.; Xie, H.; Ouyang, L.; Ye, J.; Yu, C., Transition metal sulfides grown on graphene fibers for wearable asymmetric supercapacitors with high volumetric capacitance and high energy density. *Sci Rep-Uk* 2016, 6, 26890.
220. Naguib, M.; Kurtoglu, M.; Presser, V.; Lu, J.; Niu, J.; Heon, M.; Hultman, L.; Gogotsi, Y.; Barsoum, M. W., Two-Dimensional Nanocrystals Produced by Exfoliation of Ti₃AlC₂. *Adv Mater* 2011, 23 (37), 4248-4253.
221. Lukatskaya, M. R.; Kota, S.; Lin, Z. F.; Zhao, M. Q.; Shpigel, N.; Levi, M. D.; Halim, J.; Taberna, P. L.; Barsoum, M.; Simon, P.; Gogotsi, Y., Ultra-high-rate pseudocapacitive energy storage in two-dimensional transition metal carbides. *Nat Energy* 2017, 2 (8).
222. Seyedin, S.; Yanza, E. R. S.; Razal, J. M., Knittable energy storing fiber with high volumetric performance made from predominantly MXene nanosheets. *J Mater Chem A* 2017, 5 (46), 24076-24082.
223. Yang, Q. Y.; Xu, Z.; Fang, B.; Huang, T. Q.; Cai, S. Y.; Chen, H.; Liu, Y. J.; Gopalsamy, K.; Gao, W. W.; Gao, C., MXene/graphene hybrid fibers for high performance flexible supercapacitors. *J Mater Chem A* 2017, 5 (42), 22113-22119.
224. Hu, M. M.; Li, Z. J.; Li, G. X.; Hu, T.; Zhang, C.; Wang, X. H., All-Solid-State Flexible Fiber-Based MXene Supercapacitors. *Adv Mater Technol-Us* 2017, 2 (10).
225. Zhang, S. W.; Yin, B. S.; Liu, C.; Wang, Z. B.; Gu, D. M., A low-cost wearable yarn

- supercapacitor constructed by a highly bended polyester fiber electrode and flexible film. *J Mater Chem A* 2017, 5 (29), 15144-15153.
226. Ai, Y. F.; Lou, Z.; Li, L.; Chen, S.; Park, H. S.; Wang, Z. M. M.; Shen, G. Z., Meters-Long Flexible CoNiO₂-Nanowires@Carbon-Fibers Based Wire-Supercapacitors for Wearable Electronics. *Adv Mater Technol-Us* 2016, 1 (8).
227. Ghidui, M.; Lukatskaya, M. R.; Zhao, M. Q.; Gogotsi, Y.; Barsoum, M. W., Conductive two-dimensional titanium carbide 'clay' with high volumetric capacitance. *Nature* 2014, 516 (7529), 78-U171.
228. Ren, C. E.; Hatzell, K. B.; Alhabeab, M.; Ling, Z.; Mahmoud, K. A.; Gogotsi, Y., Charge- and Size-Selective Ion Sieving Through Ti₃C₂T_x MXene Membranes. *The Journal of Physical Chemistry Letters* 2015, 6 (20), 4026-4031.
229. Androulidakis, C.; Zhang, K. H.; Robertson, M.; Tawfick, S., Tailoring the mechanical properties of 2D materials and heterostructures. *2d Mater* 2018, 5 (3).
230. Ahmadpoor, F.; Wang, P.; Huang, R.; Sharma, P., Thermal fluctuations and effective bending stiffness of elastic thin sheets and graphene: A nonlinear analysis. *Journal of the Mechanics and Physics of Solids* 2017, 107, 294-319.
231. Yan, J.; Ren, C. E.; Maleski, K.; Hatter, C. B.; Anasori, B.; Urbankowski, P.; Sarycheva, A.; Gogotsi, Y., Flexible MXene/Graphene Films for Ultrafast Supercapacitors with Outstanding Volumetric Capacitance. *Adv Funct Mater* 2017, 27 (30).
232. Kudin, K. N.; Ozbas, B.; Schniepp, H. C.; Prud'homme, R. K.; Aksay, I. A.; Car, R., Raman Spectra of Graphite Oxide and Functionalized Graphene Sheets. *Nano Letters* 2008, 8 (1), 36-41.
233. Zheng, X. M.; Chen, W.; Wang, G.; Yu, Y. Y.; Qin, S. Q.; Fang, J. Y.; Wang, F.; Zhang, X.

- A., The Raman redshift of graphene impacted by gold nanoparticles. *Aip Adv* 2015, 5 (5).
234. Pimenta, M. A.; Dresselhaus, G.; Dresselhaus, M. S.; Cancado, L. G.; Jorio, A.; Saito, R., Studying disorder in graphite-based systems by Raman spectroscopy. *Phys Chem Chem Phys* 2007, 9 (11), 1276-1291.
235. Couly, C.; Alhabeab, M.; Van Aken, K. L.; Kurra, N.; Gomes, L.; Navarro-Suarez, A. M.; Anasori, B.; Alshareef, H. N.; Gogotsi, Y., Asymmetric Flexible MXene-Reduced Graphene Oxide Micro-Supercapacitor. *Adv Electron Mater* 2018, 4 (1).
236. Dikin, D. A.; Stankovich, S.; Zimney, E. J.; Piner, R. D.; Dommett, G. H. B.; Evmnenko, G.; Nguyen, S. T.; Ruoff, R. S., Preparation and characterization of graphene oxide paper. *Nature* 2007, 448 (7152), 457-460.
237. Shen, X.; Lin, X. Y.; Yousefi, N.; Jia, J. J.; Kim, J. K., Wrinkling in graphene sheets and graphene oxide papers. *Carbon* 2014, 66, 84-92.
238. Qu, G. X.; Cheng, J. L.; Li, X. D.; Yuan, D. M.; Chen, P. N.; Chen, X. L.; Wang, B.; Peng, H. S., A Fiber Supercapacitor with High Energy Density Based on Hollow Graphene/Conducting Polymer Fiber Electrode. *Adv Mater* 2016, 28 (19), 3646-3652.
239. Jiang, D. G.; Zhang, J. Z.; Li, C. W.; Yang, W. R.; Liu, J. Q., A simple and large-scale method to prepare flexible hollow graphene fibers for a high-performance all-solid fiber supercapacitor. *New J Chem* 2017, 41 (20), 11792-11799.
240. Yang, X.; Cheng, C.; Wang, Y.; Qiu, L.; Li, D., Liquid-Mediated Dense Integration of Graphene Materials for Compact Capacitive Energy Storage. *Science* 2013, 341 (6145), 534-537.
241. Lin, Z. F.; Barbara, D.; Taberna, P. L.; Van Aken, K. L.; Anasori, B.; Gogotsi, Y.; Simon, P., Capacitance of Ti₃C₂T_x MXene in ionic liquid electrolyte. *J Power Sources* 2016, 326, 575-

- 579.
242. Chattopadhyay, R., 1 - Introduction: types of technical textile yarn. In *Technical Textile Yarns*, Alagirusamy, R.; Das, A., Eds. Woodhead Publishing: 2010, pp 3-55.
243. Riding, G., 10—THE EFFECT OF YARN TWIST ON FILAMENT PROPERTIES. *Journal of the Textile Institute Transactions* 1965, 56 (3), T109-T120.
244. Zhai, S. L.; Jiang, W. C.; Wei, L.; Karahan, H. E.; Yuan, Y.; Ng, A. K.; Chen, Y., All-carbon solid-state yarn supercapacitors from activated carbon and carbon fibers for smart textiles. *Materials Horizons* 2015, 2 (6), 598-605.
245. Kovacevic, S.; Hajdarovic, K.; Grancaric, A. M., Influence of warp loading on weaving machines upon yarn deformation. *Text Res J* 2000, 70 (7), 603-610.
246. Yoder, T.; Greene, B.; Porter, A., *Carbon Structure Hazard Control*. 2015.
247. Barella, A., The Fatigue Behavior of a Warp Yarn and its Influence on Weaving Performance. *Text Res J* 1973, 43 (7), 428-430.
248. Hu, H.; Zhu, M., A study of the degree of breakage of glass filament yarns during the weft knitting process. *Autex Research Journal* 2005, 5 (3), 41-148.
249. Wang, Z. Y.; Qin, S.; Seyedin, S.; Zhang, J. Z.; Wang, J. T.; Levitt, A.; Li, N.; Haines, C.; Ovalle-Robles, R.; Lei, W. W.; Gogotsi, Y.; Baughman, R. H.; Razal, J. M., High-Performance Biscrolled MXene/Carbon Nanotube Yarn Supercapacitors. *Small* 2018, 14 (37).
250. Huang, Y.; Hu, H.; Huang, Y.; Zhu, M. S.; Meng, W. J.; Liu, C.; Pei, Z. X.; Hao, C. L.; Wang, Z. K.; Zhi, C. Y., From Industrially Weavable and Knittable Highly Conductive Yarns to Large Wearable Energy Storage Textiles. *Acs Nano* 2015, 9 (5), 4766-4775.
251. Wei, H.; Hu, H.; Feng, J.; Zhang, M.; Hua, T., Yarn-form electrodes with high capacitance

- and cycling stability based on hierarchical nanostructured nickel-cobalt mixed oxides for weavable fiber-shaped supercapacitors. *J Power Sources* 2018, 400, 157-166.
252. Sun, J. F.; Huang, Y.; Fu, C. X.; Wang, Z. Y.; Huang, Y.; Zhu, M. S.; Zhi, C. Y.; Hu, H., High-performance stretchable yarn supercapacitor based on PPy@CNTs@urethane elastic fiber core spun yarn. *Nano Energy* 2016, 27, 230-237.
253. Zhang, J. Z.; Seyedin, S.; Gu, Z. J.; Yang, W. R.; Wang, X. G.; Razal, J. M., MXene: a potential candidate for yarn supercapacitors. *Nanoscale* 2017, 9 (47), 18604-18608.
254. Liu, Q. F.; Zang, L. M.; Yang, C.; Wei, C.; Qiu, J. H.; Liu, C. J.; Xu, X., A Flexible and Knittable Fiber Supercapacitor for Wearable Energy Storage with High Energy Density and Mechanical Robustness. *J Electrochem Soc* 2018, 165 (7), A1515-A1522.